A Study of Atmospheric Dynamics near the Mesopause Using Radio Meteor Echoes

by

Masaki Tsutsumi

January 1995

2)

A Study of Atmospheric Dynamics near the Mesopause Using Radio Meteor Echoes

by

Masaki Tsutsumi

January 1995

Acknowledgements

The author wishes to express his sincere appreciation to Professor Shoichiro Fukao for his guidance and stimulating supervision in the present work, and for the careful reading of the manuscript. The author also wishes to express his hearty gratitude to Emeritus Professor Susumu Kato for helpful comments and encouragement for the present work. The author deeply thanks Professor Iwane Kimura and Professor Hiroshi Matsumoto for their helpful advice and suggestions for the present work.

Special thanks are due to Dr. Toshitaka Tsuda for his kind guidance, continuous encouragements throughout the present work, and careful reading of the manuscript. The author also thanks Dr. Robert A. Vincent for the collaboration in the comparative study with Adelaide and Christmas Island MF radars, and constructive discussion and advice. The author thanks Professor Alan H. Manson and Dr. Chris E. Meek for the collaboration in the comparative study with Saskatoon MF radar, and helpful discussions and comments on the present work. The author is deeply indebted to Dr. Takuji Nakamura for his constructive advice, fruitful discussions, technical support, and also careful reading of the manuscript.

Thanks are also due to Dr. W. G. Elford and Dr. M. T. Elford for useful comments and discussions on mobility of ions in a meteor trail. The author appreciates Dr. S. P. Namboothiri for the collaboration in gravity wave study, helpful comments and careful reading of the manuscript. The author is also indebted to Dr. Chikao Nagasawa and Dr. Makoto Abo for the collaboration in the comparative study with the sodium Lidar.

A part of results in the present thesis is based on a collaborative study between Radio Atmospheric Science Center (RASC), Kyoto Univ., Agency for the Assessment and Application of Technology (BPPT), Indonesia and Indonesian National Institute of Aeronautics and Space (LAPAN). The author deeply appreciates the extensive collaboration of Ms. Sri Woro B. Harijono and Ms. Tien Sribimawati and all the staffs of BPPT. Thanks are also due to Professor Harsono Wiryosumarto, Mr. Pramono Mardio and Mr. Nurzaman Adikusumah.

The author thanks Drs. Takehiko Aso, Toru Sato, Manabu D. Yamanaka and Mamoru Yamamoto for a number of useful discussions, comments and suggestion.

The author is grateful to Drs. Takuya Sugiyama, Tomoyuki Takami and Yasuhiro Murayama, and Messrs. Tatsuhiro Adachi and Hiroyuki Hashiguchi for helpful discussions and technical support in computer software. The author thanks to Messrs. Naoto Fujioka and Yasunari Tanimura for helping with data analysis. The author is indebted to all staff of RASC, Kyoto University. Thanks are also due to operators from Mitsubishi Electric Corporation for the countless effort to maintain and operate the MU radar.

The MU radar belongs to, and is operated by the Radio Atmospheric Science Center, Kyoto University.

Abstract

The amount of industrial waste produced by human activity has been increasing since the Industrial Revolution in the 19 th century, and now has become significant enough to affect the natural balance of the earth's environment, causing various environmental problems. These various minor atmospheric constituents are transported to the whole earth's atmosphere by the general circulation in the height region of 10-100 km, called the 'middle atmosphere'. Thus, precise understanding of the behavior of the middle atmosphere is now a subject of great importance. The structure of the middle atmosphere is believed to be maintained by complicated dynamical processes governed by atmospheric waves and mean winds. In particular, the mesopause region (80-100 km) is known to be quite active in dynamics, however behavior of even fundamental physical quantities such as wind velocity and temperature have not been fully understood due to a lack of observations.

In this thesis we have developed new techniques to observe temperature fluctuations, simultaneously with wind velocity observations, utilizing radio meteor echo measurements with a meteor wind radar near Jakarta (6°S, 107°E), Indonesia and the MU radar in Shigaraki (35°N, 136°E), Japan. By means of these observations together with results obtained at other radar and lidar observatories we studied atmospheric dynamics around the mesopause.

We transported the meteor radar, originally constructed in 1977 at Shigaraki, to Jakarta for observations of the equatorial mesopause region after some system improvements, and have been conducting observations since November 1992. The MU radar was also applied to meteor echo observations, which is characterized by a high time-height resolution of 1 hr × 1 km realized by fully utilizing the functions of the MU radar. Both the radar techniques employed an antenna with a wide radiation pattern to effectively detect meteor echoes from wide spatial area and also a radio interferometer in reception to accurately determine echo arrival directions. Further we proposed an improved meteor echo observation system with the MU radar, which can collect meteor echoes during routine observations of the radar.

Distributions of meteor echoes were described as a function of zenith angle, horizontal distance, height and local time.

From ionic diffusion theory, the ambipolar diffusion coefficient, D, which is inferred from the decay time constant of meteor echo intensity, is related to atmospheric temperature, T, and density, ρ, as $D \propto T/\rho$. The observed mean height profile of D showed an exponential increase with a scale height fairly consistent with that of atmospheric density. Further, using the Boussinesq approximation, we found that the normalized D fluctuations, D'/D_0, can be related to those of temperature, T'/T_0, as $D'/D_0 \sim 2 \cdot T'/T_0$, where the suffix 0 denotes the time mean

values. The observed T'/T_0 oscillated with various periods. Diurnal variations of T'/T_0 at Shigaraki were characterized by constant phase with height in morning hours in summer, implying a relationship with evanescent diurnal tides or in-situ heating by solar radiation. The T'/T_0 fluctuations at Shigaraki during winter months often showed a downward phase progression, which seemed to be related to vertical propagating diurnal tides. The results in Jakarta also generally showed downward phase progression.

Other temperature fluctuations with periods shorter than 1 day were investigated as well. The observed downward phase progression of T'/T_0 indicated that these fluctuations were caused by gravity waves. Fluctuations of T'/T_0 and the horizontal wind velocity showed phase and amplitude relationships consistent with linear gravity wave theory. Based on these results, the horizontal propagation directions of dominant gravity waves were studied. They showed a seasonal variation with prefered directions toward east and west in summer and winter, respectively, which was interpreted to be related to directional filtering by prevailing zonal winds below the meteor region. We also conducted comparison observations of dominant gravity waves with the MU radar and a sodium lidar in Hachioji (35.6°N, 139.4°E) which are separated by a horizontal distance of 310 km. Density perturbations obtained from both sets of observations showed good agreement, indicating that the radar and lidar observed the same gravity wave.

Planetary scale wind motions were investigated by means of cooperative radar observations. We studied the behavior of planetary waves in middle latitudes using the meteor radar at Shigaraki and MF radars at Adelaide (35°S, 138°E) and Saskatoon (52°N, 107°W). Simultaneous wave activities were found at Shigaraki and Adelaide and also at Shigaraki and Saskatoon with periods of 1 10 days.

Long-period waves in the equatorial mesopause region were analyzed using the Jakarta meteor radar and a MF radar on Christmas Island (2°N, 158°W). The prevailing winds were dominated by semiannual oscillations with westward maxima in the equinoxes for the zonal component and an annual oscillation flowing from summer to winter hemispheres for the meridional component. Significant year to year variations were also found. Waves with periods of 3-4 days and 6-7 days revealed marked enhancements for the zonal components, whose phase differences between the stations implied the possibility that these were equatorial Kelvin waves.

Further, conspicuous two-day oscillations were observed simultaneously at Shigaraki and Jakarta in both T'/T_0 and wind fields. Phase relationships between the stations and between T'/T_0 and the wind components strongly suggested that these waves were identical to theoretically predicted (3, 0) mode Rossby-gravity waves.

Contents

List of Figures

List of Tables

Chapter 1

General Introduction

1.1 Dynamics of Earth's Atmosphere

Studies of the global changes of earth's environment have keenly become important in order to protect not only human activities, such as agriculture and various industry, but also even human bodies and animals. Industrial exhausts, whose amount has been rapidly increasing in the last decades, now act to modify the earth's environment, represented by the greenhouse effect and ozone depletion. These materials, however, do not affect the whole earth's atmosphere if they stay still at the place where they are produced. Recent atmospheric studies have revealed, however, that these materials are brought up to the middle atmosphere at 10–100 km altitudes, due to vertical wind motions in tropics, then they are spread globally by general circulation.

The earth's atmosphere is commonly separated into four layers according to its vertical temperature structure, i.e., troposphere, stratosphere, mesosphere and thermosphere. The troposphere is the lowest part from the ground up to about 15 km, where the main heat source is the solar radiation absorbed by the ground, resulting in temperature decrease with height. Thus, the atmosphere becomes unstable, and convection is generated. Most of meteorological phenomena occur in the troposphere. The region above the troposphere is called the stratosphere, where the temperature increases with height up to the stratopause around 50 km. The high temperature around the stratopause is caused by the absorption of solar ultraviolet radiation by the ozone layer. Above the stratopause, the temperature again decreases with height, which is called the mesosphere, and it reaches a minimum at the mesopause around 90 km. The region above the mesopause is called the thermosphere, where the temperature rapidly and monotonously increases with height because of the absorption of strong solar extreme ultraviolet radiation and X-rays.

The general circulation is basically generated by seasonal and latitudinal variations of net radiative heating, that is, the sum of solar heating and infrared cooling. Figure 1.1 (a) shows latitude-height section of zonal mean temperature in January from CIRA (COSPAR International Reference Atmosphere) 1986. In the lower atmosphere equatorial region is receiving a major part of the solar energy, producing a temperature distribution with a maximum over the equator and minima near the poles. While, from 20 to 70 km temperature shows antisymmetric distribution about the equator with a maximum and minimum at summer and winter poles, respectively, due to the greater absorption of solar radiation by the ozone layer in the summer hemisphere. Temperature distribution above 70 km is separately discussed below.

Figure 1.1 (b) shows zonal mean zonal wind in January from CIRA 1986. In the troposphere eastward jets are recognized with maxima at about 10 km in middle latitudes. On the other hand, above 20 km up to 80 km westward and eastward winds are dominated in summer and winter hemisphere, respectively. The relation between these temperature and zonal wind distributions are reasonably explained by the thermal wind relation [e.g., *Andrews et al.*, 1987].

The general circulation is generated to complement latitudinal difference of solar radiation and the infrared emission. From this point of view meridional circulation is essentially important, in transporting heat energy and minor constituents. Figure 1.2 shows the mean meridional mass stream function theoretically predicted by *Garcia and Solomon* [1983] in the case of northern-hemisphere winter solstice conditions. The figure indicates that tropospheric air is brought up to middle atmosphere through equatorial tropopause by active cumulus convection there.

In equatorial lower atmosphere perturbations of the atmosphere are the largest in three regions where ocean and continent interface; Africa, South America and Indonesia. In particular, Indonesia is characterized by the complicated land-sea distribution, moreover, amount of precipitable water, carrying latent heat, is the largest over Western Pacific around Indonesia. Tall cumulus clouds exclusively generated near Indonesia sometimes penetrate deep into the stratosphere, which transport the tropospheric air above the tropopause. Now the equatorial Indonesia has been known as a fountain region of minor constituents [*Newell and Gould-Stewart*, 1981].

Minor constituents such as chlorine compound, nitrogen oxide and water vapor carried up to the middle atmosphere are then transported to middle to high latitude, and a part of those pass through winter polar region.

Although the general circulation is basically driven by the solar heating, obser-

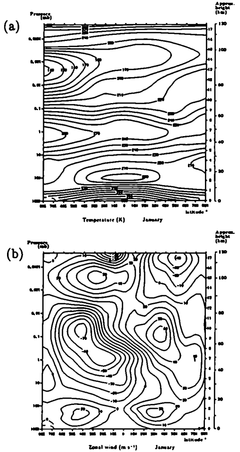

Figure 1.1: Monthly zonal mean latitude vs. pressure scale height cross sections for (a) temperature and (b) zonal wind in January [CIRA 1986]. The left ordinate is pressure (mb); the first right ordinate (0–17) is pressure scale height; the second right ordinate is approximate geometric height.

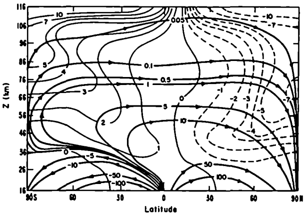

Figure 1.2: Mass stream function for the residual meridional circulation (kg $m^{-1}s^{-1}$) shown in heavy solid lines and the diabatic heating distribution (light solid and dashed lines; K day^{-1}) for northern-hemisphere solstice conditions as computed in a two-dimensional model [After *Garcia and Solomon* [1983]].

vational studies found a reversal of meridional temperature and prevailing zonal wind near the mesopause which was unable to explain by radiative balance of the atmosphere. That is, temperature distribution above 70 km shows a maximum and minimum at winter and summer poles, respectively, as seen in Figure 1.1 (a). Zonal wind becomes very weak at 80–90 km, and its direction changes above that level. Subsequent theoretical and observational studies have pointed out that dynamical processes, especially gravity waves propagating from lower altitudes, play an important role to reverse the general circulation [e.g, *Lindzen*, 1981; *Matsuno*, 1982; *Vincent and Reid*, 1983; *Tsuda et al.*, 1990]. While, as for the mass transport in the meridional plane, atmospheric waves are again thought to play an important role. That is, in addition to mean meridional flow, eddy motions produced by dynamical and chemical processes due to atmospheric waves [*Andrews et al.*, 1987] are thought to significantly contribute to the mass transport, which are taken into account for the calculation shown in Figure 1.2.

It is also notable that the mesopause region is a transition layer for many atmospheric parameters such as diffusion, composition and ionization rate [*Tohmatsu*, 1990]. Below and above a boundary called turbopause at about 100 km, turbulent and molecular diffusion processes are dominant, respectively. According to this diffusion process composition of the atmosphere is almost uniform below the turbopause, while separation due to gravity becomes effective above that. Moreover, absorption of extreme ultraviolet and X-ray causes a transition from neutral atmosphere to ionized atmosphere around the mesopause. Depending on ionization rate definitions are made for ionospheric layers of D, E and F, with approximate corresponding height ranges of 70-80 km, 80–160 km and 160-500 km, respectively. Thus, the mesopause region is a very interesting object of observations.

There are a number of techniques to observe the middle atmosphere. In-situ measurements such as rocket and radiosonde observations have been operated for long time, in which compact measuring instrument is carried by a rocket or balloon. These measurements are characterized by their good height resolution. However, these observations give only one vertical profile by a single launch.

On the other hand, remote sensing measurements using radio wave and optical rays provide more successive data in time and height. The remote sensing measurements are classified into two types; i.e., satellite and ground based techniques. The satellite observation has now become one of the most powerful methods, which is suitable for studying global scale waves. However, its height resolution is about 2-8 km [*Rodgers*, 1984], and time resolution is not very good for a polar orbit satellite, thus it is not good at studying atmospheric waves with small vertical and time scale. While, the ground based remote sensing systems, such as radars and lidars are characterized by high time and height resolution of about 1-10min and 100m-5km, although horizontal coverage of each system is fairly limited. Various radar measurements of the middle atmosphere have revealed characteristics of the atmospheric waves, such as planetary waves, atmospheric tides and gravity waves. The lidar is an observation method developed more recently. The Rayleigh lidar can observe the atmospheric density and temperature at the altitude of 30-80km, which covers the blind height of radar observation (30-60km). Sodium lidar can also observe density and temperature at the altitude of 80-105km.

Among these radar and lidar techniques which can observe the atmosphere from the mesosphere to lower thermosphere, MST (Mesosphere, Stratosphere and Troposphere) radar observations are the most excellent in time and height resolutions as schematically illustrated in Figure 1.3. However, MST radar observations with turbulence echoes in the mesosphere are limited to daylight hours due to low electron density at night (Figure 1.4). Lidar observations are difficult to conduct in daylight hours. While, MF (Medium Frequency, partial reflection) radar and meteor radar can continuously monitor wind fields although they are not so good as MST radar in time and height resolution. Furthermore, observations using meteors can be conducted with an MST radar, and even in parallel with normal MST radar observations by attaching a fairly compact economical processing system [e.g., *Avery et al.*, 1983; *Wang et al.*, 1988]. In addition, they have a potential to be used for study of atmospheric temperature and density as well [e.g., *Greenhow and Hall*, 1960].

1.2 Atmospheric Waves

In the middle atmosphere atmospheric waves with various periods exist superposed by mean winds, such as gravity waves (5 min-21 hr at 35° latitude), atmospheric tides (24 hr, 12 hr, 8 hr,..) and planetary waves (1 day ~).

Assuming adiabatic inviscid process and small scale motions, these atmospheric waves were theoretically investigated by using the perturbation equations of atmospheric motions derived from the fundamental equations of the atmospheric dynamics such as the equation of motion, first law of thermodynamics, continuity equation and equation of state for an ideal gas. The restoring forces for these waves are provided by the stable density stratification of the atmosphere, namely, the buoyancy, and by the rotation of the earth, as represented by Coriolis force.

Gravity waves, which are types of waves with relatively small horizontal scale owe their existence mainly to the buoyancy. They are mainly exited in the lower

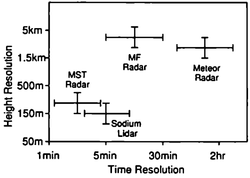

Figure 1.3: Time-height resolutions of principle observation techniques near the mesopause.

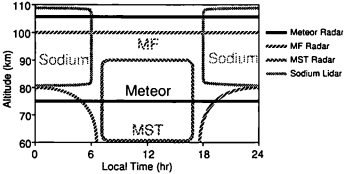

Figure 1.4: Time-height coverage of observation techniques near the mesopause.

atmosphere through geostrophic adjustments, shear instability of jet stream, interaction of topography with a jet stream and various meteorological disturbances such as fronts and cumulonimbus convections [e.g., *Murayama et al*, 1994; *Tsuda et al.*, 1994].

While, atmospheric tides and planetary waves have larger horizontal structure. Atmospheric tides are daily oscillations, which are primarily forced by diurnal variations of the heating due to absorption of solar ultraviolet radiation by atmospheric water vapor and ozone. On the contrary planetary waves have no such specific periodic sources. Restoring force of these global-scale waves is latitudinal difference of Coriolis force. The buoyancy is also important for vertically propagating atmospheric tides.

In the followings we briefly review characteristics of each wave.

Atmospheric Tides

In considering atmospheric waves with a large horizontal extent, such as atmospheric tides and planetary waves, we have to employ a set of perturbation equations described on spherical coordinate [e.g., *Kato*, 1980]. By using a separation constant, called 'equivalent depth', obtained differential equation can be separated into two equations which determine vertical and horizontal structure of waves, called vertical and horizontal structure equations, respectively. The horizontal structure equation is known as Laplace's tidal equation. For forced waves like atmospheric tides their frequency and longitudinal wave number can be specified, thus by substituting these parameters into the Laplace's tidal equation we can obtain equivalent depth as eigen-value and corresponding eigen-function called 'Hough function', which determine latitudinal variations of amplitudes of vertical displacement of air parcel, thus, temperature fluctuations. Further, the equivalent depth is substituted into the vertical structure equation, then corresponding vertical structure is calculated.

Application of a classical tidal theory to atmospheric tides was established mainly by *Kato* [1966] and *Lindzen* [1967]. It is shown that the equivalent depth of diurnal tides can take negative values as well as positive values [*Kato*, 1966]. While, the Hough function was solved by *Longuet-Higgins* [1968]. Figure 1.5 shows Hough functions for some principal modes of diurnal tides together with corresponding latitudinal variations of eastward and northward wind velocity components. The modes with positive and negative equivalent depths are called positive modes and negative modes, respectively. A positive mode of diurnal tides can propagate vertically, while a negative mode is an external wave with a standing phase structure along height. The positive modes of diurnal tides have the major part of their energy in the low latitude region, while the negative modes show large amplitudes in the high latitude as seen in Figure 1.5. This is shown

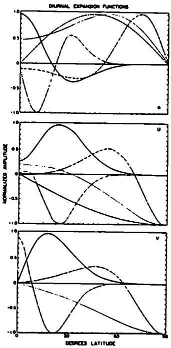

Figure 1.5: TOP: Hough functions for the solar diurnal tidal modes normalized to a maximum value of unity. Keys and normalization factors for each Hough mode are as follows; (1, 1), solid line, 0.606; (1, -1), broken line, 1.034; (1, -2), dotted line, 1.054; (1, -4), dashed-dot line, 0.513; (1, 2), dashed-double-dot line, 0.641. BOTTOM: northerly (southward) velocity expansion functions normalized to a maximum value of unity. Normalization factors are 0.026., 0.126, 0.100, 0.024, 0.015, respectively. CENTER: westerly (eastward) velocity expansion functions normalized to a maximum value of unity. Normalized factors are 0.038, 0.130, 0.100, 0.024, 0.018, respectively, [after *Forbes* [1982]]. (1, 1), (1, -1), (1, -2), (1, -4) and (1, 2) are the first symmetric positive, first antisymmetric negative, first symmetric negative, second symmetric negative and first antisymmetric positive modes, respectively.

by the fact that since the Coriolis frequency becomes equal to the frequency of the diurnal tide at 30° latitude. Thus, at lower latitudes diurnal tides can propagate as a gravity wave, while at higher latitudes they cannot propagate vertically, resulting in the dominance of a negative mode. On the contrary, since the frequency of a semidiurnal tide is always larger than the Coriolis frequency, it only takes positive equivalent depth, i.e., all the semidiurnal tides can propagate vertically.

During the Middle Atmosphere Program (MAP) in 1982–1985, many observations on atmospheric tides were carried out. The new CIRA model (CIRA, 1986) of the atmospheric temperature and zonal mean wind was also provided, utilizing various observations carried out during MAP. Theoretical models of atmospheric tides utilizing these updated model atmosphere and improved information on the dissipating process due to the eddy diffusion were recently proposed [*Vial*, 1986; *Forbes and Hagan*, 1988; *Forbes and Vial*, 1989], and discrepancy with the observations becomes smaller. Now the monthly mean climatology comparatively agrees better between the models and observations for semidiurnal tides [*Forbes and Vial*, 1989], however, diurnal tides are not yet well described by the models.

Gravity Waves

Assuming that a gravity wave is a plane wave, we can derive the dispersion relation of gravity wave from perturbation equations when $f^2 < \omega^2 < N^2$ as follows

$$m^2 \simeq \frac{N^2 - \omega^2}{\omega^2 - f^2} k^2 \tag{1.1}$$

where ω is the intrinsic frequency of the wave (frequency observed in the frame moving with the background flow) which can be written as $\omega = k(c - \bar{u})$, where c and $\bar{u}$ are the horizontal phase velocity of the gravity wave and horizontal mean wind speed in the direction of wave propagation, respectively [e.g., *Gossard and Hooke*, 1975; *Andrews et al.*, 1987].

The polarization relations between the variables of gravity waves can be derived from the basic equations as

$$v' = -i\frac{f}{\omega}u' \tag{1.2}$$

$$w' = -\frac{k}{m}u' \tag{1.3}$$

where u' and v' are the parallel and perpendicular components of wave induced horizontal wind fluctuations relative to the wave propagation directions, w' is the wave-induced vertical wind. Note that the prime, ′, denotes perturbation quantities. Equation 1.2 indicates that phase difference between u' and v' are 90°

and the ratio of amplitudes is proportional to f/ω, thus, a tip of the horizontal wind vector draws an elliptical locus, which shows a clockwise rotation with increasing height in the case of the northern hemisphere.

Further, we introduce temperature fluctuation, T', accompanied by vertical motion of air parcel in an adiabatic condition. Since relative temperature perturbations are shown to be equal to those of potential temperature under the Boussinesq approximation [e.g., *Stull*, 1988], T' can be related to the vertical wind velocity perturbation, w', assuming the preservation of potential temperature, θ, as follows:

$$\frac{T'}{T_0} \simeq \frac{\theta'}{\theta_0} = -i\frac{N}{g}\frac{N}{\omega}w' \tag{1.4}$$

where g is gravitational acceleration, and suffix 0 denotes time mean values. Using Equations 1.1 and 1.3, T'/T_0 can be related to u' as follows:

$$\frac{T'}{T_0} = -i\frac{N}{g}u' \tag{1.5}$$

where we assume $f^2 << \omega^2 << N^2$. This equation indicates that T' becomes maximum earlier than u' by a quarter of the wave period.

In equatorial region there is a type of wave with planetary scale called equatorial Kelvin wave, which satisfies the dispersion relation identical to that of two-dimensional gravity wave [*Andrews et al.*, 1987]. The equatorial Kelvin wave is trapped only in a narrow latitude region around the equator, propagating eastward. Figure 1.6 shows the wind perturbation and geopotential structure for the Kelvin wave, indicating that its horizontal wind perturbation appears only in zonal direction.

Planetary Waves

Planetary waves, or Rossby waves, can be classified into two types; forced planetary waves and free traveling planetary waves. In the followings we limit our interest to the traveling planetary waves.

Analogous to atmospheric tides a set of equation on spherical coordinate is employed to investigate planetary waves. However, the traveling planetary wave has no specific periodic forcing unlike atmospheric tides. Thus, firstly, the equivalent depth is calculated as an eigen value of the vertical structure equation, then corresponding wave frequency and latitudinal structure, namely, Hough function, are determined from the Laplace's tidal equation [e.g., *Salby*, 1981a].

A lot of efforts have been devoted to observations of planetary waves and identify their global structure since 1950's [e.g., *Madden and Julian*, 1972, 1973]. In the stratosphere satellite observations greatly contributed to the study of planetary waves, such as 5, 10, 4 and 16 day waves, which were shown to correspond

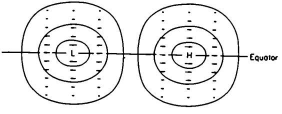

Figure 1.6: Plan view of horizontal velocity and height perturbations associated with an equatorial Kelvin wave [*Matsuno*, 1966]

to symmetric (1, 1) mode, anti-symmetric (2, 1) mode, symmetric (1, 2) mode and symmetric (1, 3) mode, respectively, when the equivalent depth is taken to be about 10 km [e.g., *Hirota and Hirooka*, 1984; *Hirooka and Hirota*, 1985], where notation is made as $(s,\ n-s)$ for waves with a zonal wavenumber of s and a meridional index of n.

In the mesosphere and lower thermosphere, large scale motions with various periods have been also reported [e.g., *Salby and Roper*, 1980; *Ito et al.*, 1984]. Among them the most conspicuously observed wave is a quasi-two-day wave (hereafter, the two-day wave), which reveals large amplitude in low to high latitudes in summer hemisphere. From satellite and cooperative radar observations [e.g., *Mullar and Nelson*, 1978; *Rodgers and Prata*, 1981], the two-day wave was interpreted as a manifestation of one of Rossby waves, called a Rossby-gravity wave, with a zonal wavenumber of three, that is, antisymmetric (3, 0) mode obtained from a numerical calculation [*Salby*, 1981a].

However, except for the two-day wave global structure of most of planetary waves in the mesopause region has not been identified yet. In addition, although simultaneous observations of wind and temperature fluctuations are necessary to fully understand the behavior of planetary waves, such observations have not been conducted due to a lack of such observation techniques.

We now study a relation between wind and temperature fields associated with a Rossby-gravity wave using an equatorial β plane approximation [*Holton*, 1992]. When we assume a zonally propagating wave the meridional structure of the

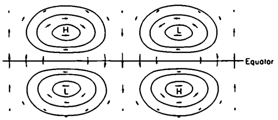

Figure 1.7: Plan view of horizontal velocity and height perturbations associated with an equatorial Rossby-gravity wave [*Matsuno*, 1966].

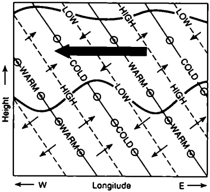

Figure 1.8: Longitude-height section along a latitude circle north of the equator showing pressure, temperature, and wind perturbations for a thermally damped Rossby-gravity wave. Areas of high pressure are shaded. Small arrows indicate zonal and vertical wind perturbations with length proportional to the wave amplitude. Meridional wind perturbations are shown by arrows pointed into the page (northward) and out of the page (southward).

horizontal velocity and geopotential perturbations can be expressed as

$$\begin{pmatrix} u \\ v \\ \phi \end{pmatrix} = v \begin{pmatrix} i|m|\omega N^{-1}y \\ 1 \\ i\omega y \end{pmatrix} \exp\left(\frac{\beta|m|y^2}{2N}\right) \tag{1.6}$$

where u, v and ϕ are eastward and northward wind velocity and geopotential perturbations, respectively, ω and N are wave frequency and Brunt-Väisälä frequency, respectively, m is vertical wavenumber, y is distance from the equator. β is defined as $2\Omega/a$, where Ω and a are the angular velocity and the radius of the earth, respectively. The resulting horizontal wave structure is plotted in Figure 1.7, which shows an antisymmetric structure about the equator. The wave structure in the longitude-height section at a latitude north of the equator is shown in Figure 1.8, indicating phase relation between v' and temperature fluctuation is expected to be in phase, while, in the southern hemisphere it is expected to be anti-phase.

1.3 Fundamental Characteristics of Meteors

This section is devoted to a brief description of the characteristics of meteors and their impacts on the earth's atmosphere.

A meteor is a streak of light or "shooting star" that is seen in the night sky when a small object, known as a meteoroid, enters the earth's atmosphere at a high speed and dissipates its energy and substance in a brief blaze. Very rarely, a residual fragment of a large meteoroid may survive the fiery plunge and drop to the ground as a meteorite [*McKinley*, 1961]. The velocities of meteors approaching the earth are in the range of 11.3 to 72 km/s. The lower limit is set by the velocity of a particle escaping the earth's gravitational field and is therefore the minimum velocity that a particle falling toward the earth can have. The upper limit of 72 km/s is the sum of the velocity of the earth orbiting the sun, 29.8 km/s, and the escaping velocity for a particle leaving the solar system, i.e., 42 km/s. The fact that observed meteor velocities hardly exceed the upper boundary is proof that most, if not all, meteors are members of the solar system [*Sugar*, 1964].

Meteors are classified into sporadic and shower meteors. Shower meteors are thought to be mainly originated from small particles ejected from comets orbiting the sun. On each perihelion passage a comet loses a large number of particles, which gradually spread along the cometary orbit and fill a tube of space, called a meteor stream. If the cometary orbit intersects the earth's orbit, the earth will pass the intersection on the same date every sidereal year, and if the intersection falls in the meteor stream region, a meteor shower will result. In the case of an old comet the meteor stream may finally close all around the orbit, so that a meteor shower will result on every earth crossing. Thus, shower meteors have been investigated to study the history of meteor streams and ages of their mother comets [e.g., *Watanabe et al.*, 1992].

A sporadic meteor or non shower meteor is not a member of a recognized shower. Over a period of a year it is found that the number of sporadic meteors greatly surpasses the total number of meteors belonging to the well-known showers, particularly if the counts are extended to the very faint meteors [*McKinley*, 1961].

Due to meteoric ablation a large flux of metallic vapor is continuously entering the Earth's atmosphere, whose amount was estimated to be as large as 44,000 kg/day by *Hughes* [1978] using satellite, radio and visual observation data in particle mass range larger than 10^{-13} g. The major metallic constituents of meteorites are by weight Na 0.6 %, Ca 1.0 %, Ni 1.5 %, Al 1.7 %, Fe 11.5 % and Mg 12.5 % [*Mason*, 1971]. The existence of these abundant metallic ions activates the behavior of the atmosphere in various aspects as follows.

The meteoric atoms are believed to be the source of ions in sporadic E layers, occurring occasionally in the ionosphere at altitudes between 90 and 140 km with a typical thickness of 1-3 km [*Huuskonen et al.*, 1988]. For the formation of sporadic E layers dynamical processes, such as vertical shear of neutral wind and electro-dynamical forces associated with aurora, are also thought to play important roles to concentrate these ions into the thin layers [e.g., *Whitehead*, 1970; *Kirkwood and von Zahn*, 1991].

Furthermore, these meteoric metals are of chemically importance for number of reasons [*Plane*, 1991]. Firstly, meteoric metals have very unusual atmospheric chemistries. Atmospheric temperature near the mesopause is known to show large seasonal variation, especially in high latitudes, causing important seasonal changes in the chemistry. The solar insolation penetrating through the mesosphere is only attenuated at wavelengths less than 190 nm [*Shimazaki*, 1985], meaning that photochemistry requiring high photon energies occurs in this region, producing ions and neutral species that are often in highly excited electron and vibratinal states.

It is also speculated that these meteoric metals, X, descending from the mesosphere react with the atmosphere to form XCl. Since these processes continue in the absence of sunlight, chlorine may accumulate during polar winter. The sudden release of this chlorine from photodissociation of these salts during spring could give rise to the loss of ozone in the upper polar stratosphere [*Aikin and McPeters*, 1986].

The free metal atoms and ions, which are relatively easy to view with ground-based instruments such as a meteor radar and various optical instruments like a sodium lidar, appear to be excellent tracers of the dynamical processes [e.g., *Plane*, 1991].

1.4 Outline of the Thesis

As described in previous sections meteor echo observation is one of crucial observation techniques to study atmospheric dynamics near mesopause region. In this thesis we developed meteor echo observation techniques using two radars of Radio Atmospheric Science Center (RASC), Kyoto Univ., then studied waves with various period.

In Chapter 2 we describe developments of meteor echo measurement techniques using a meteor radar and the MU radar for observations of wind velocity and ambipolar diffusion coefficient. Further, we propose an improved meteor observation system with the MU radar, which can collect meteor echoes in parallel with normal MU radar observations. Then, we discuss time-height distribution of meteor echoes for each radar observation.

In Chapter 3 we study relation between ambipolar diffusion coefficient and atmospheric temperature and density, then apply the relation to observations of density scale height and temperature fluctuations caused by wave activity. Among observed fluctuations with various periods we examine diurnal component in this chapter.

Chapter 4 is devoted to studying behavior of gravity waves using simultaneous wind and temperature fluctuation observations with the MU radar with resolutions of 1 hr × 1 km. First, we examine phase and amplitude relations between observed wind and temperature fluctuations in comparison with a prediction from a linear theory of gravity waves. Then, we investigate seasonal variations of propagation directions of dominant gravity waves. Finally, we present a comparison observation of gravity waves with the MU radar and a sodium lidar.

We study planetary scale wind motion in Chapter 5 using data from several radar observatories which are widely spaced in longitude and latitude. First, planetary waves in middle latitudes are investigated. Then, we describe the behavior of mean winds and planetary waves in equatorial mesopause region. Finally, by means of simultaneous observations of wind and temperature fluctuations using meteor echoes we study global structure and seasonal behavior of two day wave.

In Chapter 6 we present summary and conclusions of this thesis.

Chapter 2

Radar Observations of Meteor Echoes

In this thesis we study atmosphere dynamics near the mesopause utilizing radio echoes scattered from an ionized meteor trail. We first review the characteristics of radio scattering by a meteor trail, then present development of observation techniques for both wind velocity and ambipolar diffusion coefficient, and finally discuss time-height distributions of meteor echoes together with performance of obtained data. Observations were carried out with the MU (Middle and Upper atmosphere) radar and a meteor radar in Shigaraki (35°N, 136°E). While, we transported the meteor radar from Japan to Jakarta (6°S, 107°,E), Indonesia.

2.1 Radio Scattering by Meteor Trails

When a meteoroid impinges the earth's atmosphere, it interacts with neutral atmosphere and ablates meteor atoms, which have an initial velocity comparable to that of the meteoroid (about 11–73 km/s). Collisions between the ablated ions and atmosphere molecules are frequently repeated to slow the ions down to the thermal velocities of the environment neutral atmosphere within less than a millisecond [*McKinley*, 1961]. Then, an ionized meteor trail is left along a pass of the meteoroid. The trail has an initial radius, r_0, approximated by

$$\log_{10} r_0 = 0.019h - 1.92 + \log_{10}(V/40) \tag{2.1}$$

where r_0 is in meter, and h and V are altitude in km and impinging velocity in km/s, respectively [*Baggaley*, 1980; 1981; *Thomas et al.*, 1988]. When V is 40 km/s, r_0 at 90 km altitude is 0.62 m. The meteor trail is further moved by wind motion of ambient neutral atmosphere.

We receive a backscattered radar echo from the meteor trail using HF and VHF radio waves. Meteor echoes can be classified into two types, i.e., underdense and overdense types, according to the line electron density. A boundary line electron density of the two types is given by

$$\pi^3 \frac{r_0{}^2}{\lambda} \cdot 2.4 \cdot 10^{14} \tag{2.2}$$

where λ is a radar wavelength [*McKinley*, 1961]. When a line electron density is less than this value, all the received echoes become underdense types.

For the overdense trail, transmitted radio waves can not penetrate into the meteor trail, but is totally reflected, because its frequency is lower than the critical frequency of the plasma corresponding to the electron density of the trail. While, in the case of an underdense echo, electron density is so low that the radio wave penetrates into the trail, and it is partially reflected by each electron independently, with the scattering cross section of

$$\sigma_e = \frac{\mu_0^2 e^4}{16\pi^2 m^2} \tag{2.3}$$

where μ_0, m and e are magnetic permeability of air, electron mass and electron charge, respectively. By using a conventional radar equation, the received power from each electron scattering, ΔP_r, is represented by a formula

$$\Delta P_r = \frac{P_t G_t G_r \lambda^2 \sigma_e}{64\pi^3 R^4} \tag{2.4}$$

where P_t, G_t, G_r and R are transmitted power, transmitting antenna gain, receiving antenna gain and range, respectively. By integrating Equation 2.4 for all electrons in the trail, we can obtain echo power. When we assume an instantaneously formed infinitely long cylindrical trail, the total received echo power at $t = 0$, P_r, is obtained as

$$P_r = \frac{P_t G_t G_r \lambda^3 \sigma_e}{128\pi^3 R^3} q_e^2 \frac{c^2 + s^2}{2} \tag{2.5}$$

where q_e is a line density of electrons, and c and s are Fresnel integrals. If the trail is a straight column without distortions, we can regard the scattering of radio wave as a Fresnel reflection. The value $(c^2 + s^2)/2$ becomes almost 1 by integrating Equation 2.4 for a few Fresnel zones [*McKinley*, 1961].

Figure 2.1 shows a numerical model of an instantaneous meteor echo power and phase during the formation of the meteor trail with solid lines in the absence of diffusion process and wind motions of ambient neutral atmosphere. We assumed that meteor trail is an infinitely long straight column and uniformly ionized along the trail. We also neglect deceleration of impinging velocity of the meteoroid in the atmosphere. The abscissa is distance along the trail measured from the minimum range point between the trail and the radar. In Figure 2.1 (a) the echo power increases gradually during the early stage of trail formation, and quickly reaches maximum value when the meteor body passes through the minimum range point. After that the echo power becomes fairly constant. The main reflection occurs on a region called the first Fresnel zone. The extent of the first Fresnel zone is given as $\sqrt{2\lambda R_0}$ centered at the minimum range point, where R_0 is the minimum range between the radar and the trail. The first Fresnel zone, for example, is 1.1 km when λ and R are 6 m (50 MHz) and 100 km, respectively.

We neglected the effects of diffusion processes on a meteor trail so far. However, the actual meteor trail suffers various diffusion processes such as ambipolar diffusion, eddy diffusion, recombination, chemical reaction and also distortion by wind motions. Among them ambipolar diffusion is found to play play a dominant role of trail diffusion [e.g., *Jones*, 1975]. The radius of a meteor trail, r, is given by

$$r^2 = 4Dt + {r_0}^2 \tag{2.6}$$

where D is ambipolar diffusion coefficient, t and r_0 are time and an initial radius after the meteor trail reaches thermal equilibrium, respectively [*McKinley*, 1961]. A meteor trail considering ambipolar diffusion is schematically illustrated in Figure 2.2. The echo intensity is reduced by the radial diffusion of the trail in the case of the underdense echo [*Herlofson*, 1948], thus echo power at t, $P_r(t)$, decays exponentially as

$$P_r(t) = P_r(0)\exp(-\frac{32\pi^2 Dt}{\lambda^2}) \tag{2.7}$$

and a decay time constant, τ, is defined as

$$\tau = \frac{\lambda^2}{32\pi^2 D} \tag{2.8}$$

The echo power in the existence of ambipolar diffusion is shown in Figure 2.1 (a) with a solid line. Further, the ambipolar diffusion coefficient, D, is known to depend on atmospheric temperature, T, and density, ρ [e.g., *Kaiser*, 1953, *Greenhow and Neufeld*, 1955, *Weiss*, 1955] as

$$D \propto \frac{T^C}{\rho} \tag{2.9}$$

where C is a constant. Since temperature is fairly constant around the mesopause, D is expected to increase exponentially with height, which is used to observe

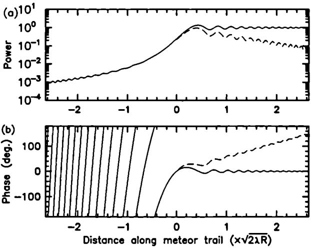

Figure 2.1: A numerical calculation of (a) an instantaneous meteor echo power and (b) phase. The abscissa is a distance along the meteor trail measured from the minimum range point between the trail and the radar, expressed in terms of the length of the first Fresnel zone. The solid lines indicate values in the absence of ambipolar diffusion and wind motions, while the dashed lines in the existence of these effects. Amplitude and phase values after formation of the infinitely long trail, in the case of no ambipolar diffusion and wind motions, are set to be unity and 0, respectively.

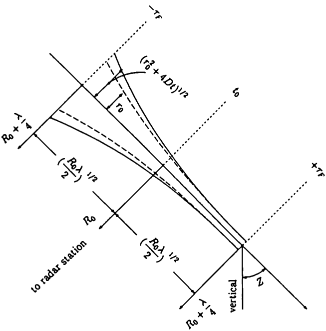

Figure 2.2: A model of a meteor trail at time τ_F after the time when the meteoroid with impinging velocity V passes the minimum range point, where $\pm\tau_F = (\lambda R/2)^{1/2}/V$ is defined as one-half of the first Fresnel zone of the trail. The initial radius is shown as the dashed line, while the effective radius due to diffusion is indicated by the solid-line envelope [*McKinley*, 1961].

density scale height. This relation is also utilized to estimate echo reflection height (decay height method) for radar systems which do not directly measure the reflection height. Further, it is possible to delineate information of temperature and density fluctuations from temporal variations of D, which will be precisely discussed in subsequent chapters.

On the other hand, phase of meteor echo shown in Figure 2.1 (b) exhibits rapid increase during the beginning stage of the trail formation, which is caused by the approaching meteor body. The phase variation with time gives us the values of impinging velocities of meteorites, which is an important parameter to know its orbit in the interplanetary space. The phase becomes almost constant after the first Fresnel zone is formed in the case of motionless atmosphere as shown with the solid line. However, the ionized particles in a meteor trail are moved with wind motion of the ambient neutral atmosphere [*Manning et al.*, 1950], causing the Doppler frequency shift Δf in the received echo. A general idea for an approaching meteor trail toward the radar site is shown with a dashed line in Figure 2.1 (b). The radial wind v_r is inferred from Δf as

$$v_r = \frac{\lambda}{2}\Delta f \tag{2.10}$$

So far we assumed that the initial radius of meteor trail is negligibly small compared with the radar wavelength. However, if the initial trail width is of the order of the radio wavelength then the radiation backscattered from electrons in the trail may not be in phase, and the echo power can be severely attenuated [e.g., *Olsson-Steel and Elford*, 1987]. Further, since a meteor takes a finite time to cross the first Fresnel zone, it is possible that the trail has diffused to reach a width comparable to the radar wavelength by the time the meteor has reached the end of the zone. These effects destructively reduce the echo amplitude at higher altitude and set an upper limitation for observations, called 'echo ceiling', which is approximately 100–110 km for conventional meteor radars operated at some tens of MHz [*McKinley*, 1961].

2.2 Development of Observational Techniques

In this section we describe observation techniques of atmospheric parameters using meteor echoes. We employed two radar systems in this study; a meteor wind radar and the MU radar. Before describing each radar technique we discuss system requirements to realize the meteor observations.

1. Meteor appears randomly in a large spatial area. Fortunately, we do not need transmitting and receiving antennas with a large gain because we can

expect a fairly strong echo from the trail due to the specular reflection, whose intensity ranges over 80 dB [*e.g.*, *McKinley*, 1961]. Therefore, antennas with wide radiation patterns have advantages in collecting plenty of meteor echoes from wide azimuth and zenith angles.

2. It is essentially important to measure arrival direction and reflection height of each meteor echo accurately in order to recompose wind velocity vector from observed radial wind velocities. Therefore, it is required to employ a radio interferometer technique, with which we can determine the arrival directions by measuring phase differences of the received echoes between more than three antennas. The echo reflection height is further calculated from the direction and the range between the radar and the meteor trail.

3. The length of the first Fresnel zone is an order of 1 km as described in the previous section, indicating that minimum scale of observable atmospheric phenomena is also around this length. Therefore, necessary and sufficient range resolution is about 1 km.

4. Meteor echoes occupy quite a small part of received signal records, because meteor trails are fairly small targets and normally disappear within one second due to diffusion, suggesting that most of the received signal is useless. Therefore, it is required to record only a part of signal at a range where the echo appears for a certain duration time in order to reduce total amount of stored data by using a sophisticated realtime processing software or hardware.

In the following three subsections, we discuss how we realized these system requirements. We first describe a meteor wind radar system, then an application of the MU radar to meteor echo observations and lastly a proposal for an improvement for the meteor observation system with the MU radar, which can collect meteor echoes in parallel with the routine observations of the MU radar.

2.2.1 Meteor Wind Radar System

A meteor radar was constructed at Shigaraki (35°N,136°E) in 1977. It is a compact economical radar system, which is equipped with fundamental functions to realize the necessary conditions discussed above. Five-element Yagi antennas with the half power beam width of as wide as 60° in one way pattern were used for both transmission and reception in order to detect echoes from a large spatial area. Single Yagi antenna was used for transmitting radio waves. While, three Yagi's composed an interferometer, providing signal to the phase sequenced interferometer (PSI) [Rudman et al., 1970] equipped for accurate measurements of arrival angles of a meteor trail. A computer system was employed for radar control and real time data processing. The radar was operated under two modes; 'watch mode' and 'measure mode'. During the watch mode the radar searched a meteor echo whose intensity exceeded a threshold value, without recording received signal. When the received signal is recognized to be a meteor echo, the operation mode is changed to the measure mode, where the computer fixes the sample range and records the signal for 200 transmitting pulses (about 1 sec.) [*Aso et al.*, 1979; *Tsuda et al.*, 1982].

In 1983–1986 continuous observations were carried out by the automatic observing system for 24 hours and a large observational data base for the meteor height of 80–110 km were stored.

In 1992 we transported the meteor wind radar to Indonesia to investigate equatorial atmosphere dynamics after some improvements of the system [*Fujioka*, 1993]. In order to start observations in the equatorial Indonesia, it is necessary to consider the operation conditions there. Since scientists who designed this system cannot stay at the observatory for all the observation period, the system should be operated under a control of a computer, except for the least maintenance by the operator, visiting the observatory occasionally. Even if there is a severe damage on the hardware, small MTTR (mean time to recover) is demanded in order to reduce the gap of continuous observation to as short as possible. Considering these requirements, we have improved the meteor radar, especially the transmitter and computer. We also have replaced the transmitting and receiving antennas with newly designed ones [*Tsuda et al.*, 1995].

Figure 2.3 shows the block diagram of the new meteor radar. The transmitter, antennas and the computer subsystems are encircled by dotted line in Figure 2.3. Basic parameters of Jakarta meteor wind radar are summarized in Table 2.1. In the followings we describe the improvement of transmitter, antennas, and the computer system.

Transmitter and Antenna

A transmitter used in the meteor radar is required to produce a pulse, with a width of about 300μsec, at the central frequency of 31.57 MHz, where the peak and average output power should be 10 kW and 0.5–1 kW, respectively. In the original system we used a transmitter with a tube as the final linear amplifier. The tube must be replaced every about 1,000 hours (about one month) in order to keep the nominal output power. Such a maintenance was not ideal from a point of cost.

Therefore, we decided to employ a new transmitter originally designed for a magnetic resonance imaging system, which utilized solid-state circuit for all the

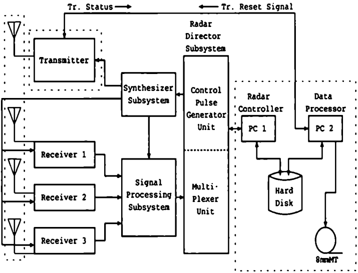

Figure 2.3: Blockdiagram of the Jakarta meteor wind radar. The areas encircled by dotted lines are parts newly designed for the continuous observations in Jakarta, Indonesia [*Fujioka*, 1993].

Parameter	Value
Operating frequency	31.57 MHz (VHF band)
Antenna	TX: 5-elements Yagi
	RX: three 5-elements Yagi's (interferometer)
beam directions	45° off the zenith
Transmitter	dual solid state amplifier
peak power	$\sim$ 10 kW (maximum)
average power	$\sim$ 0.5 kW (duty ratio 5% (maximum)
bandwidth	$\sim$ 400 kHz (maximum) (pulse width: 10 μs)

Table 2.1: Basic parameters of Jakarta meteor wind radar [*Tsuda et al.*, 1994].

amplifiers (model MRI-10000, ENI. Inc.). This transmitter consists of a final amplifier, a system combiner and a signal splitter. The final amplifier of MRI-10000 is composed of two sets of amplifiers, each of which produces any RF pulse with the peak power of 5 kW.

Since the two amplifiers are connected in parallel by the system combiner and the signal splitter, we can also operate the transmitter by using a single final amplifier with the half power, even when the other amplifier does not work due to system damage or malfunction. The new transmitter is equipped with a serial communication channel (RS-232C) to provide the current status of the system operation and to accept system-control from outside, which further enables us an automatic operation supervised by a computer. For instance, when the transmitter stopped observation due to power failure or other reasons, the computer checks the status of the transmitter and restarts it through communication.

The antenna employed for the meteor wind radar is a five element Yagi type with the half power width of 60°. Single antenna is used for transmission, while three sets are used for reception to compose an interferometer. Configuration of the antennas for the interferometer, especially the spacing of antennas, should be carefully designed. It is normally true that a longer baseline gives better accuracy, which, however, might give more than two solutions of arrival angles. By taking the antenna beam width and the range of ambiguity in arrival angle determinations into consideration, we chose the antenna arrangement in Indonesia as shown in Figure 2.4, which is rather decided not to produce unambiguous solutions for a single echo by compromising their accuracy.

Computer System

Since the computer system, originally installed in the meteor radar, is quite

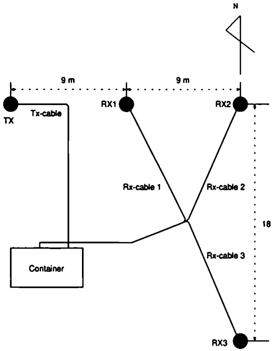

Figure 2.4: Configuration of transmitting (TX) and receiving (RX) antennas for the Jakarta meteor wind radar. Two antenna beam directions were used, which were 45° off the zenith toward south on November 2, 1992–March 10, 1993 and March 18–June 8, 1993 and toward north on March, 11–17, 1993 and from June 9, 1993 [*Fujioka*, 1993].

old, we replaced it with two sets of personal computers whose instruction speed is 3–5 times as fast as the old one. However, basic functions of the computer in the radar are the same, which cover 1) radar control, 2) data-acquisition, 3) data storage, 4) radar status check and 5) data processing. Tasks of these functions are summarized briefly in the followings.

1.) radar control: to control operation of the radar hardware; pulse scheme for transmission and reception.

2.) data-acquisition and transfer: to transfer output of A/D converters of signal detector and phase detector and also other digital signals from the signal processing subsystem to the memory of PC for a certain duration (about 1 sec.), then to transfer the data to the hard disk.

3.) data storage: to store the data collected on the hard disk to an 8 mm MT (EXABYTE) at 0:00 once a day.

4.) status-check: to record the status of the radar operation every hour, such as the condition of the transmitter, local time of the first and last echoes in the last one hour, the hourly mean radial wind velocity and the noise level, and to restart the transmitter if it stops due to some error.

5.) data processing: to illustrate raw data for each meteor echo, such as range, echo intensity, Doppler signal and phase detector output, and to additionally plot time variation of meteor echo rate and the hourly-mean radial wind velocity.

Since the items 1) and 2) largely concern the operation of the radar hardware and data-transfer, we should design a real time software. While, the items 3), 4) and 5) do not necessarily correlate with, for instance, the pulse scheme of the radar operation. We installed two sets of small personal computers (NEC (Nippon Electric Company) , PC9801DX/U2), with a 16-bit CPU (Intel 80286, 12 MHz), which is characterized by high reliability and good cost-performance, where one of them manages items 1) and 2), while the other 3), 4) and 5).

Operation in Indonesia

In October 1992 we transported the radar system to an observatory, located in PUSPIPTEK (Indonesia National Center for Research, Science and Technology), Serpong (6.4°S, 106.7°E), located about 27 km south-west of Jakarta (Figure 2.5). So far, we have exchanged the antenna illuminating area several times between southward and northward directions. The reason and the effective center of observation area is precisely discussed in Section 2.3. Figure 2.6 shows the outlook

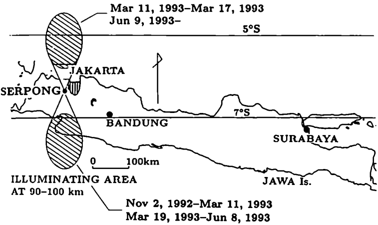

Figure 2.5: Location of the radar observatory. Shaded areas show radar approximate illuminating area. The illuminating area was toward south during November 2, 1991 to March 11, 1993 and March 19, 1993 to June 8, 1993 and toward north during March 11-17, 1993 and after June 9, 1993.

of the radar site, where all the equipment other than antennas is installed in a container in the left side. A boundary layer radar was also installed in the same area, as shown in the right side of the figure. The radar site occupies a square area of 40 m × 40 m, surrounded by a safety fence with a height of about 2 m.

Radar status is checked once a day by a watcher in PUSPIPTEK. Operators from BPPT (Agency for the Assessment and Application of Technology), Indonesia visit the radar site once or twice in a week to change the 8mm MT and maintain the radar system. Further, they analyze the data and send quick-look output to RASC.

2.2.2 Application of the MU Radar to Meteor Echo Observations

The MU (middle and upper) radar is a monostatic pulse Doppler radar at 46.5 MHz, constructed at Shigaraki, Shiga, Japan (34.85°N, 136.10°E) in 1984. The MU radar is characterized by an active phased array system with 475 Yagi antennas [*Fukao et al.*, 1985a, b]. The whole antenna of the MU radar consists of 19 hexagonal subarrays (shown separated by thin solid lines in Figure 2.7), and six deformed areas at the edge of the circular antenna. The subarrays, each of which contains 19 three-element crossed Yagi's, are units for the control of transmission and reception. There are four independent receiver channels in the MU radar. Observation parameters of the MU radar can be flexibly changed by softwares, which enables us to operate the radar as various kinds of radar systems such as an MST (mesosphere, stratosphere and troposphere) radar and also an IS (incoherent scatter) radar. The basic parameter of the MU radar is shown in Table 2.2.

For a normal MST radar observation by the DBS (Doppler beam swinging) technique the whole antenna is used to obtain a pencil-like main lobe with a narrow beam width, which is alternately connected to a transmitter and a receiver. However, this set up is not necessarily suitable for meteor echo observations. Therefore, we used special combinations of the subarrays for both transmission and reception in this study. In the following, we first discuss the beam patterns of the transmitting antenna, and then describe the interferometer system and data taking procedure.

Transmitting Antenna

A pencil-like antenna beam used for normal DBS techniques with the MU radar has a half power beam width of 3.7°, which is schematically illustrated in Figure 2.8. In the present study, we designed a doughnut-like radiation pattern, also shown in Figure 2.8, by controlling the phase of the radio waves transmitted

Figure 2.6: A view of the Jakarta meteor wind radar observation site [*Tsuda et al.*, 1995].

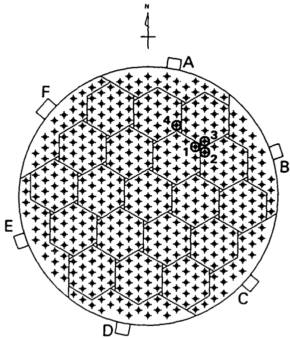

Figure 2.7: A plane view of the antenna array of the MU radar. The open circles with numerals, 1 to 4, indicate the single crossed Yagi's used to construct an interferometer (modified from [*Nakamura et al.*, 1991]).

Parameter	Value
Location	Shigaraki, Shiga, Japan (34°51′N, 136°06′E)
Radar system	monostatic pulse radar; active phased array system
Operational frequency	46.5 MHz
Antenna	circular array of 475 crossed yagis
apperture	8330 m^2 (103 m in diameter)
beam width	3.6° (one way; half power full-width)
steerability	steering is completed in each IPP
beam directions	1657; 0°–30° off zenith angle
polarizations	linear and circular
Transmitter	475 solid state amplifiers (TR modules; each with output power of 2.4 kW peak and 120 W average)
peak power	1 MW (maximum)
average power	50 kW (maximum duty ratio is 5 %)
bandwidth	1.65 MHz (maximum)
IPP	400 μs to 65 ms (variable)
Receiver	
bandwidth	1.65 MHz (maximum)
dynamic range	70 dB
IF	5 MHz
A/D converter	12 bits × 8 channels
Pulse compression	binary phase coding up to 32 elements; Barker and complementary codes

Table 2.2: Basic parameters of the MU radar [*Fukao et al.*, 1985a].

from each Yagi antenna [*Nakamura et al.*, 1991]. As we will show in Section 2.3, a large number of meteor echoes are detected at zenith angles of 20° – 45°, so that the doughnut-like beam is found to be effective for detecting many meteor echoes.

We introduce a coordinate system, (x, y, z), where x, y and z correspond to eastward, northward and vertical axes, respectively. For a pencil-like beam with the narrowest main lobe width and maximum bore-sight gain, the phase of the transmitted radio waves for each antenna, Φ_i, is generally given as

$$\begin{aligned} \Phi_i &= \frac{2\pi}{\lambda}(\mathbf{l} \cdot \mathbf{x_i}) \qquad (2.11) \\ &= \frac{2\pi}{\lambda}(x_i \sin\theta \sin\phi + y_i \sin\theta \cos\phi) \end{aligned}$$

where $\mathbf{l} = (\sin\theta\cos\phi, \sin\theta\sin\phi, \cos\theta)$ is the direction cosine of the bore sight pointing to the azimuth angle, ϕ, and zenith angle, θ, and $\mathbf{x_i} = (x_i, y_i, 0)$ is the coordinate of the i-th antenna measured from the center of the whole array.

In order to obtain the doughnut-like radiation pattern, we need to replace Φ_i with Φ'_i by adding a phase shift, φ_i,

$$\begin{aligned} \Phi'_i &= \Phi_i + \varphi_i \qquad (2.12) \\ \varphi_i &= \frac{2\pi}{\lambda}(|\mathbf{x_i}| \cdot \sin\theta_B) \qquad (2.13) \\ &= \frac{2\pi}{\lambda}(\sqrt{x_i^2 + y_i^2} \cdot \sin\theta_B) \end{aligned}$$

where θ_B is the zenith angle of the direction of the maximum gain. Figure 2.9 shows numerical computation of the doughnut-like radiation pattern in comparison with in the case of the pencil-like beam. The antenna gain at $\theta = 0°$ for the doughnut-like pattern is suppressed by about 20 dB relative to the pencil-like beam, while the sidelobes between 23° and 40° are considerably enhanced, by 6 to 16 dB. As a result, a doughnut-like main lobe appears centered at 30°, which radiates radio waves more effectively in oblique directions.

Interferometer and Data-taking Procedure

The interferometer can be constructed by connecting three receiver channels to individual single Yagi's located at the points of an equilateral triangle with a length of 0.697 λ, as indicated in Figure 2.7. Since even the shortest base line ($0.697\ \lambda \times \cos 30°$) of the interferometer is longer than 0.5 λ, the arrival angle of each echo can not be uniquely determined. That is, an echo at a zenith angle of larger than 56.5° contaminates the first lobe of the interferometer pattern. This ambiguity, however, can be removed by using the fact that almost all underdense

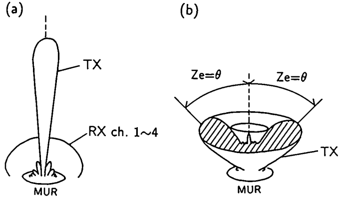

Figure 2.8: Schematic diagrams of the antenna patterns used in this study: (a) vertically pointed pencil-like beam and (b) doughnut-like beam [*Nakamura et al.*, 1991].

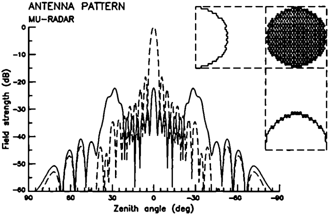

Figure 2.9: Numerical models of the radiation patterns for a pencil-like beam (dashed line) and a doughnut-like beam (solid line). The plotted patterns are cross sections of the 0 ° - 180 ° plane with the azimuth angle measured from the north. The upper-right panel shows a plane view of subarrays and cross sections of weighting functions of the radiation intensity.

meteor trails appear at altitudes higher than 70 km [e.g., McKinley, 1961; Aso et al., 1980]. The largest zenith angle is realized when a meteor trail at 70 km is detected in the largest range gate. Therefore, if sample range is less than 70 km/cos 56.5° =127 km, all the meteor echoes should be received by the first lobe of the interferometer. Even if echoes are detected at ranges longer than 127 km, some part of their arriving directions can be determined without ambiguities when only one of the possible reflection heights exceeded 70 km. Further, since meteor echoes are seldom detected above 110 km with the MU radar as seen in Section 2.3, large part of arriving directions of the residual meteor echoes can be uniquely determined by assuming the reflection heights are between 70-110 km.

Here, we briefly describe other observation parameters, the data-taking procedure and the history of their developments. A transmitted pulse is phase modulated by a 13 bit Barker code or a 16 bit complementary code with a 6 μs or 8 μs subpulse width, the inter-pulse period (IPP) being 1.6 - 2.56 ms. Note that when the 13 bit Barker code is employed strong meteor echoes sometimes produce more than 12 images of the true echo at every two adjacent range gates because suppression of the range side lobe of the 13 bit Barker code is only -22dB. In this study, we removed these spurious echoes by selecting the echo with the largest intensity in a single record. To minimize this problem a 16-bit complementary code has been adopted since August 1991.

The received signal is sampled every 0.9 and 1.2 km for the subpulse widths 6μ s and 8 μ s in range, respectively, coherently integrated for 4-8 pulses and once stored on memory of the computer as complex time series of 3-5 sec. When the echo intensity exceeds a threshold for six successive data points of 80-100 msec in a time series, the received signal is recognized as a meteor echo and recorded to a magnetic tape. Otherwise, the received signal is discarded.

Up to December 1989 we recorded all the time series of the received signals on a magnetic tape, regardless of the detection of meteor echoes, since the real-time data-taking software was not installed. Frequent accesses to the magnetic tape increased the blanking time of the measurements, so the effective observation period was only 35% of the total observation period, that is, 21 min/hour. As a compromise, we superposed data for 4 times to make the data compact, which, however, reduced the signal-to-noise ratio (SNR) by 6 dB, and therefore, it was difficult to detect weak meteor echoes. After an update of the data taking software in 1990, the effective observation time was increased to nearly 60% without the superposition. Further, according to the upgrade of the MU radar system in 1994, the continuous observations without loss time has been realized.

Decay rate of meteor echo power is calculated on offline by fitting a line to time variations of logarithm of echo power. Since the fitting was sometimes difficult for echoes of which intensities were not large enough, we conducted fitting to time variations obtained by coherently superimposing those for the receiver channels after subtracting phase difference between the channels, which raised SNR by 6 dB when number of receiver channels was four. Note that a meteor echo at high altitude, showing rapid decay, often may not be detected unless it has a large enough signal-to-noise ratio (SNR), which limits the maximum D value. For instance, the maximum D value becomes about 8 $\mathrm{m^2/s}$ and 12 $\mathrm{m^2/s}$ for meteor echoes with peak SNR of 20 dB and 30 dB, respectively.

Figure 2.10 shows an example of the time variations in the amplitude and the phase of an underdense meteor echo received at 17:51 LT on 10 December, 1989, where the phase difference between channels 1 and 2 is also plotted. The meteor echo had a peak intensity of 29 dB above the noise level and showed an exponential decay with a time constant of about 41 msec, from which the ambipolar diffusion constant was inferred to be 3.2 $\mathrm{m^2/s}$ from Equation 2.8. Smooth phase progression is caused by a Doppler frequency shift corresponding to an approaching radial wind velocity of 12.5 m/s toward the radar site. The phase difference between the two channels is fairly constant during the time when the echo intensity is sufficiently large.

Accuracy of the Interferometry System

In studying minute height structure of atmospheric parameters accuracy of meteor echo arrival angle and reflection height measurements is of great concern, especially for the observations of ambipolar diffusion coefficient which is very sensitive to height. Therefore, we discuss the accuracy using an interferometer here.

First we describe a set of equations to calculate the echo arrival directions from phase differences between three receiving antennas. We define position and phase of i th antenna as $\boldsymbol{x}_i(\lambda)$ and $\Phi_i(rad.)$. $\boldsymbol{x}_i$ is expressed by the coordinate system as

$$\begin{aligned} \boldsymbol{x}_i &= (x_i, y_i, 0) \\ (i &= 1 \sim 3) \end{aligned} \tag{2.14}$$

where we assume an interferometer on a horizontal plane. Direction cosine of the meteor arrival direction, $\boldsymbol{k}$ is expressed as

$$\boldsymbol{k} = (l, m, n) \tag{2.15}$$

Phase difference between i th and j th antennas are given by

$$\frac{\Phi_i - \Phi_j}{2\pi} = (\boldsymbol{x}_i - \boldsymbol{x}_j) \cdot \boldsymbol{k} \tag{2.16}$$

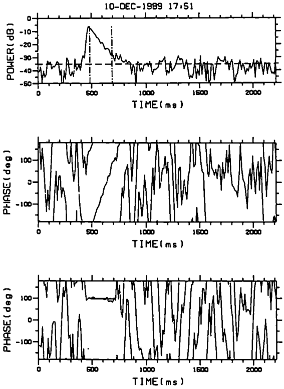

Figure 2.10: An example of the time variation in the amplitude (top) and the phase (center), and phase difference between the two receivers (bottom) for a meteor echo received at 17:51 LT on 10 December, 1989. The dashed line in the top panel indicates the estimated noise level, while the vertical chained lines indicate the period used for determining the phase difference [*Nakamura et al.*, 1991].

This is further expressed with the coordinate system as

$$\begin{aligned} l(x_1 - x_2) + m(y_1 - y_2) &= (\Phi_1 - \Phi_2)/(2\pi) && (2.17) \\ l(x_2 - x_3) + m(y_2 - y_3) &= (\Phi_2 - \Phi_3)/(2\pi) && (2.18) \end{aligned}$$

Finally, the echo arriving direction is found as

$$\begin{aligned} l &= \frac{1}{2\pi} \frac{\Phi_1 y_2 + \Phi_2 y_3 + \Phi_3 y_1 - (\Phi_1 y_3 + \Phi_3 y_2 + \Phi_2 y_1)}{A} && (2.19) \\ m &= \frac{1}{2\pi} \frac{\Phi_1 x_3 + \Phi_2 x_1 + \Phi_3 x_2 - (\Phi_1 x_2 + \Phi_2 x_3 + \Phi_3 x_1)}{A} && (2.20) \\ n &= \sqrt{1 - l^2 - m^2} && (2.21) \\ A &= x_1 y_2 + x_2 y_3 + x_3 y_1 - (x_1 y_3 + x_3 y_2 + x_2 y_1) && (2.22) \end{aligned}$$

Echo reflection height is further determined from this arrival direction and range between the radar and the meteor trail.

Now we consider an error of determination of the echo arrival direction due to a deviation involved in the measurements of the receiving antenna phase, $\Delta\Phi_i (i = 1 \sim 3)$. Apparent echo arrival direction (l_i, m_i, n_i) in the existence of $\Delta\Phi_i$ is approximated by

$$(l_i, m_i, n_i) = (l + \frac{\partial l}{\partial \Phi_i}\Delta\Phi_i, m + \frac{\partial m}{\partial \Phi_i}\Delta\Phi_i, n + \frac{\partial n}{\partial \Phi_i}\Delta\Phi_i) \qquad (2.23)$$

Errors in arrival zenith and azimuth angles, σ_{ze_i} and σ_{az_i}, are estimated from (l, m, n) and (l_i, m_i, n_i) as

$$\begin{aligned} \sigma_{ze_i} &= \arccos(n) - \arccos(n_i) && (2.24) \\ \sigma_{az_i} &= \arctan(l/m) - \arctan(l_i/m_i) && (2.25) \end{aligned}$$

The values of $\Delta\Phi_i$ can be thought to follow Gaussian distribution and be independent between the antennas. Therefore, total error in the arriving direction estimation is given by

$$\begin{aligned} \sigma_{ze} &= \sqrt{\sum_{i=1}^{3} (\sigma_{ze_i})^2} && (2.26) \\ \sigma_{az} &= \sqrt{\sum_{i=1}^{3} (\sigma_{az_i})^2} && (2.27) \end{aligned}$$

Using these equations we estimate the accuracy of our interferometry system. We first need to know the magnitude of the deviation involved in the measurements of

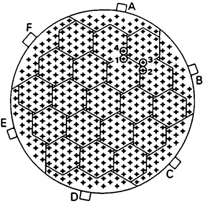

Figure 2.11: The special receiving antenna configuration for the experiment on December 10, 1991.

the phase difference received by a pair of Yagi antennas, which is probably caused by a random noise. For that purpose, we chose a special antenna combination shown in Figure 2.11, where the configurations of two antenna pairs, 1–4 and 2–3 (hereafter referred to as A14 and A23, respectively) were set to be the same, being aligned into north-south direction. Therefore, when a single meteor echo was detected, two sets of phase differences, which were ideally the same in the absence of noise, were independently obtained.

Figure 2.12 shows a scatter diagram, where $x-$ and $y-$ axes correspond to the phase differences detected with A14 and A23, respectively. The values should be distributed on the line, $y = x$, if there is no error due to the noise. Note, however, that the least squares fits showed the off-set as $y = x - 4.99°$, because the bias of the phase delays for A14 and A23 were not completely adjusted during the experiment. The offset can be removed for present meteor observations according to the improvement of phase adjustment method. The standard deviation from the fitted line in Figure 2.12 was estimated as 8.33°, from which the standard deviation of the phase determination error for each receiver channel (hereafter referred to as σ_e) can be inferred as $8.33°/\sqrt{4} = 4.17°$, by assuming that the noise distribution is Gaussian and uncorrelated between the channels.

Figure 2.13 shows the distribution of σ_{ze} and σ_{ae} for an interferometer with an equilateral triangle shaped configuration, where the baseline length is 0.698λ.

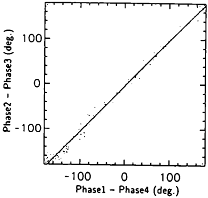

Figure 2.12: Comparison of the phase difference between the antenna pair 1-4 and 2-3 shown in Figure 2.11.

At the zenith angle of 30°, where large number of meteor echoes are normally detected as discussed in Section 2.3, σ_{ze} is about 1.5°, which corresponds to the standard deviation of the height determination of about 1.3km at the range of 100 km. Since the first Fresnel zone of a meteor trail is about 1.1 km at the range of 100km and the atmospheric phenomena whose scales are less than the Fresnel zone are difficult to be detected, the standard deviation of 1.3km is appropriate for meteor wind observations. However, it is not necessarily good for the observation of diffusion coefficient, because diffusion coefficient largely varies with height as precisely discussed in Chapter 3.

So far, we considered the interferometer constructed using three receiving antennas. However, we can additionally use the fourth antenna by utilizing the full capability of the MU radar system in order to construct an interferometer with a longer baseline, which gives a better resolution in determining arrival angles of meteor echoes. Figure 2.14 shows an example of the interferometer using four antennas with much longer baselines than the former equilateral triangle configuration. In order to exhibit the advantage of this arrangement, we present σ_{ze} and σ_{az} for the combination of the three antennas, 1, 3 and 4 in Figure 2.15. The values of σ_{ze} are about 0.4° – 0.8° at $\theta = 30°$, which corresponds to the standard deviation (or the error) in height as 0.3-0.6 km for a meteor echo at the range of 100 km. Because the scale height of diffusion coefficient is about

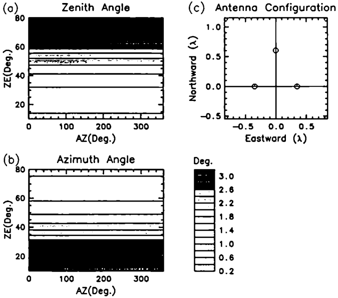

Figure 2.13: The accuracy of the interferometer using three antennas in the MU radar with the equilateral triangle shaped configuration shown in (c). (a) and (b) show the accuracy for zenith and azimuth angles, respectively.

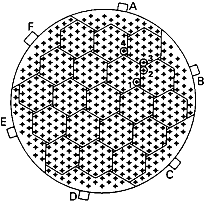

Figure 2.14: Configuration of the interferometer adopted since the observations on August 1991

6 km as discussed in Chapter 3 the standard deviation of 0.3-0.6 km is good enough for the observations of diffusion coefficient as well as wind velocity. The interferometer shown in Figure 2.14 has been used for the meteor observations since August 1991.

2.2.3 A Proposal for an Improved Meteor Observation System: MU/Meteor Monitor

In the last several decades meteor echo observations have revealed various scales of atmospheric motions such as mean wind, planetary waves, atmospheric tides and gravity waves [e.g., *Tsuda et al.*, 1987, *Ito et al.*, 1984, *Tsuda et al.*, 1988a; b, *Vincent et al.*, 1988, *Vincent et al.*, 1989, *Yamamoto et al.*, 1986]. Further, the meteor observation is useful for observing wider time and height ranges of atmospheric phenomena if it is simultaneously conducted with the turbulence echo observation in the mesosphere (60-90 km altitude, limited to daylight hours) and incoherent scatter observations (above 100 km). At present, however, the meteor observations with the MU radar has been conducted only on a campaign basis and also not carried out with other MU radar observations at the same time due to the system limitation.

Since we do not need the whole antenna array for receiving meteor echoes

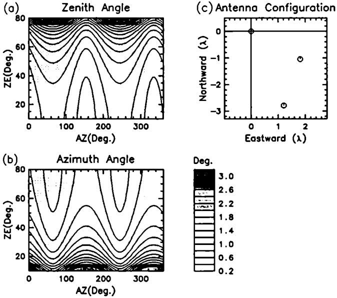

Figure 2.15: Same as Figure 2.13 except for the antenna configuration shown in (c)

but only three or four antennas, we can receive meteor echoes during other observations with the MU radar if we provide a data acquisition system with extra antennas. In order to decode pulse-modulated signals in reception, we can utilize three out of four receiving channels of the MU radar during the routine observations, which use only one receiver channel. But, it is not possible to conduct meteor observations with such observations that use multiple receiver channels as the spaced antenna drift (SAD) observations.

Figure 2.16 shows the schematic diagram of the meteor echo receiving system (hereafter referred to as the MU/Meteor Monitor), which consists of an interferometer with three extra antennas located near the array antenna of the MU radar and the data processing unit of meteor echoes, which can be operated simultaneously with the routine observations of the MU radar. We will utilize three of 475 transmitter-receiver (TR) modules for the improved system, which can reduce the expense for the development. Received signal with the extra antennas are down-converted to IF signal of 5 MHz in the TR module by mixing with local signal of 41.5 MHz and sent to the control building. The IF signal is split and separately mixed with two phase-quadrature reference signal of 5 MHz, analog-to-digital converted and decoded for pulse compression. The decoded signal is available for general purposes from the monitor output of the realtime data processing system of the MU radar newly developed in 1994. The signal is connected to the meteor detection hardware.

In the following we first describe the external receiving antennas suitable for meteor echo observations, and then show a design of the meteor echo detection hardware and realtime data processing software.

Receiving Antenna Design

For meteors at a range longer than 127 km their arrival directions are difficult to be decided without ambiguities by using antennas of the MU radar as discussed in Section 2.2.2. Therefore, we constructed an interferometer with an antenna spacing shorter than the MU radar array (0.698λ), so as to uniquely determine the arrival angles of all the echoes, although the accuracy in determining the arrival angles becomes worse as described in Section 2.2.2. Furthermore, majority of meteor echoes are detected at zenith angles larger than 30° even if the most of the transmitting radio power is concentrated in a pencil beam pointing to the zenith as discussed in Section 2.3. The three-element crossed Yagi antenna used in the MU radar has the radiation pattern with its maximum gain at $\theta = 0$. Therefore, it is recommended that the receiving antenna has larger gain at larger zenith angles for meteor observations.

Since the radiation pattern of a dipole antenna significantly varies with the antenna height from the ground, we can design a preferable antenna pattern for

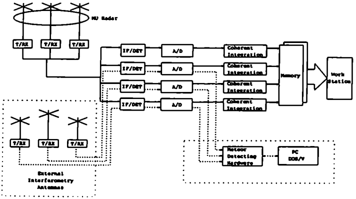

Figure 2.16: The schematic diagram of the MU/Meteor Monitor. Newly designed parts for meteor observations are encircled with dashed lines.

meteor observations. We decided to located the dipole antenna at the height of $\frac{3}{8}\lambda$ which has the maximum gain at the zenith angle of around 45°. We conducted comparative experiments using the antennas in the MU radar and the external dipole antennas, and found that the dipole antenna is advantageous to that of the Yagi antenna in receiving larger number of echoes from larger zenith angles. Computed radiation patterns of the receiving antenna and exact number and distribution of meteor echoes obtained from the experiments are described in Appendix B in more detail. Larger number of echoes realizes observations with higher time-height resolution. In addition, collection of echoes from wider zenith angles enables us to investigate horizontal propagation directions of waves by analyzing the cross-correlation between wind velocities obtained from different sub spatial areas [*Yamamoto*, 1986].

Meteor Detection Hardware and Realtime Processing Software

When we use the MU radar exclusively for meteor observations, we once record all the received signal into a memory for a duration of about 3 sec, then search meteor echoes. It is realized by employing quite a high speed realtime data processing system. This method has an advantage that we can detect more than one echo which appear at different ranges at the same time. However, it is not economical to adopt such a system for the MU/Meteor Monitor. Therefore we employ a similar method used for the meteor radar observations described in Section 2.2.1. That is, we search received signal pulse by pulse on the meteor detection hardware, and only when the signal intensity exceeds a threshold value for some successive pulses, we fix the sample range, and then record the signal only at the specified range into memory on PC for a certain duration (about 1 sec).

In designing the meteor detection hardware there are two important points to be considered.

1. The improved system must synchronize with the MU radar. In particular, data transfer rate must be very fast with the maximum value of 1 MHz.
2. The system treats the decoded signal which is as much as 19 bit digitized.

We could not find a general purpose hardware to process above signal, therefore we developed a hardware exclusively designed for meteor observations. We decided not to conduct coherent integration in order to precisely investigate time evolution of the meteor echo, which is also preferable to simplify the hardware.

Moreover, meteor echoes should be obtained under various observation parameters which might not be relevant for meteor observations, thus, there would

	Stratosphere	Mesosphere	Ionosphere
Date	24 Jan 1994 3:42-5:11 LT	15 Nov 1993 10:03-11:20 LT	24 Jan 1994 2:10-3:12 LT
Sample range	39.6-44.25 km	99.15-117.75 km	82.5-231.3 km
Beam directions	Zenith ($\theta = 0°$) Northward ($\theta = 10°$) Eastward ($\theta = 10°$) Southward ($\theta = 10°$)	← ← ← ←	← ← ← ←
Range resolution	150 m	600 m	4800 m
Inter pulse period	400 μ sec	1460 μ sec	10000 μ sec
Pulse compression	16 bit complementary	←	13 bit Barker
Coherent integration	1	1	1
Number of receiving antennas	1	1	1

Table 2.3: Parameters of emulation observations for the external interferometer system

be some additional problems. Therefore, in order to find these problems we conducted preliminary observations using parameters similar to those used for normal turbulence echo (stratosphere and mesosphere) and IS observations. Table 2.3 shows the observation parameters. Coherent integration was not conducted, which, however, increased obtained data more than the limit of the memory of the MU radar. Therefore, we compromised by reducing the number of beam directions from 5 to 4 as well as sample ranges. Reception was done with single three-element Yagi antenna. All the received signal was stored on a magnetic tape regardless of the existence of meteor echoes, and then used for further offline analysis.

According to these experiments we found two problems to be solved with the MU/Meteor Monitor as follows:

3. Flip code technique is sometimes adopted in order to subtract an offset involved in received signal. That is, phases of adjacent two pulses are 180° shifted each other in transmission. Since we do not apply any coherent integration, it is necessary to remove the offset for every pulse.

4. Since antenna beam direction is not fixed, but normally altered for every transmitted pulse, echo intensity may significantly vary pulse by pulse and exceed a threshold value only for a part of antenna beam direction.

In order to make the hardware flexible and simple, we solved the problems 3 and 4 mainly with a software on PC.

Figure 2.17 shows the blockdiagram of the designed meteor detection hardware. Three sets of 19 bit digitized complex signals (I, in phase and Q, quadrature components) are sent from the realtime processing system. To simplify the hardware only one of the three complex signals is searched to detect meteors. After subtracting offset values, which are specified by a software on PC, from I and Q, instantaneous signal intensity is estimated using the sum of the absolute value of I and Q, i.e., $|I| + |Q|$, in stead of $\sqrt{I^2 + Q^2}$ in order to reduce calculation time. The maximum ratio between the two estimations is only $\sqrt{2}$, which is almost negligible considering the large time variation of meteor echo intensity ranging to some tens of dB. During one IPP (Inter Pulse Period) cycle the hardware holds only one range value where the maximum echo intensity is detected. This algorithm is similar to that employed by the meteor radar system described in Subsection 2.2.1 and useful to reduce data transfer rate between the hardware and the PC and also to simplify the system. When some successive echo intensity at a certain range satisfy a condition to be recognized as a meteor echo, the realtime processing software on PC fixed the range and store the three sets of complex signals on the hard disk for a specified duration ($\sim$ 1 sec).

In estimating the offset involved in the receiver we have to separately treat I and Q signals and also positive and negative pulses of flip code. Figure 2.18 shows the relation between average time and averaged signal values in the case of mesosphere observation parameters. The signals became fairly flat after averaging over 500 pulses ($\sim$0.5 sec). In the case of stratospheric parameter signals were also converged after averaging for about 500 pulses ($\sim$0.2 sec). While, in the case of IS observation parameter only several pulses was enough for the averaging, due to the good SNR obtained by using the long transmitting pulse and narrow filter width in reception. We decided to average the echo intensity over 500 pulses at the beginning of the observations, and set the obtained offset values to the register of the meteor detection hardware.

Next we developed algorithm to solve the problem 4. Figure 2.19 presents an example of a meteor echo, where echo intensity revealed a clear periodic variation corresponding to the beam swinging. Therefore, we decided to search echoes beam by beam as follows. When echo intensity for a certain antenna beam exceeds a threshold value at a certain range for two consecutive pulses, the realtime processing software on PC fixes the range value and store data in the hard disk.

Having decided all the algorithm for the MU/Meteor Monitor we estimate expected number of meteor echoes with the system here. Numbers of echoes detected by using the algorithm stated above were 4, 20 and 65 for stratospheric,

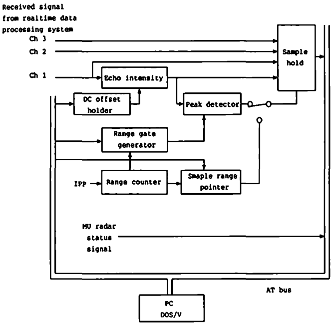

Figure 2.17: A blockdiagram of the meteor echo detection hardware.

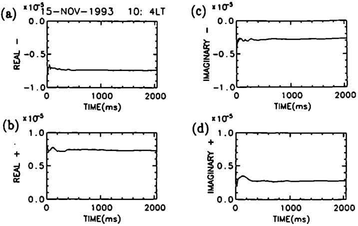

Figure 2.18: An example of the relation between averaging time and averaged echo intensity obtained using mesosphere observation parameter. (a): negative pulse of flip code of I, (b): positive pulse of flip code of I, (c): negative pulse of flip code of Q and (d): positive pulse of flip code of I.

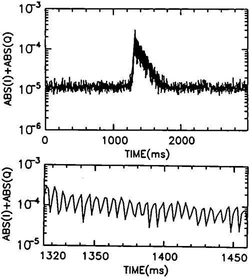

Figure 2.19: An example of the time variation of meteor echo intensity calculated after subtracting offset value. A part of the top panel is enlarged in the bottom panel.

mesosphere and IS observation, respectively, during 1 hour observation. Since this experimental setup consumed much more time for data transfer than those of usual observation parameters, the effective observation time was 4, 11 and 50 min, respectively. The loss time is expected to be almost negligible when we conduct meteor observations with the MU/Meteor Monitor. Further, sample range, which was rather limited in the experiment, can be largely expanded. Assuming the local time and range distributions obtained using a pencil like beam, number of meteor echoes per day are estimated to be as large as 5000–6000 and about 6000 for mesosphere and IS observations, respectively, although the number of meteor echoes in the actual observations will be somewhat smaller than these values, because observation parameter is frequently altered and some parameters will not be necessarily suitable for meteor observations.

2.2.4 Observation Periods

In this subsection we present observation periods of data set used in this study obtained with the meteor wind radar observations and the meteor observations with the MU radar.

The meteor wind radar started operation in Shigaraki in 1977. In 1983-1986 continuous observations was carried out by the automatic observing system for 24 hours as shown in Figure 2.20 and a large observational data base for the meteor height of 80–110 km has been stored.

In October 1992 we transported the meteor wind radar to Indonesia and started operation from November 1992. Observations were carried out fairly continuously, as shown in Figure 2.21, except for several major gaps, such as in September–December, 1993 and May–June 1994.

Meteor observations with the MU radar was carried out on campaign basis, where each observation period was 2 to 7 days. Observation periods are illustrated in Figure 2.22 and basic observation parameters for each observation periods are listed in Table 2.4 together with total underdense echo numbers.

2.3 Distribution of Meteor Echoes

In studying atmospheric phenomena it is important to know observable time-height range and resolutions of instruments we employ. Further, especially for meteor echo measurements, echoes are not expected to be sampled from a confined small area, but from a rather widely spread area. In this section we first present zenith angle and horizontal distributions of observed echoes, and then their time-height distributions. Further at the end of this section we describe a method to

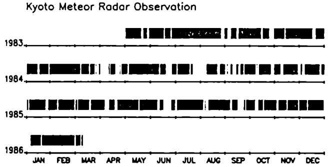

Figure 2.20: Observation periods of Kyoto meteor wind radar in 1983-1986

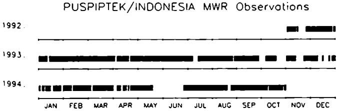

Figure 2.21: Observation period of Jakarta meteor wind radar (as of October 1994).

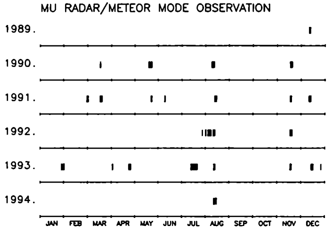

Figure 2.22: Periods of meteor observations with the MU radar.

Year	Start Time		End Time		Duration	Total	Pulse Width	Coherent Integration	Inter Pulse Period	Pulse Code
	Date	LT	Date	LT	HR	Echo	(μ s)	Times	(μ s)	
1989	Dec. 10.	15	Dec. 11	15	24	783	6	8	1600	B13
	Dec. 11.	16	Dec. 12	16	24	1234	6	8	1600	B13
1990	May 18	17	May 23	24	127	16288	6	8	1600	B13
	Aug. 08.	14	Aug. 12	17	99	14027	6	8	1600	B13
	Nov. 16.	21	Nov. 19	07	58	10474	6	8	1600	B13
1991	Feb. 27	18	Mar. 01	19	49	6772	6	8	1600	B13
	Mar. 15	16	Mar. 19	17	97	17084	6	8	1600	B13
	May 21	13	May 23	12	47	8488	6	8	1600	B13
	Jun. 08.	03	Jun. 09	18	39	6921	6	8	1600	B13
	Aug. 12.	21	Aug. 15	15	66	9038	6	8	1950	C16
	Nov. 16.	21	Nov. 18	09	36	8019	8	8	2560	C16
	Dec. 10.	02	Dec. 13	08	78	15438	8	8	2560	C16
1992	Jul. 31	23	Aug. 1	08	09	3408	15	4	2560	C8
	Aug. 03	12	Aug. 08	09	117	23415	8	4	2560	C16
	Aug. 10.	12	Aug. 13	11	71	7314	6	8	1950	C16
	Nov. 16.	13	Nov. 18	14	49	10169	8	8	2560	C16
	Nov. 18.	14	Nov. 19	15	25	3012	8	4	1280	C8
1993	Jan. 28	19	Feb. 01	11	88	17997	8	4	2560	C16
	Apr. 01	09	Apr. 02	08	23	3086	8	4	1280	C8
	Apr. 22	16	Apr. 25	19	(night)	5415	8	8	2560	C16
	Jul. 12	18	Jul. 19	18	169	26256	8	8	2560	C16
	Aug. 11.	01	Aug. 13	18	65	13743	6	8	1950	C16
	Nov. 16.	11	Nov. 18	11	48	10148	8	8	2560	C16
	Dec. 13.	16	Dec. 16	09	65	13743	8	8	2560	C16
1994	Aug. 11.	13	Aug. 15	08	91	27542	6	8	1950	C16

Table 2.4: Observation periods, total underdense echo numbers and basic parameters on meteor observations with the MU radar. B13, C8 and C16 represent 13 bit Barker code, 8 bit and 16 bit complementary codes, respectively. Observation periods footnoted with asterisks corresponded to periods of major meteor showers.

delineate time-height section of wind velocity from meteor echo data using a least square fitting.

2.3.1 Zenith Angle and Horizontal Distribution

We study here the distribution of meteor echoes as a function of the zenith angle and horizontal distance, which seems to be affected by two independent factors: first, the systematic configuration of the radar observations, such as the transmitting antenna pattern and the geometry between the radar and meteor trails, and second, the intrinsic distribution of the impinging meteors.

Jakarta Meteor Radar Observations

Figure 2.23 shows zenith angle distribution for the northward antenna beam on July 1–31, 1993. Echoes were widely distributed from 10° to 70°. The distribution showed a maximum around 60°, although the transmitting and receiving antennas were steered to 45° off zenith. From visual meteor observations it is known that provability function of radiants of meteors is approximately proportional to $cos(\theta)$, where θ is zenith angle [*McKinley*, 1961]. If we simply apply this relation to radio meteor echoes, we can expect more echoes at larger zenith angle because of the specular reflection due to the Fresnel scattering. However, since meteor echo power highly depends on range between the meteor trail and the radar as shown in Eq. 2.5, echoes from meteor trails at large distance, namely at large zenith angle, would be severely attenuated. Thus, zenith angle distributions are thought to be determined in a manner balancing the natural distribution of meteor radiants and the system factors such as antenna radiation pattern and receiver sensitivity, resulting in the maximum distribution around 60° in the case of present observations.

Note that Figure 2.23 showed slight enhancements at 48°, 60° and 70°, for which we could not give a satisfactory explanation. They might be caused by the fact that antenna radiation pattern was somewhat modified due to interferences between the direct and reflected radio waves. As described in Appendix C, zenith angle distribution for the southward antenna beam was superimposed by clear irregular enhancements which was successfully explained as the effect of the interferences by considering the local topography. Since it is preferable that these enhancements are small when we investigate true spatial distribution of meteor echoes, we have been employing the northward antenna beam since June 9, 1993.

Next we present distribution on the horizontal plane in Figure 2.24, where echoes showed a fan-shaped distribution because echoes were assumed to be received with the first lobe of the interferometer as discussed in Subsection 2.2.1.

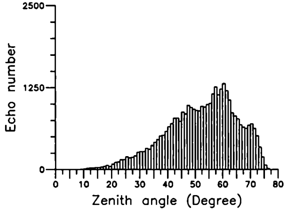

Figure 2.23: Zenith angle distribution of meteor echoes observed in Jakarta with the northward antenna beam on July 1-31, 1993.

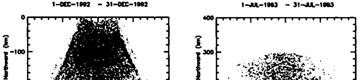

Figure 2.24: Horizontal distribution of meteor echoes observed in Jakarta with the southward antenna beam on December 1-31, 1992 (left) and the northward antenna beam on July 1-31, 1993 (right).

Note that we can see slight enhancements at the west and east edges of the distributions, which would be due to the ambiguities of arrival angles. Echoes were scattered in an area of as wide as 300 km × 300 km. The effective centers of observation areas were about 120 km to the south and north of the radar site for the southward and northward beams, respectively, corresponding to (7.4°S, 106.7°) and (5.3°S, 106.7°), respectively.

MU radar Observations

We first discuss the effects of the transmitting antenna pattern on the distribution [*Nakamura et al.*, 1991]. Figure 2.25 is a histogram of the number of meteor echoes at every 2.5° of the zenith angle(θ) for 24 hour observations on December 10–11, 1989 using a pencil-like antenna beam by exciting 21 subarrays other than 4 subarrays exclusively used for reception indicated in Figure 2.7. Note that the shape of this radiation pattern was almost the same with that obtained using all the 25 subarrays shown in Figure 2.9 although the peak gain at zenith angle of 0° became smaller by 1.5dB. The distribution in Figure 2.25 had a peak at $\theta = 30° - 40°$, although the radiation pattern of the transmitting antenna has a large gain at small θ. In fact only two echoes were detected in the main beam.

It is noteworthy that the zenith angle dependence of the meteor echo distribution is not greatly affected by the antenna pattern, but it is mainly determined by the geometrical configuration between the radar and the meteor trail. That is, in order to receive the intense meteor echoes due to Fresnel reflection, the trajectory of a meteor trail must be perpendicular to the propagation direction of the transmitted radio waves. Because the meteor trails that are nearly parallel to the ground are few in number, the main beam and side lobes near the zenith do not significantly contribute in the detection of meteor echoes.

Since the zenith angle distribution of meteor echoes has a peak at $\theta = 30°$ to 40°, the meteor echo rate seems to be increased, if the transmitted radio waves are concentrated at relatively large zenith angles rather than into the zenith. We, therefore, designed a doughnut-like radiation pattern with a peak gain at $\theta = 30°$ by controlling the phase of the radio wave transmitted from each Yagi antenna as discussed in Subsection 2.2.2. Note again that since we excited 21 arrays in this experiment, radiation pattern was somewhat modified from that shown in Figure 2.9, although the antenna gain at 30° was larger than that of the pencil-like pattern by more than 5 dB. Figure 2.25 shows the meteor echo distribution obtained using the doughnut-like beam pattern on December 11-12, 1989, which clearly shows that this antenna pattern is effective in increasing the meteor echo rate at $\theta = 25°$ to 40 °. The total echo rate over 24 hours was also increased to 1,300, which is about 1.6 times more than that with the pencil-like beam. Thus, after December 1989 we mainly used a doughnut-like beam pattern

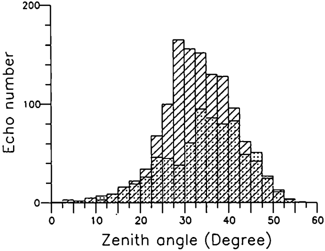

Figure 2.25: Distribution of meteor echoes with zenith angle. Results obtained using a pencil-like antenna pattern on December 10–11, 1989 (dotted) and a doughnut-like antenna pattern on December 11-12, 1989 (oblique lined) are plotted [*Nakamura et al.*, 1991].

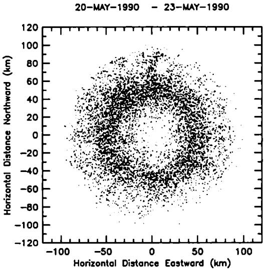

Figure 2.26: An example of horizontal distribution of meteor echoes observed with the MU radar using a doughnut-like transmitting antenna pattern on May 20-23, 1990.

for transmission, which is obtained by using all the 25 antenna arrays as shown in Figure 2.9.

Figure 2.26 shows a typical example of horizontal distributions of meteor echoes for observations using the doughnut-like beam conducted on May 20-23, 1990. Echoes were widely distributed within a circle centered at the radar site with a diameter of about 200 km, where majority of echoes were detected on a circle whose diameter is about 100 km, which corresponded to the zenith angle of around 30°.

2.3.2 Time-height Distribution

Height Distribution

Figure 2.27 shows typical height distributions of meteor echoes observed with the MU radar and Jakarta meteor radar. Distribution for the MU radar was confined in 70–105 km altitude, indicating the validity of the assumption used to eliminate ambiguities of arrival directions described in Subsection 2.2.2. Mean value and standard deviation were 87.8 km and 5.7 km, respectively. While, the meteor radar observations exhibited a wider distribution ranging from 70 km to 110 km with a mean and standard deviation of 91.9 km and 7.0 km, respectively. Some part of these differences was due to the employment of different radio wavelengths between the radars, that are, 6.45 m for the MU radar and 9.50 m for the meteor radar. As mentioned in Section 2.1 the effects of initial radius and finite impinging velocity to the attenuation of echo power are severer for observations using shorter radio wavelength. Further, the real time processing software could detect echoes whose duration time was longer than about 80–100 msec for the MU radar and 50 msec for the meteor radar, indicating that the meteor radar could observe echoes at higher altitudes.

Time Distribution

Next we study the diurnal variations of meteor echo rate. Number of meteor echoes observed depends on both intrinsic and system factors. One of the major intrinsic factors is a diurnal variation of meteor echo rate [*Sugar*, 1964]. On the morning side of the earth, meteors are overtaken by the forward motion of the earth as it revolves around the sun. On the evening side only meteors reaching the earth can be observed. Kyoto meteor radar observations have revealed the fairly sinusoidal variation of meteor echoes with local time, and a very low meteor echo rate in late afternoon [*Aso et al.*, 1980]. It is sometimes difficult to construct uniform data series as a function of local time due to such large diurnal variation of the echo rate [e.g., *Tsuda et al.*, 1987].

Kyoto meteor radar observations have also revealed that the local times of the maximum and minimum echo rates vary depending on the azimuth angle of the main beam of the five-element Yagi antennas. That is, when the main beam was steered toward the north and east at a zenith angle of 45°, the local time of the maximum echo rate was 6 LT and 8–9 LT, respectively. This azimuth angle dependence could be qualitatively explained [*Sugar*, 1964, *Hines*, 1956]; as the earth rotates, the position of the predominant radiants of sporadic meteors change relative to the antenna beam direction, and the location of "hot spot" moves around. Since the antenna used in the MU radar observations has omni-directional pattern, it can be expected that the diurnal variation of the meteor

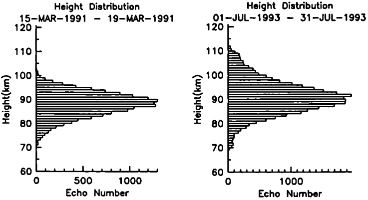

Figure 2.27: Examples of height distribution of meteor echoes; observations in Shigaraki with the MU radar on May 20–23, 1990 (left) and observations in Jakarta with the meteor radar on July 1–31, 1993 (right).

echo rate is rather smoothed out because of overlapping diurnal changes in the meteor echo rate with various azimuth angles, which is more suitable for the continuous monitoring of diurnal variations of wind fields. Figure 2.28 shows the local time dependency of meteor echo rate observed with the MU radar on May 20-23, 1990 using a doughnut-like transmitting antenna beam, where meteor echo rates obtained in the azimuth angle range of 315°-45° (northward section), 45°-135° (eastward section), 135°-225° (southward section) and 225°-315° (westward section) are also plotted. The total echo rate exhibited no clear maximum and minimum but fairly flat ones at 2100-0800 LT and 1000-1800 LT, where their ratio was only about two. While, distributions in the sectors were highly variable with each other. Clear maximums were seen at 0200 LT, 1500 LT for the north and east sections, respectively, and at 2100 LT and 0800 LT for the west section, but the south section was quite flat. General feature of these variations is explained by the effect of the earth's rotation. However, minute structure such as a marked enhancement at 1500 LT for the westward section might to be affected by other factors like meteor showers. Superposition of these variations made the distribution much smoother and enabled us to conduct observations without data gaps.

The numbers of underdense meteor echoes observed with the MU radar are summarized in Table 2.4, where the echo acquisition rate was as high as 3000-5000 per day since May 1990, owing to the improvements of the design of transmitting antenna pattern as well as the real time meteor echo detection procedure as discussed in the previous section. It is notable that the echo rate was almost the same between the periods of meteor shower (see Table 2.4, dates footnote with asterisks) and the periods with no significant shower activities, suggesting most of the meteor echoes observed with the MU radar were those of sporadic meteors. As a result, fine time-height variations of D and wind fields can be delineated about every 1 hour and 1 km throughout a day regardless of the existence or nonexistence of meteor shower activities.

On the other hand Figure 2.29 shows typical examples of local time dependency of underdense meteor echo rate in Jakarta for the southward and northward beams, revealing similar diurnal variations with clear peaks at 04 LT and 05 LT, respectively. The discrepancy from the MU radar observations, where difference between the north and south sections was very clear, is attributed to the latitudinal difference [*Sugar*, 1964].

Figure 2.30 presents seasonal variations of daily underdense echo rate obtained with Jakarta meteor radar, where observations were carried out fairly continuously except for several major gaps, such as in September-December, 1993 and May-June 1994. Typical echo number was 500-1200 per day. The clear seasonal

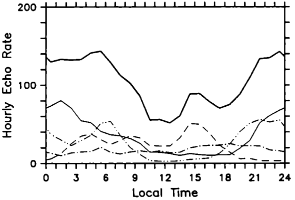

Figure 2.28: Mean diurnal variations of meteor echo rate observed on May 20–23, 1990 with the MU radar using a doughnut-like beam (thick solid line). Note that the meteor echoes received from the north (315°-45°), east (45°-135°), south (135°-225°) and west (225°-315°) are counted separately and are plotted as thin solid, thin dashed, thin dot-dashed and thin double dot-dashed lines, respectively.

variation in Figure 2.30 was due to at least three factors. One is the effect by the tilt of the Earth's axis relative to the ecliptic plane [*Hawkins*, 1956a], which could change echo rate by factors as large as 1.4. Another is the effect by the distribution of meteorite in the interplanetary space, which is thought to be not uniform along the Earth's orbit, but concentrated so as to produce a maximum incidence of meteors at the earth in July and a minimum in February [*Hawkins*, 1956b, *Sugar*, 1964]. And the other is the effect caused by altering the antenna beam direction from southward to northward on June 9, 1993.

2.3.3 Least Squares Fitting Method

Since meteor echoes are distributed widely in large spatial area as described in the previous subsections, it is necessary to reconstruct wind velocity and D from observed radial wind velocities and echo intensity, respectively. We first present methods to delineate time-height section of horizontal wind velocity and D, then

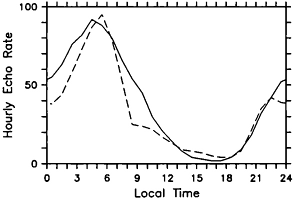

Figure 2.29: Monthly mean diurnal variations of meteor echo rate observed in Jakarta with the southward beam in December 1992 (solid line) and the northward beam in July 1993 (dashed line).

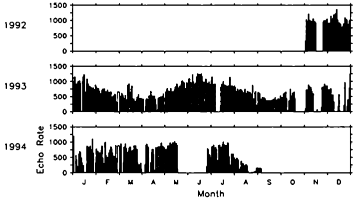

Figure 2.30: Seasonal variation of daily underdense meteor echo rate observed with the Jakarta meteor wind radar. Observations in November 2, 1992–March 10, 1993 and March 18–Jun 8, 1993 were conducted using the southward antenna beam, while observations during the other periods were conducted with the northward antenna beam.

we evaluate time-height resolutions of wind velocity and D measurements of each radar technique based on the meteor echo distributions.

The radial wind velocity of each meteor echo, v_r, is expressed as

$$v_r = l \cdot u + m \cdot v + n \cdot w \tag{2.28}$$

where u, v and w are eastward, northward and vertical wind component. Here, we can neglect w because the periods of the wind fluctuation of our interest by the meteor observation is usually longer than 1–2 hours, and w of these frequency is much smaller than u and v. Therefore, Eq.2.28 is simplified as

$$v_r = l \cdot u + m \cdot v \tag{2.29}$$

Assuming that wind velocity is constant in a given time-height bin, the wind component u and v can be determined in a manner, with the residual given by the following is minimized:

$$\epsilon^2 = \sum_{i=1}^{N}(v_{ri} - l_i \cdot u - m_i \cdot v)^2 \tag{2.30}$$

where N is the number of echoes in a given time-height bin. Although it is possible to calculate horizontal wind velocity with two echoes per time-height bin, we determine horizontal wind velocity only when N exceed 4 to exclude spurious values caused by measurement error.

As for D we calculate a mean value in a time-height bin also only when N exceeds 4. Mean value is obtained by averaging logarithm of D values at each time-height bin because the logarithm of D values at a fixed height shows a Gaussian distribution as shown in Section 3.2. Each D value sometimes show unrealistical values due to contamination of noise and overdense type echoes which can not be completely omitted. Therefore, we first calculate a mean value of D, X_D, and standard deviation, σ_D, for each time-height bin, then eliminate echoes with D values out of $X_D \pm 1.65\sigma_D$ which corresponds to 10 % of the total echoes. Finally values of X_D and σ_D are recalculated and used for further analyses.

Note that for the meteor radar observations in Jakarta height measurements of echoes at large zenith angles are not accurate enough to determine D profile. Thus, as a compromise we use echoes only at zenith angles smaller than 60 ° for the calculation of X_D and σ_D. Since echoes at zenith angles larger than 60° are not so large in number, effective centers of horizontal distributions of echoes at zenith angles smaller than 60° are almost the same with those of all the echoes used for wind velocity calculation.

Considering the time-height distribution of meteor echoes the MU radar observation has fine time-height variations of wind velocity and D about 1 hour and 1 km at 75-95 km throughout a day regardless of meteor shower activities. While the improved meteor wind radar has a time-height resolution of about 1 hour and 4 km at 80–100 km except for evening hours when meteor echo rate is relatively low.

2.4 Discussion and Conclusions

This chapter was devoted to the description of observation techniques using radio meteor echoes with a meteor radar and the MU radar.

In Section 2.1 we reviewed characteristics of radio meteor echoes. A meteor leaves an ionized long column along its pass, called a meteor trail, which reflects radio waves in HF and VHF bands. Echoes from the meteor trail involves a Doppler frequency shift, from which we can infer radial wind velocity of neutral atmosphere. Moreover, decay time constant of meteor echo intensity enables us to delineate ambipolar diffusion coefficient, which is a function of atmospheric temperature and density.

In Section 2.2 we first discussed system requirements for observations of atmosphere using a radio meteor echo. An antenna with a wide omnidirectional radiation pattern is prefered to collect large number of echoes because meteors appear randomly in large spatial area. Further an interferometer in reception is necessary to accurately determine meteor echo direction and reflection height. Sophisticated realtime processing softwares are also required.

A meteor wind radar of Kyoto university, which was originally constructed in 1977 in Shigaraki (35°N, 136°E), Japan, is an economical and transportable system. The radar employed single and three five-element Yagi antennas, with a half power width of as large as 60° in one way pattern, for transmission and reception, respectively, where the three receiving antennas compose an interferometer. We transported the radar to a newly established observatory near Jakarta, Indonesia (6°S, 107°E) in October 1992 for observations of equatorial mesopause region after replacing a transmitter, system-installed computer and antennas. We provided the radar with substantial auto-recovery functions for a long period of unmanned observations. Antennas were steered to north-south directions with 45° off zenith angle. The meteor radar observations have been carried out fairly continuously since November 1992 except for some major gaps.

The MU radar in Shigaraki was also applied for meteor observations by fully utilizing its versatility. We obtained a doughnut-like transmitting antenna pattern with a peak at a zenith angle of 30° by controlling phases of each antenna, which was proved to be effective to collect larger number of echoes than a pencil-like pattern of normal MU radar observations. We constructed an interferometer using four receiving antennas, whose accuracy was 0.3–0.6 km in altitude at a zenith angle of 30° and a range of 100 km, being sufficient enough for studying minute vertical structure of wind fields and diffusion coefficient. The MU radar observations were conducted for about 30 times during 1989–1994 on campaign basis with duration of 2–7 days.

Further, we proposed an improved meteor observation system with the MU radar equipped with external receiving antennas, a meteor detection hardware and a personal computer, which enables us long period observations by collecting meteor echoes under operation of various observations with the MU radar. We found that cross dipole antenna had an advantage of gathering a lot of meteor echoes in reception over the three element Yagi antenna in the MU radar. We designed a meteor detection hardware and developed softwares on the personal computer.

In Section 2.3 we present distributions of meteor echoes. The meteor radar observations in Jakarta revealed a wide zenith angle distribution ranging from 10 to more than 70°. Note that irregular enhancement was superposed on the zenith angle distribution when the antenna was steered toward southward presumably due to an interference between direct and reflected radio waves. Meteor trails were horizontally distributed in an area as large as 300 km × 300 km with a center at about 120 km south and north of the radar site according to the antenna beam direction. While, zenith angle distribution obtained by the MU radar showed a peak at 30–40°. Echoes were detected from all azimuthal angles within a circle with a diameter of about 200 km centered at the MU radar.

Meteor echoes were distributed in 70–105 km and 70–110 km altitude with a peak height of about 88 km and 92 km for the MU radar and the meteor radar observations, respectively. This difference seemed to be caused by the differences of employed radio frequency and meteor detection software.

Clear diurnal variations of meteor echo rate were recognized for the meteor radar observations in Indonesia with a maximum echo rate at 04–05LT. Daily echo rate showed a seasonal variation ranging from 500 to 1200. On the other hand, daily variations for the MU radar observations showed a remarkable azimuth angle dependency caused by a geometrical condition between the earth and meteoroids. Therefore, total daily variation was fairly smoothed out with a maximum to minimum ratio of only about 2 due to overlapping of daily variations of various azimuth angles. Daily echo rate was as much as 3000–5000. Owing to these fairly high echo acquisition rates we can determine wind velocity and ambipolar diffusion coefficient with a good time-height resolution of about 1 hr×4 km and 1 hr×1 km, for the meteor and the MU radar observations, respectively.

Chapter 3

Observations of Temperature Structure

We discuss in this section derivation of temperature perturbations from meteor echo measurements. Ambipolar diffusion coefficient, D, can be inferred from a decay time constant of meteor echo intensity (see Eq. 2.8), which is related to atmospheric temperature, T, and density, ρ. We develop in the following a relation between D and T perturbations. Since temperature is a one of key parameters in understanding atmospheric dynamics, its observations will greatly contribute to the study of the atmosphere if it is simultaneously realized with wind velocity measurements.

3.1 Relation between Ambipolar Diffusion Coefficient and Temperature

The effective diffusion coefficient for an electron in a meteor trail is shown as

$$D \sim D_i(1 + T_e/T_i) \tag{3.1}$$

where D_i is the diffusion coefficient for positive ion and T_e and T_i are the electron and ion temperature, respectively [*Kaiser*, 1953, *Weiss*, 1955]. Since the values of T_e and T_i can be taken equal [*Huxley*, 1952], we can assume

$$D \sim 2D_i \tag{3.2}$$

For a dilute system as we consider here, the diffusion coefficient, D_i and the mobility of ions, μ_i, are connected by the Einstein relation

$$D_i = \mu_i k T_i / e \tag{3.3}$$

where k is Boltzman's constant and e the electron charge. It is normally accepted that k is inversely proportional to the molecular concentration, i.e., atmospheric density.

However, there are some problems to estimate the value of μ_i. The main difficulty is the evaluation of temperature dependence of μ_i, since there is no simple relations between them [*McDaniel and Mason*, 1973]. For some ions the temperature dependence is shown to be negligible by laboratory measurements [*Weiss*, 1955, *Jones and Jones*, 1990], although it is not very easy to know the validity of the results in a realistic atmosphere. Further, the equation above is based on a single ion species being present. In practice the meteor trail may contain a number of different species, so the value of D corresponds to lumped or average mobility, which may not coincide with that for a specific species [*M. T. Elford*, private communication 1993].

A model was proposed for the dependence of D on temperature and density as follows

$$D \propto \frac{T^C}{\rho} \tag{3.4}$$

where C is a constant. Since the height variation of T is rather small near the mesopause compared with the exponential decrease of ρ, the D profile can be expected to show an exponential increase with a scale height close to that for ρ [e.g., *Greenhow and Hall*, 1960 ;1961]. It is noteworthy that scale height enables us to infer background temperature T by using a relation for an isotropic atmosphere

$$H = \frac{RT}{g} \tag{3.5}$$

where R and g are the gas constant and gravitational acceleration, respectively [e.g., *Holton*, 1992].

On the other hand, from Eq.3.4 the small perturbation of the ambipolar diffusion coefficient, D', can be expressed by using the temperature and density perturbations, T' and ρ', respectively, as follows:

$$\frac{D'}{D_0} = C\frac{T'}{T_0} - \frac{\rho'}{\rho_0} \tag{3.6}$$

where the suffix 0 denotes the time mean values. Under Boussinesq approximation, $\rho'/\rho_0 = -T'/T_0$, [e.g., *Stull*, 1988], Eq. 3.6 can be modified to

$$\frac{D'}{D_0} = (C+1)\frac{T'}{T_0} \tag{3.7}$$

Two possible values for C were adopted by earlier studies of radio meteor trail echoes to 1/2 [e.g., *Kaiser*, 1953, *Greenhow and Neufeld*, 1955, *Greenhow* *and Hall*, 1960, *Tsutsumi et al.*, 1994a] or 1 [e.g., *Weiss*, 1955, *Thomas et al.*, 1988, *Jones and Jones*, 1990], respectively. Difference between the two is attributed to the dependence of the ion mobility on T. That is, the former assumes the ion mobility to be proportional to $1/\sqrt{T}$, while the latter supposes to be negligible.

On the basis of experimental results, $C = 1$ seems to be more realistic in the atmosphere [*W. G. Elford*, private communication 1994]. As a matter of fact, we found that $C = 1$ gives a better consistency in terms of a ratio between potential and kinetic energy of gravity waves, which is discussed in more detail in Section 4.2. Thus we adopt $C = 1$, so that temperature fluctuations can be expressed as

$$\frac{T'}{T_0} = \frac{1}{2}\frac{D'}{D_0} \tag{3.8}$$

We present T'/T_0 in the following sections using this relation.

3.2 Seasonal Variations of Density Scale Height

In this section we present profiles of D together with seasonal variations of density scale height, using MU radar observations.

In Figure 3.1 (a) we show distribution of D as a function of height for observations on July 12-19, 1993, which basically indicates an exponential increase of D with height. Note that there are not many echoes with D larger than about 10 m^2/s, because a short lived meteor echo does not have a duration long enough to determine its decay time constant.

There were some attempts to infer the scale height, H_D, from height profiles of D, estimating as 26 km [*Murray*, 1959], 9.0±0.2 km [*Greenhow and Hall*, 1960], 7.8±0.3 km [*Greenhow and Hall*, 1961], and 8.4±0.64 km [*Hess and Geller*, 1976]. These values were generally larger than the density scale height, which is about 6 km near the mesopause in the CIRA86 model atmosphere.

Greenhow and Hall [1961] pointed out that the large H_D values reported by *Murray* [1959] were partly due to the fact that large D values were difficult to detect at high altitudes. Furthermore, we suspect that a part of the disagreement was caused by the less accurate height determinations with a resolution as poor as ±4 km [*Greenhow and Hall*, 1960].

We discriminated only good meteor echoes with sufficient SNR, for which the altitudes were more accurately determined. Practically, we chose echoes with peak SNR exceeding 30 dB and with zenith angles of smaller than 30°, then the standard deviation of the height determinations became less than 0.6 km. Moreover, we limited the height range to below about 94 km, where the D values are normally not clipped due to the system limit.

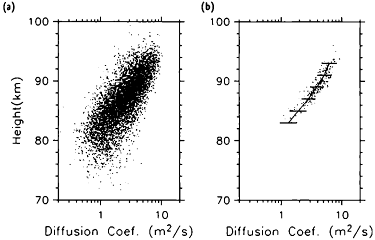

Figure 3.1: A scatter diagram of the diffusion coefficients observed on July 12-19, 1993, for (a) all the underdense meteor echoes and (b) the underdense meteor echoes with signal-to-noise ratios larger than 30 dB and arrival zenith angles of smaller than 30° (right).

We divided the selected data into layers with a thickness of 2 km and determined the mean values, as shown in Figure 3.1 (b), where the error bars represent the standard deviation, which was 30-40 % of the mean values. Since the measured height of a meteor trail involved an uncertainty of about 0.6 km, the corresponding error of the D values seemed to be about 10 % by assuming H_D=6 km, which was much smaller than the observed standard deviation. Therefore, the spread of D values at each height in Figure 3.1 (b) seemed to reflect the time variations of D.

The slope of the height profile seemed to change above 93 km altitude, presumably due to the clipping of large D values, exceeding about 10 m^2/s. So, we applied least square fitting to the profile only at 84-92 km in Figure 3.1 (b), and found H_D to be 6.1 km. Note that when we adopted the least square fitting to all the underdense meteor data at 84-92 km in Figure 3.1 (a), obtained values of H_D was 7.5 km, which is larger than that of the reduced data in Figure 3.1 (b) by about 20%.

The seasonal behavior of H_D is plotted in Figure 3.2, by using data obtained after August 1991 when echo reflection heights were more accurately determined with the improved interferometer (see Section 2.2.3). The density scale height, H, derived from the CIRA86 model shows seasonal variation with a maximum of 6.4 km in January and December, and a minimum of 5.4 km in June and July. While the observed H_D also showed seasonal variation, except for some enhancement in November and December.

During January to September, H_D ranged from 5.3 to 6.5 km, which was much closer to H compared with the results of earlier meteor studies. Further, no offset seems to exist between H_D and H in this period although samples are sparse during the first half of year. While, in November and December, H_D ranged from 6.7 to 8.1 km, which was larger than H by 6-24 %. Large year to year variations were also recognized between 1991 and the others. At present, we do not know the reason for the large H_D values in winter, though they might be caused by large perturbations of both temperature and density, as revealed by recent *Na* lidar observations [*She et al.*, 1991; 1993].

3.3 Diurnal Variations

This section treats temporal variations of T'/T_0, in particular, diurnal variation, determined from measurements of D'/D_0 using Equation 3.8. Although we used very limited number of meteor echoes for determinations of density scale height in the previous section, we include more underdense echoes, loosening the peak SNR to be larger than 10 dB. We discuss error in T'/T_0 estimation caused

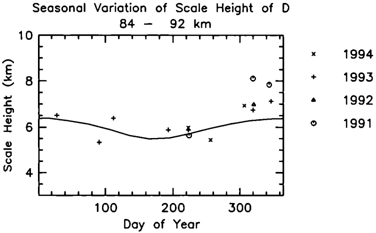

Figure 3.2: The symbols show the scale heights of the ambipolar diffusion coefficients at 84–92 km altitude for meteor observations with the MU radar from November 1992 to November 1994, see Table 2.4. The solid curve shows the density scale height at 84–94 km inferred from the CIRA86 model atmosphere.

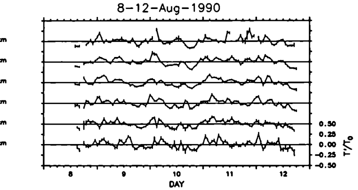

Figure 3.3: Time series of T'/T_0 every 2 km altitude from 84 km 94 km observed on August 8-12, 1990 in Shigaraki. Vertical bars indicate the confidence intervals of each observed values.

by using these data in Section 4.2.

Figure 3.3 shows time series of T'/T_0 observed on August 8-12, 1990 in Shigaraki. Amplitudes of T'/T_0 sometimes exceeded 0.25, corresponding to T' of more than 45 K assuming T_0 to be 180 K from CIRA 1986 model atmosphere. It is noteworthy that fluctuations with various periods were coherently observed between different altitudes. These fluctuations seemed to be caused by atmospheric waves such as gravity waves, atmospheric tides and planetary waves or direct heating of the atmosphere due to insolation of solar radiation. First we study diurnal component here, which is presumably fixed to local time, and therefore, can easily be analyzed compared with other components. We investigate shorter and longer components in more detail in Chapters 4 and 5, respectively.

Figure 3.4 shows the band-pass filtered time series of T'/T_0 with cut-off periods at 20 and 30 hr for data observed on August 8-12, 1990. We can see a clear diurnal variation with a positive peak at around 0300-0600LT throughout the observed height region at 84-94 km. The enhancement in the morning shows good consistency with earlier findings by meteor echo observations at middle to high latitudes [e.g., *Greenhow and Hall*, 1960; *Hess and Geller*, 1976 and *Devara et al.*, 1981.]

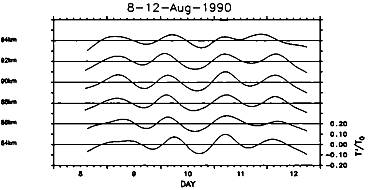

Figure 3.4: The same as Figure 3.3 except for band-passed filtering with cutoff periods at 20 and 30 hr.

We conducted harmonic analysis to obtain amplitudes and phases of diurnal variations for observations continued longer than two days. Figure 3.5 shows a typical example in summer months (May–August), observed on August 8–12, 1990, where T'/T_0 was converted to T' assuming T_0 to be 180 K from a model atmosphere [CIRA 1986]. Note that diurnal components of eastward, u', and northward, v', wind velocities are also plotted. For comparison numerical model by *Forbes* [1982], which is dominated by $S_{1,1}$ mode of diurnal tide, are also shown for summer solstice conditions. Amplitude of T' was about 12 K (6% in T'/T_0) at 80-95 km. The phase was fairly constant throughout the observed altitude range at 04-05LT, which is obviously different from the numerical calculation showing a clear downward phase propagation. While, phases of observed u' and v' indicated a clear downward phase progression with a vertical wavelength of about 30 km, showing a very good agreement with the numerical model, although observed amplitudes were less than a half of the model prediction.

On the other hand, the structure of T'/T_0 in winter sometimes showed a remarkable difference from that in summer when large amplitudes were observed in wind fields. Figure 3.6 shows an example for observations conducted on November 16–19, 1992. Amplitudes of u' and v' ranged 5–40 m/s, larger than those in Figure 3.5 at almost all the observed altitude range, and phases of T', u' and v'

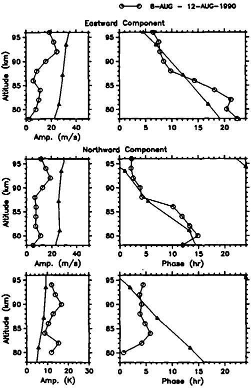

Figure 3.5: Profiles of amplitudes and phases of diurnal components of eastward wind velocity (top), northward wind velocity (middle) and temperature (bottom) on August 8-12, 1990 observed with the MU radar in Shigaraki. Note that observed T'/T_0 was converted to T' by assuming T_0 to be 180 K from CIRA 1986 model. Values of phases were defined as the time when fluctuating components had its maximum values. Model result at 36° for summer solstice conditions from *Forbes* [1982] is also plotted with triangles.

showed a clear downward progression with a similar vertical wavelength. Note that numerical model by *Forbes* [1982] for winter solstice condition showed quite similar phase structure between T', u' and v' although the absolute phase values were in consistent, that is, phases were systematically shifted by about 90° between the observations and the model. Amplitude profiles were also quite similar, although the amplitude of u' of the model is 1.2–1.3 times bigger than that of observations throughout the height region. The discrepancy in phase could be caused by the fact that the assumed background conditions of the model, affecting the propagation characteristics of diurnal tides such as temperature gradient, mean winds and eddy diffusion coefficient, [*Vial*, 1986; *Aso et al.*, 1987; *Vial*, 1989], were not necessarily identical with the real atmosphere during the present observation.

Next we investigate diurnal variation of T' observed with the meteor wind radar in Jakarta. Since a tidal model predicted that diurnal variation of T' is maximized at equator where propagating symmetric modes have their peak values [e.g., *Lindzen*, 1967; *Forbes*, 1982], larger T' value is expected in Jakarta than in Shigaraki. We also conducted harmonic analysis for Jakarta data collected from November 1992 to August 1994. Note that it was sometimes difficult to delineate wind velocity and temperature fluctuations, especially in the evening hours. because meteor echo rate was not so high as that for the MU radar observations. Therefore, we determined monthly mean daily variations by superposing 30 days of data, then we delineated diurnal component [*Tsuda et al.*, 1987].

Obtained phase values of T' often showed clear downward propagations with various vertical wavelengths ranging 20–50 km, suggesting a relation with propagating diurnal tides. Figure 3.7 shows such an example observed in April 1994 when clear downward phase propagations were seen in both wind and temperature fields. A numerical model by *Forbes* [1982] for an equinoctial condition is also plotted for comparison. In the figure observed amplitude of T'/T_0 was 2–7%, corresponding to T' of 4–14 K assuming T_0 as 190 K [CIRA 1986]. This value was comparable to those in Shigaraki seen in Figures 3.5 and 3.6. However, considering that the results in Jakarta were based on monthly average while those in Shigaraki on the campaign observations whose durations were shorter than one week, the amplitudes would be fairly larger in Jakarta than in Shigaraki. Observed amplitudes of u' and v' in Figure 3.7 were similar with each other as about 10 m/s, showing a general tendency to increase with height. While, the model amplitudes, especially for v' and T', show larger values than the observation.

Vertical wavelengths of v' and T' were quite similar between the observations and the model although the absolute values were somewhat different, that is, in the model phase leads by 2–4 hours for v' and is delayed by 2–7 hours for T'.

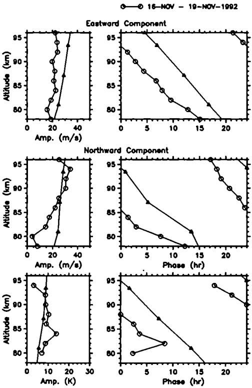

Figure 3.6: Same as Figure 3.5 except for observations on November 16–19, 1992. Model result at 36° for winter solstice conditions from *Forbes* [1982] is also plotted with triangles.

For u' phase of the observation and model showed similar values around 85 km altitude, but the vertical wavelengths were a little shorter for the observation.

Since the model is dominated by symmetric $S_{1,1}$ mode, these differences seem to suggest that in the actual atmosphere effects of higher order modes were not negligible, at least, during the present observation period.

Now we discuss the standing phase structure seen in T' profile in Shigaraki in summer. Evanescent diurnal tides such as $S_{1,-1}$ and $S_{1,-2}$ modes are predicted to show a considerable activity via modal coupling as $S_{1,1}$ mode is mechanically damped [*Forbes and Hagan*, 1988]. For these modes T' has a maximum value at middle to high latitudes, while wind velocity components have maxima at poles and are not large at middle latitudes as seen in Figure 1.5. Therefore, considering that Shigaraki is located at middle latitude it might be possible that evanescent modes could be observed only in T'. Another possible source of the standing phase structure is direct absorption of solar UV radiation.

3.4 Discussion and Conclusions

In this chapter we first studied a theoretical relation between atmospheric parameters and ambipolar diffusion coefficient, D, inferred from a decay time constant of meteor echo intensity. Employing a theory of ionic diffusion, we obtained a relation, $D \propto T^C/\rho$. The value of C was chosen to be 1, which is considered to be the most relevant from experimental results. Since T is fairly constant near the mesopause, scale height of D nearly corresponds to that of ρ, H, which is further related to background temperature. Using a Boussinesq approximation, we found a relation between the normalized D and T fluctuations as $T'/T_0 = 1/2D'/D_0$. Temperature fluctuations are one of the basic parameters to study atmospheric dynamics. Their observations enable us to obtain information to infer structure of atmospheric waves by combining simultaneous wind velocity observations.

The D profile, obtained with the MU radar in Shigaraki, showed an exponential increase with a scale height of about 6 km, which are very consistent with the density scale height estimated from a model atmosphere [CIRA86]. During November and December scale height of D showed large year to year variations, indicating atmospheric stability can be considerably changed around the mesopause region.

Observed T' involved fluctuations with various periods, showing coherent structure between different altitudes. In particular, we presented preliminary results of diurnal variations in this chapter, while short and long period components are presented in Chapters 4 and 5.

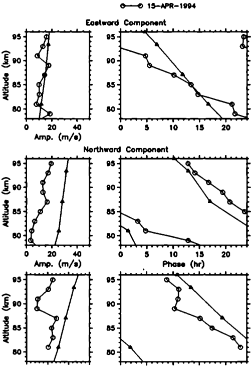

Figure 3.7: Same as Figure 3.5 except for observations in Jakarta in April 1993. Values of T'/T_0 are converted to T', assuming T_0 to be 190 K [CIRA 1986]. Results from numerical computations at 6°S by *Forbes* [1982] on equinoctial condition are also shown with triangles.

In Shigaraki a typical amplitude of diurnal variations of T' was about 10 K from campaign observations with durations of 2-7 days. While, their phase structure could be classified into two types. In summer phases were fairly constant along height at 04-05LT, being consistent with earlier findings using meteor echo measurements in middle to high latitudes. However, this phase structure was in contrast to that for horizontal wind component which usually showed a downward phase propagation. The standing phase structure implies a manifestation of an evanescent diurnal tides which dominated only in temperature fields in middle latitudes such as $S_{1,-1}$ and $S_{1,-2}$, or in-situ heating due to solar radiation. On the other hand, in winter they sometimes exhibited clear downward phase progression when large amplitudes were observed in wind components. For a typical example obtained on November 16-19, 1992, T', u' and v' had wavelengths of about 25 km. Moreover, relative phase relation among T', $u'$and v' was quite consistent with a model prediction by *Forbes* [1982], although the absolute phases were systematically shifted by 90° between the observations and the model.

In Jakarta monthly mean amplitude of diurnal variations of T' was about 10 K. This value was comparable to those in Shigaraki. However, considering that the results in Shigaraki was based on shorter period observations less than one week the amplitude of T' seemed to be fairly larger in Jakarta. While phases usually showed downward propagations for both the wind and temperature fields. But, they did not necessarily show a phase relation predicted by the model by *Forbes* [1982] which is dominated by $S_{1,1}$ mode diurnal tide, indicating that higher tidal modes had also significant amplitudes.

Chapter 4

Observations of Gravity Waves in the Mesopause Region

A number of theoretical studies have pointed out the important role of gravity waves in transporting energy and momentum from the lower atmosphere to the mesosphere and lower thermosphere [*Lindzen*, 1981; *Matsuno*, 1982; *Fritts and Rastogi*, 1985]. The behavior of gravity waves have been studied with various remote sounding and in-situ observation techniques, such as MST radar, MF radar, lidar, meteor radar and rocket measurements[e.g., *Vincent and Reid*, 1983; *Meek et al.*, 1985; *Yamamoto et al.*, 1986; *Tsuda et al.*, 1990; *Tsuda et al.*, 1992; *Nakamura et al.*, 1993]. Among them meteor observations have a great potential to simultaneously monitor wind and temperature fluctuations associated with gravity wave activities around the mesopause.

In this chapter we investigate the characteristics of gravity waves near the mesopause using the high resolution temperature and wind velocity data obtained with the meteor observations with the MU radar.

4.1 Temperature Fluctuations due to Gravity Waves

Figure 4.1 shows a band-passed time series of T'/T_0 with cut-off periods at 5 and 10 hr observed on May 19-23, 1990. It is noteworthy that wave-like structures showed downward phase propagation throughout the observation period, as indicated by dashed lines. Similar T'/T_0 with periods shorter than the inertial period (especially several to about 10 hr) were often detected during other meteor observations with the MU radar. Note that *Tsutsumi et al.* [1994a] studied gravity waves using the MU radar data adopting $C = 1/2$ in Equation 3.7. In

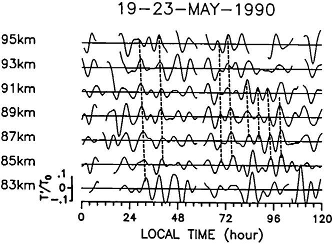

Figure 4.1: An example of band-passed time series of normalized temperature with cutoff periods of 5-10 hr on May 19-23, 1990.

this chapter we present revised results adopting $C = 1$ (Equation 3.8).

Here we compare T'/T_0 with fluctuations of wind velocity, which was simultaneously measured by using meteor echoes. Figure 4.2 shows the time series of T'/T_0 and wind velocity at 91km with cut-off periods at 5 and 10 hr observed on May 19–21, 1990. The correlation was quite good, especially between T'/T_0 and the eastward wind velocity, implying that the short period fluctuations in both T'/T_0 and wind velocity were generated by gravity waves.

In earlier studies of meteor echo observations only horizontal wind velocity was determined. It is expected that the simultaneous observation of temperature fluctuations will greatly facilitate a full understanding of atmospheric phenomena. Here we show an example of the analysis of gravity waves for meteor data obtained on December 10–13, 1991. In this period MU radar observations of turbulence echoes were interleaved every 15 min.

Figure 4.3 shows a contour plot of northward and eastward wind velocity after removal of the mean winds, where the meteor and turbulence echo observations are shown in the height ranges above and below the dashed lines, respectively. Turbulence echo observation with the MU radar is of great advantage in the

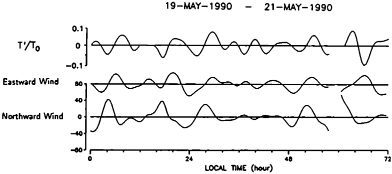

Figure 4.2: Band-passed time series of normalized temperature and wind velocities at 91 km with periods of 5-10 hr observed on May 19-21, 1990.

study of small scale atmospheric phenomena, though it is limited to daylight hours due to the low electron density at night. At the meteor height of 75-100 km, systematic wind motions were continuously observed throughout a day, even in the afternoon when the meteor echo rate is low. In particular, a wave with a period of about 12 hr and a vertical wavelength of about 15 km was dominant from 1200 LT on December 10, 1991, to 1200 LT on December 11, 1991. It is notable that this wave showed downward phase propagation continuously from the meteor echo height down to the turbulence echo region, a characteristic of gravity waves.

Figure 4.4 shows a contour plot of T'/T_0 on December 10-13, 1991, indicating a similar structure to that of the inertial gravity wave shown in Figure 4.3. Furthermore, this structure became unclear after 1200 hr LT on December 11, 1991, for both wind velocity and D, which also indicates the strong relation between the fluctuations of D and wind velocity.

Hodograph Analysis of a Gravity Wave

Bandpass filter with cutoff periods of 8 to 15 hr was applied to time series during December, 10-13 1991. Then hodograph and height profile at 2000 LT on December 11, 1991 were drawn, from which components with vertical wavelengths longer than 7 km were extracted (Figure 4.5). The amplitude of T'/T_0 was estimated from the wind velocity fluctuations (about 20 m/s) to be about 4 % by employing Equation 1.5. This value is smaller than the real amplitude due to

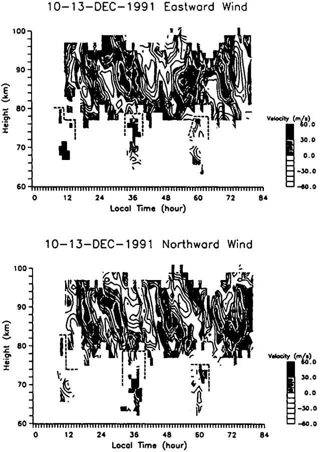

Figure 4.3: Time height sections of wind velocity observed on December 10–13, 1991. The two different observations were interleaved using meteor and turbulence echoes, time averaged wind velocity being removed. The meteor and turbulence echo observations correspond to the height ranges above and below the dashed lines, respectively.

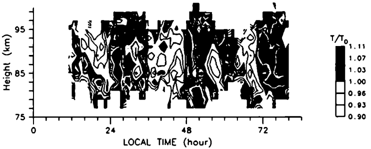

Figure 4.4: Time height sections of T'/T_0 observed on December 10–13, 1991.

the filtering, but it shows good agreement with the observed amplitude of T'/T_0. Since T_0 is about 200 K in the mesopause region [CIRA86], the fluctuation of 4 % corresponds to about 8 K.

The wind vector showed elliptical rotation, with the long axis aligned north-west to south-east. Temperature fluctuations were out of phase with both northward and eastward wind fluctuations by about 135°, therefore, the horizontal propagation direction of this wave is inferred to be north-westward from the polarization relation, Equation 1.5. The band-passed (8–15 hr) south-westward wind velocity, which was composed of zonal and meridional winds, and band-passed T'/T_0 are shown in Figure 4.6. The phases agreed fairly well up to 1200 LT on December 11.

For comparison we also analyzed the hodograph in Figure 4.7 for the height profile obtained on turbulence echo observation at 1400 LT on December 11, 1991, after subtracting the linear trend and removing the components with vertical wavelengths shorter than 7.2 km. Because the longer axis was roughly aligned east-west and the vertical wind component was anti-phase with the eastward wind component, the propagation direction of this wave can be inferred to be westward, which was fairly consistent with the results of meteor wind measurements, although they differed by about 45°. This discrepancy is thought to be mainly caused by the time evolution of the wave activity, that is, it was fairly clear during the meteor echo measurements, but at 1400 LT the wave structure began to become unclear at the meteor echo height region, when turbulence echo observations were conducted.

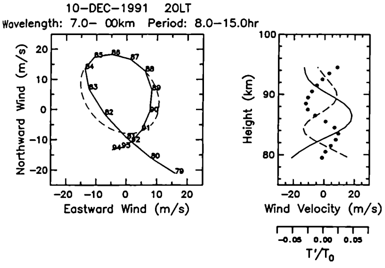

Figure 4.5: The hodograph and height profile obtained at 2000 LT on December 10-11, 1991. The wave components with periods of 8-15 hr and vertical wavelengths longer than 7 km were extracted. The numerals and dashed ellipse in the left panel indicate the height in km and least squares fit to the hodograph, respectively. The solid, dashed and dotted lines in the right panel denote the fluctuations of the northward wind, eastward wind and temperature, respectively.

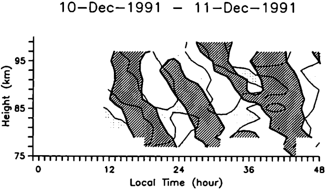

Figure 4.6: Contour plots of the south-westward wind velocity (thick solid curve) and normalized temperature (thin solid curve) after band-pass filtering with a cutoff of 8–15 hr obtained on December 10–11, 1991.

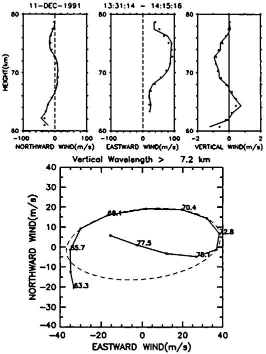

Figure 4.7: The height profiles of the northward, eastward and vertical wind velocity obtained on turbulence echo observations with the MU radar at 1400 LT on December 11, 1991 (top), and the hodograph (bottom). Solid lines and open circles in the top panel show the raw profiles and profiles after low-pass filtering with a cut-off vertical wavelength of 7.2 km, respectively. The solid line in the bottom panel corresponds to the filtered height profiles in the top panel, and the dashed line is a least squares fit to the hodograph.

4.2 Frequency Spectra of Wind and Temperature Fluctuations

In this section we investigate the amplitude relation between T'/T_0 and u' due to gravity waves in terms of frequency spectra. The frequency spectrum of potential energy can be expressed, by using that of potential temperature, $F_{\theta/\theta_0}(\omega)$, as [*Gage and Nastrom*, 1986]

$$\frac{1}{2}\left(\frac{g}{N}\right)^2 F_{\theta/\theta_0}(\omega) = \frac{1}{2}\left(\frac{g}{N}\right)^2 F_{T/T_0}(\omega) \tag{4.1}$$

Further the frequency spectrum of kinetic energy is expressed by the half of the sum of frequency spectrum of eastward and northward wind fluctuation, $F_{v'_e}$ and $F_{v'_n}$. From Eq. 1.5 it is expected that kinetic energy density is equal to potential energy density when ω is large enough compared with the inertial frequency.

Figure 4.8 shows spectra density of potential energy (dashed line) for the observations on December 13-16, 1993, adopting $2\pi/300$ rad.s^{-1} and 9.55 m^{2}s^{-1} for N and g, respectively at the altitude ranges of 83-93 km. The spectra for the kinetic energy are also plotted (solid line). The spectra was obtained by Fourier transforming an auto-correlation function with a maximum lag value of 24 hours. In the figure both the potential and kinetic energy show similar intensity with similar exponential decrease with frequency as well. Large discrepancy at lower frequency seemed to be caused by inertial gravity waves and atmospheric tides, whose relation between amplitudes of wind and temperature fluctuations are not subject to Eq. 1.5.

Note that we assumed 1 for the value of C in Equation 3.7. ***Tsutsumi et al.*** [1994a] presented generally larger values for potential energy than kinetic energy, which is because they adopted 1/2 for the value of C. In other words it can be said that the present results ascertain that C=1 is a better solution. While, the much larger potential energy in higher frequency range of ***Tsutsumi et al.*** [1994a] seems to be attributed to contamination of overdense type meteor echoes which raise the noise floor of the potential energy spectra.

Figure 4.9 showed potential and kinetic energy density at 88 km altitude for observations conducted in 1993-1994. Both spectra showed similar values in a period range shorter than 2 hours. The energy level was, however, highly variable in period ranges longer than 12 hours possibly due to the large temporal variations of atmospheric tides and also inertial gravity waves.

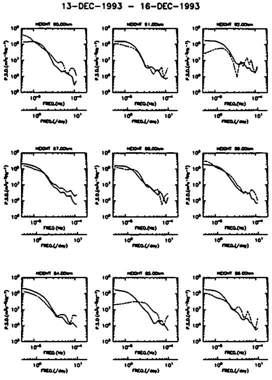

Figure 4.8: Potential energy density (dashed curve) calculated from T'/T_0 and kinetic energy density (solid curve) at altitude from 84 to 92 km for meteor observations with the MU radar conducted on December 13-16, 1993.

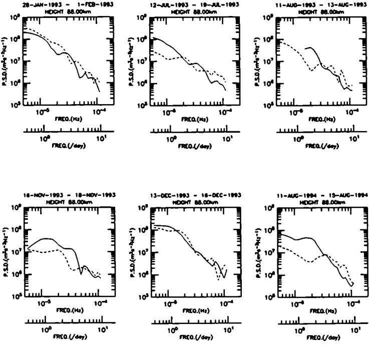

Figure 4.9: Same as Figure 4.8 except for 88 km altitude from observations conducted in 1993 and 1994.

4.3 Horizontal Propagation Characteristics

4.3.1 Seasonal Variations

Meteor echo observations with the MU radar often detected sinusoidal fluctuations in vertical profiles of wind and temperature fluctuations with vertical scales 5–20 km, which are most likely due to inertial gravity waves. In this subsection we study the seasonal behavior of the propagation characteristics of dominant gravity waves in vertical profiles adopting hodograph analysis [*Tsuda et al.*, 1990; *Nakamura et al.*, 1993].

We used 12 observation periods from May 1990 to November 1992 listed in Table 2.4. Wind velocity and T'/T_0 were determined every hour and 1km altitude. Since amplitudes and vertical wavelengths of propagating diurnal atmospheric tides were comparable to those of gravity waves, it was sometimes difficult to distinguish them. Therefore, the time series were band-passed with cutoff periods at 5 and 20 hrs to exclude diurnal tide. Moreover, we compared the bandpassed profiles with mean daily variations obtained by superimposing wind and temperature fluctuations into local time for each observation periods, which were thought to represent tidal components. Then, we picked up gravity waves when sinusoidal fluctuations were clearly seen for several hours only in the bandpassed profiles.

We analyzed hodograph for horizontal wind vectors of selected bandpassed profiles, and an ellipse was best-fitted to the hodograph at successive 5-15 km altitude. By using the polarization relation of gravity waves, Equation 1.2, intrinsic period was determined from the ratio between the major and minor axes of the ellipse. Horizontal propagation directions were detected from Equations 1.2 and 1.5 using the same criteria employed in Section 4.1. Other parameters of gravity waves such as horizontal wavelength and horizontal phase velocity were determined using the dispersion relation of gravity waves. Center of the profiles was at about 88 km on the average.

We detected 21 gravity wave events during the 12 campaign periods, and successfully fitted an ellipse to 16 cases. Fifteen cases out of the 16 hodographs exhibited clockwise rotations, while only one case, observed around 03–04LT May 23, 1990, showed anti-clockwise rotation, indicating that most of wave energy propagated upward. Further, horizontal propagation direction was determined for 14 events without ambiguity of 180°, except for the observations at 00–06LT November 18, 1990, when temperature profile did not show clear phase relation with wind profiles. Basic parameters of selected gravity waves are summarized in Table 4.1.

Resultant intrinsic periods were distributed from 6.8 to 14.0 hr with a mean value of 11.3 hr. Although the inertial periods in Shigaraki is 20.9 hr, the obtained

DATE	Period (hr)	λ_z (km)	λ_h (km)	c_{ph-h} (m/s)	c_{ph-z} (m/s)	Direction (Azimuth) (deg.)
20-MAY-1990 15-16LT	6.8	9.0	776	31.7	-0.37	125
21-MAY-1990 14-16LT	8.8	14.0	1618	51.4	-0.44	164
23-MAY-1990 03-04LT	9.7	12.0	1576	45.2	0.34	43
23-MAY-1990 19-20LT	12.8	12.0	2317	50.5	-0.26	24
09-AUG-1990 22-02LT	-	-	-	-	-	-
10-AUG-1990 14-16LT	12.5	16.0	2994	66.5	-0.36	-174
17-NOV-1990 10-12LT	-	-	-	-	-	-
18-NOV-1990 00-06LT	14.0	16.0	3620	71.8	-0.32	-
16-MAR-1991 08-14LT	12.3	13.0	2373	53.6	-0.29	-35
17-MAR-1991 06-11LT	12.4	14.0	2595	58.0	-0.31	-31
19-MAR-1991 06-13LT	11.9	13.8	2381	55.7	-0.32	-51
08-JUN-1991 18-02LT	9.8	11.7	1553	44.0	-0.33	81
13-AUG-1991 22-02LT	-	-	-	-	-	-
14-AUG-1991 19-05LT	13.8	11.3	2509	50.4	-0.22	53
17-NOV-1991 14-17LT	13.4	12.0	2498	52.0	-0.25	-157
18-NOV-1991 01-02LT	-	-	-	-	-	-
10-DEC-1991 20-8LT	13.4	13.3	2793	57.9	-0.28	-42
12-DEC-1991 02-06LT	7.7	11.0	1093	39.4	-0.40	-176
12-DEC-1991 22-24LT	-	-	-	-	-	-
17-NOV-1992 00-04LT	11.1	13.0	2043	51.1	-0.33	-152
17-NOV-1992 23-02LT	8.1	16.5	1752	59.7	-0.56	178
Mean Values	11.3	13.1	2195	52.9	-0.34	

Table 4.1: Basic parameters of dominant inertial gravity waves in the vertical profiles deduced using hodograph analysis. Intrinsic periods, vertical wavelength (λ_z), horizontal wavelength (λ_h), horizontal phase speed (c_{ph-h}) vertical phase speed (c_{ph-z}) and horizontal propagation directions are shown. Horizontal bars indicate that values could not be determined. Note that wind vector during 03-04LT May 23, 1990 showed anti-clockwise rotation with increasing height, thus values in this period were not used in calculating mean values shown at the end of the table.

longest period was limited to 14.0 hr, probably due to the bandpass filter of 5–20 hr in order to avoid the effects of diurnal tides. Vertical and horizontal wavelengths ranged from 11.3 to 16.0 km and from 776 to 3620 km with a mean value of 13.1 km and 2200 km, respectively.

Figure 4.10 shows the distribution of vertical wavelength as a function of intrinsic period with solid circles. For comparison also shown with open circles are the results by *Nakamura et al.* [1993], which studied dominant gravity waves in vertical profiles with hodographs using turbulence echo observations with the MU radar. Center height of their observations was about 70–75 km. There is a clear tendency that present observations show larger vertical wavelengths than *Nakamura et al.* [1993] which distributed from 4 to 15 km with a mean value of 8.2 km. Note that the largest vertical wavelength of the present study seems to be limited due to the fact that we selected gravity waves with vertical scales clearly different from those of upward propagating diurnal tides of about 25–30 km.

Murayama et al. [1992] reported dominant vertical scales of gravity waves by means of the MU radar, rocketsondes and radiosondes, which were 2–5 km, 5–15 km and longer than 15 km in the lower stratosphere, the upper stratosphere and the mesosphere, respectively. The present results were fairly consistent with, but slightly shorter than, their results in mesosphere, which might be due to the limit of the present study stated above. *Murayama et al.* [1992] interpreted the increase in the vertical scales with altitude in terms of the saturation of upward propagating gravity waves. It is reported that wave damping due to eddy diffusion, which increase with altitude, are also responsible for the change of dominant vertical scale [*Gardner and Voeltz*, 1987; *Nakamura et al.*, 1993].

Now we study horizontal propagation characteristics of the dominant gravity waves near the mesopause. Horizontal phase speeds of the present observations were distributed from 31.7 to 71.8 m/s with a mean value of 52.9 m/s. Those in middle mesosphere were reported to be about 30 m/s by *Nakamura et al* [1993]. *Tsuda et al.* [1994] showed using radiosonde observations near equator that typical horizontal phase speeds of dominant gravity waves in troposphere and stratosphere was 5–7 m/s and 12 m/s, respectively. These results indicate that the horizontal phase speeds are larger at higher altitudes. This may be partly due to the height variation of dominant vertical scale of gravity waves discussed above because horizontal phase speed is basically proportional to vertical wavenumber. Furthermore, directional filtering caused by mean winds might be responsible; only waves with sufficient horizontal phase speeds can propagate upward without being absorbed by mean winds.

The distributions of horizontal propagation directions are shown in Figure 4.11

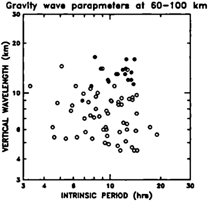

Figure 4.10: A scatter diagram of vertical wavelengths versus intrinsic periods of dominant gravity waves listed in Table 4.1 (solid circles). For comparison results from turbulence observations in the mesosphere with the MU radar by *Nakamura et al.* [1993] are plotted with open circles.

separately for summer months (May–August) and winter months (November, December and March). In the figure there is a tendency that horizontal propagation directions tended toward east and west during summer and winter months, respectively. These results show a fairly good consistency with the results for mesospheric gravity waves by *Nakamura et al.* [1993]. That is, prefered propagation directions by *Nakamura et al.* [1993] were toward northeast and west during May–August and November–December, respectively, although they were rather isotropic during March–April, suggesting horizontal propagation directions of dominant gravity waves are not significantly changed at 60–95 km.

Seasonal variation of propagation directions was attributed to the directional filtering of gravity waves by prevailing zonal winds [*Ebel et al.*, 1987]. In Figure 4.12 we show profiles of mean winds in each observation period. Since duration of each observation was not a multiple of 24 hr, we obtained mean winds by decomposing the wind field into mean winds, semidiurnal and diurnal tides so as to exclude tidal effects.

Mean zonal winds were generally eastward throughout a year at altitude range 80–96 km, while mean meridional winds were generally smaller than the zonal winds. However, Figure 4.12 suggests that mean zonal winds were quite different between summer and winter months below 80 km. That is, a very large wind shear recognized in summer indicates that mean zonal wind was westward below 80 km, while in winter the sense of vertical shear, although not very large in general, was opposite to that in summer, suggesting that mean zonal wind was eastward below 80 km. These features showed a good consistency with the mean wind by the Kyoto meteor wind radar observations in 1983–1986 [*Tsuda et al.*, 1987] and CIRA 1986 model.

Below the meteor observation height a clear seasonal variation of mean zonal winds at 60–80 km were reported by *Nakamura et al.* [1995] using turbulence echo data in 1985–1988 observed with the MU radar as shown in Figure 4.13, where mean zonal winds were ~40 m/s toward west in summer and ~60 m/s toward east in winter at around 70 km, while mean meridional winds were much smaller and around 10 m/s. Directions of these wind velocities shows an opposite sense to those of the dominant gravity waves seen in Figure 4.11. Since these zonal wind velocities were comparable to the observed horizontal phase speeds of the dominant gravity waves, the seasonal variation of propagation directions of these waves seemed to be related to directional filtering caused by the prevailing zonal winds below the height range of meteor observations.

Note that below the mesopause horizontal propagation directions of dominant gravity waves were not necessarily toward west in winter but they were toward north-east during January–February, as revealed by *Nakamura et al.* [1993].

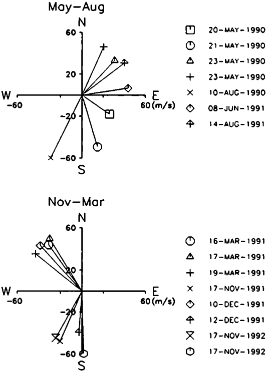

Figure 4.11: The distribution of horizontal propagation directions of dominant gravity waves. Top and bottom panels correspond to summer and winter months. The length of each vector indicates intrinsic horizontal phase speed.

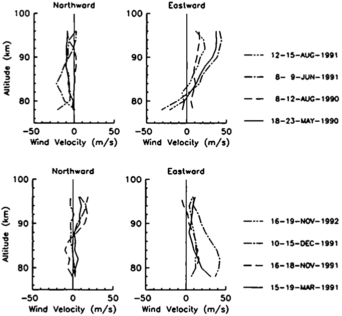

Figure 4.12: Prevailing winds corresponding to observation periods in Figure 4.11. Top and bottom panels correspond to summer and winter months.

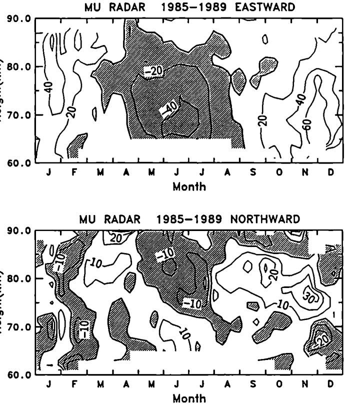

Figure 4.13: The eastward (top) and northward (bottom) components of mean winds observed with the MU radar using turbulence echo in 1985–1989, where shaded areas correspond to westward and southward wind, respectively. [*Nakamura et al.*, 1995]

These results imply the possibility that source regions of gravity waves are not isotropically distributed around Shigaraki [*Nakamura et al.*, 1993].

4.3.2 Simultaneous Observations with the MU Radar and the Sodium Lidar

In this subsection, we present simultaneous observations of mesospheric gravity waves carried out by using the meteor observations with the MU radar in Shigaraki (34.9°N, 136.1°E) and a sodium lidar observations in Hachioji (35.6°N, 139.4°E) [*Namboothiri et al.*, 1994].

As the latest developments, lidars have proved to be quite powerful to measure the mesoscale fluctuations in the middle atmosphere. The temperature fluctuations and the sodium density fluctuations observed through the Rayleigh scatter and resonant backscatter by the Rayleigh lidar and Sodium lidar, respectively are found to be an important tracer of gravity waves. [e.g., *Gardner and Voelz*, 1987; *Hauchecorne et al.*, 1987; *Wilson et al.*, 1991; *Beatty et al.*, 1992; *Collins et al.*, 1994]. Various important features of gravity waves such as individual wave events, seasonal variability, and spectral aspects of total gravity wave field etc have been reported [e.g., *Shibata et al.*, 1986; *Senft and Gardner*, 1991; *She et al.*, 1991; *Hostetler and Gardner*, 1994].

Although there have been a few attempts for the comparison of simultaneous lidar measurements of densities and radar measurements of horizontal winds [e.g., *Ogawa et al.*, 1989; *Franke et al.*, 1990; *Kwon et al.*, 1990], the radar and lidar studies of the gravity waves mainly concentrated on individual stations so far. Simultaneous observations at different locations are very important in order to understand clearly the propagation details such as the horizontal extension [e.g., *Meek et al.*, 1985; *Manson et al.*, 1988]. This will also give some insights to differentiate the various sources of gravity waves between the locations.

To this respect, collaborations between the Radio Atmospheric Science Center (RASC) and Tokyo Metropolitan University (TMU) have arranged and made some simultaneous mesospheric observations using the meteor echo measurements with the MU radar at Shigaraki and the sodium density measurements using the Sodium lidar at Hachioji. These two locations are separated by a horizontal distance of 310 km, which is appropriate as far as the horizontal wavelength of a large scale gravity wave is concerned. The neutral atmospheric density perturbations can be inferred from the Na density measurements and in our study the analysis mainly focuses on the neutral density fluctuations.

Experimental Setup

We first present in Figure 4.14 the locations of the MU radar and the lidar. Note that the baseline of the stations makes an angle of 14.5° with the zonal direction.

The data used are from the 7 hours of observations on the night of December 15–16, 1993. Figure 4.15 shows profiles of the wind components and the temperature perturbation T'/T_0 observed with the MU radar during the period, where time and height resolutions were 1 hour and 1 km, respectively. Note that in the figure the time mean values were removed from each time series, and vertical wavelengths longer than 4 km were extracted from each profile with a low-pass filter. A clear wave induced fluctuation showing a downward phase propagation was recognized, especially for the northward wind component as indicated by a solid line.

The sodium lidar was installed recently and operated at the Tokyo Metropolitan University. The lidar consists of a tunable dye laser pumped by a frequency doubled Nd:YAG laser, receiving telescope, a photomultiplier tube and a computer controlled data acquisition system. The signals from 2000 laser shots are accumulated for each profile. Consequently, one profile is observed once in every 4 minutes with a height resolution of 100 m. The laser shot number is selected to assure an acceptable signal-to-noise ratio for each profile. The details of the system specifications and the method of data analysis can be seen in a report by *Nagasawa and Abo* [1994]. Figure 4.16 shows the Na density values measured on December 15–16, 1993. The profiles are plotted on a linear scale at 8-min intervals and have been low-pass filtered with a cutoff at 1.5 km. The downward movement of the Na density peak seems to be affected by the gravity waves or tides. A detailed description of the figure can be seen later.

The Na density measurements can be effectively used to deduce the atmospheric density perturbations [*Gardner et al.*, 1989; *Beatty et al.*, 1992]. When the wind fluctuations are caused by gravity waves, the relative Na density fluctuations are related to the relative atmospheric density perturbations. The following is a short account on the steps involved in the calculation of atmospheric density perturbations from the sodium density values. First, the sodium density is normalized in the altitude range by the total column density for each profile, here the altitude range considered is 80–105 km. Then the profiles are filtered with a low-pass filter with a cutoff equal to 1.5 km and an average profile for the sodium density is produced from all the profiles. Now the sodium density perturbations can be calculated and the sodium density perturbations are transformed to atmospheric density perturbations. Here it is assumed that the unperturbed Na profile is modeled by a Gaussian distribution, and then the relative Na density fluctuations can be expressed in terms of atmospheric density fluctuations [*Gardner et*

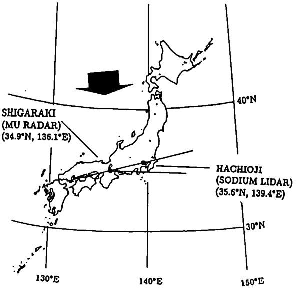

Figure 4.14: Locations of the MU radar and Sodium lidar. The base line and the horizontal make an angle of 14.5°. The big arrow indicates the horizontal propagation direction of the gravity wave, which is 5.45° off vertical to the zonal direction [*Namboothiri et al.*, 1994].

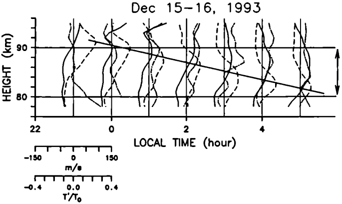

Figure 4.15: Time-height variations of the fluctuating components of the eastward (solid line) and northward (dashed line) wind velocities and the normalized temperature (dot-dash line) observed with the MU radar on December 15-16, 1993. The region 80-90 km is marked to indicate that the study focused on that height range [*Namboothiri et al.*, 1994].

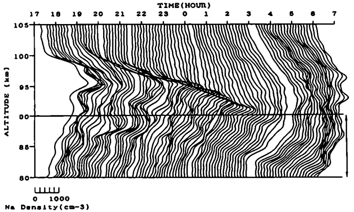

Figure 4.16: Sodium density profiles measured on the night of December 15-16, 1993. The profiles are plotted on a linear scale at about 8 min intervals. The region 80-90 km is marked to indicate that the study focused on that height range [*Namboothiri et al.*, 1994].

al., 1989],

$$r_s(z,t) = -\frac{1}{(\gamma - 1)}[1 - \frac{\gamma H(z - z_0)}{\sigma_0^2}]r_a(z,t) \tag{4.2}$$

$$r_s(z,t) = \rho_s'/\rho_{s0} \tag{4.3}$$

$$r_a(z,t) = \rho_a'/\rho_{a0} \tag{4.4}$$

where γ = ratio of the specific heat (~1.4)
H = atmospheric scale height (~6 km)
z_0 = centroid height of the unperturbed Na layer (~92 km)
σ_0 = rms thickness of the unperturbed Na layer (~4.3 km)
ρ_s'/ρ_{s0} = relative Na density fluctuations
ρ_a'/ρ_{a0} = relative atmospheric density fluctuations

The prime in ρ_s' and ρ_a' denotes the perturbation quantity, while the suffix 0 denotes the associated mean quantity.

Figure 4.15 indicates that the data from the altitude range 80–95 km are usable for the MU radar observations. While, the sodium lidar measurements are available for a height range of 80–105 km as seen in Figure 4.16. Although this is the case, in the present study of the gravity wave induced neutral density perturbations, we concentrated only the altitude region 80–90 km. From Equation 4.2 it can be seen that the altitude dependent scaling factor vanishes near the Na layer peak, z_0, it is not possible to determine the atmospheric density perturbations in the vicinity of z_0 [*Senft and Gardner*, 1991].

Hodograph Analysis of Gravity Waves

We performed a hodograph analysis to extract wave parameters from the data obtained with the MU radar. Before presenting the results of our hodograph analyses, it is appropriate to give a background on the data selected for the detailed analysis. It was our interest to search large scale gravity wave activities and for this we have investigated 5 nights of simultaneous observational data. But unfortunately we could get only one nights (15–16 December, 1993) data with less interference of waves. Hence we considered that data for our detailed analysis. Again in the data considered itself, although we have the lidar data for a period 1700-0600 LT we selected a period from 2200–0500 LT when the overlapping of waves is not significant. From Figure 4.16 it can be seen the dominance of monochromatic waves during the period 2200-0500 LT. Before and after that period smaller scale variations dominated.

In the present analysis, a wave period of 5-20 hr was considered and the data were filtered accordingly. After the mean wind and linear trend were removed from the vertical profile, wave components with a vertical wavelength greater than 7 km were extracted. The hodograph and the height profiles were constructed with one hour interval starting from 2300 LT to 0500 LT. Figure 4.17 shows a typical hodograph and height profile of the gravity wave of our interest. The hodograph shown is for 0200 LT on December 16, 1993. In this example the successive wind velocities in the height region 77–85 km were fitted by an ellipse. We have tried to include all the possible data points especially in the height region 80–90 km, since in the present study we are more interested in that height range. Unfortunately it was rather difficult to conduct a fit with all the desired data points. In the height profiles the solid curve represents the northward component, the dashed curve represents the eastward component and the curve with the solid circles is the temperature perturbations.

As evident from the figure, the wind vector rotated in the clockwise direction with the increase in altitude, indicating positive vertical group velocity. Also it can be seen the dominance of a monochromatic gravity wave and such a wave was observed in all the hodographs except the 0500 LT case. The 0500 LT case is separately discussed below. The horizontal propagation direction was found to be in the north-south direction and this is consistent with all the other hodographs. The exact propagation direction can be determined by checking the phase relations between the horizontal wind components and the temperature perturbations and it was found that the wave propagated from north to south. The arrow in Figure 4.17 represents the direction of propagation of the wave.

Figure 4.18 is the plot for the hodograph and height profile for 0500 LT. The ellipse was fitted with the wind velocities in the height range 82–90 km. The ellipse indicated by a dotted line in Figure 4.18 also shows the horizontal and vertical propagation directions to be identical to that of the 0200 LT case. However, one important feature of the hodograph to be mentioned is the departure of the monochromatic nature of the gravity wave, the structure of the hodograph in Figure 4.18 suggests that there may be a mixing of two gravity waves.

Hodograph analysis seems to have certain inefficiency when there is a mixing of two or more waves. In Figure 4.17 we presented one of the best cases and in Figure 4.18 we showed the worst case that we have obtained. As mentioned above, Figure 4.18 indicates a mixing of two waves and in this situation two ellipses may be fitted to different altitude ranges. However, we took the ellipse fitted for the 82–90 km height range considering a consistency with earlier hodographs.

Table 4.2 illustrates the values of the gravity wave parameters that we have obtained from the hodograph analyses. It can be seen that the wave had an

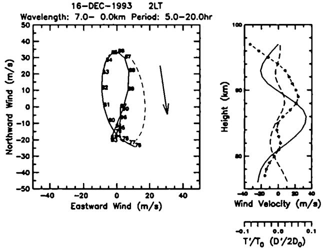

Figure 4.17: The hodograph and height profile obtained at 0200 LT on December 16, 1993. The wave components with periods of 5-20 hr and vertical wavelength longer than 7 km were extracted. The numerals and dashed ellipse in the left panel indicate the height in km and least squares fit to the hodograph, respectively. The arrow indicates the horizontal propagation direction of the gravity wave. In the right panel the fluctuations of northward (solid line), eastward (dashed) and temperature (dashed line with solid circle) are given [*Namboothiri et al.*, 1994].

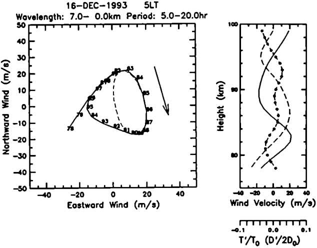

Figure 4.18: Same as Figure 4.17, but for 0500 LT [*Namboothiri et al.*, 1994].

Date	Time (LT)	ω (hr)	λ_z (km)	Azm. (deg)	λ_h (km)	Amp. (m/s)	$\sqrt{\overline{(\rho'/\rho_0)^2}}$
15 Dec. 1993	2300	8.33	13.8	4.18	1380	16.8	0.0254
16 Dec. 1993	0000	10.45	16.5	-6.00	2068	24.0	0.0362
16 Dec. 1993	0100	9.82	18.0	-8.28	2120	26.1	0.0394
16 Dec. 1993	0200	9.21	16.0	-8.41	1767	28.6	0.0432
16 Dec. 1993	0300	8.60	15.9	2.33	1645	28.3	0.0427
16 Dec. 1993	0400	8.43	16.2	-4.00	1639	28.5	0.0430
16 Dec. 1993	0500	8.95	15.3	-16.00	1644	21.0	0.0315
Average		9.11±0.78	15.95±1.17	-5.45±6.4	1751±241	24.75±4.15	0.0373

Table 4.2: Wave parameters obtained from the hodograph analyses of height profiles of wind velocity observed with the MU radar [*Namboothiri et al.*, 1994].

average intrinsic period of about 9 hr and a vertical wavelength of about 16 km. The inferred horizontal wavelength showed a variation between 1380 km and 2120 km with an average value of 1750 km. To compute the horizontal wavelength we assumed the value of the inertial frequency f as 1.33×10^{-5} Hz at the 35° latitude of the MU radar, corresponding to a period of 20.9 hours. The propagation direction was found to be from north to south with an average azimuth of -5°, an arrow in Figure 4.14 shows this direction of propagation. The wave propagated not exactly perpendicular to the baseline of the stations and this will result a timelag in the wave propagation.

It is very important to consider the possible contribution of tidal waves in the profiles we considered here. However, our analysis indicated that there was no significant contribution of 12 hr tides during the period of observation. A tidal analysis was done with 4 days of the MU radar data of that campaign, that is, December 13-16, 1993, including the period of observation considered in the present study, and found that the average amplitude of semidiurnal tides was ~5 m/s in the 80-90 km region. Also climatological results [*Tsuda et al.*, 1988] showed that the amplitude of semidiurnal tides in Kyoto (Shigaraki) are generally less than 5 m/s during December in this altitudes. The effect of diurnal tides is believed to be smaller considering the intrinsic wave period of 9 hr.

Comparison Between the MU Radar and the Lidar

Our major interest here is to calculate the wave induced neutral density perturbations from the gravity wave parameters obtained using the MU radar data, and compare them with those obtained with the sodium lidar observations. The derivation of the density perturbation was based upon the gravity wave dispersion and polarization relations. By applying the Boussinesq approximation, $\rho_a'/\rho_{a0} = -T'/T_0$, the density perturbation can be expressed using Eq. 1.5 as

$$\frac{\rho_a'}{\rho_{a0}} = i\frac{N}{g}u' \tag{4.5}$$

Using Eq. 4.5, the atmospheric density perturbations were calculated for the MU radar observations. A vertical wavelength of 16 km (average λ_z) was considered and in order to add the 90° phase shift, the profiles were height adjusted with 4 km. Here we assumed that a sinusoidal variation was dominant and accordingly the MU radar profiles were reconstructed. Figure 4.19 is a composite picture of the density perturbations obtained for the MU radar and the lidar observations. In the figure the continuous curve indicates the MU radar observations and the dashed curve represents the lidar measurements. Since the horizontal propagation of the wave was in the north-south direction, the values of the northward wind velocity were taken to determine the density perturbations for the MU radar profiles. The profiles shown are for each one hour interval starting from 2300 LT to 0500 LT. It should be mentioned that the comparison was stressed for the height range 80-90 km.

Comparison of the profiles reveals encouraging agreements between the two observations. It can be seen that all the profiles, except for 0500 LT, show good resemblance. The phase pattern observed has considerable similarities. It should be remembered that there was a difference in the height resolution of observation and also a time-series filtering for the lidar data was not being done due to the limited hours of observation per night. Bearing this in mind, a smoothed pattern of the lidar profiles will give even better agreements with the MU radar profiles. It is very important to note that the density perturbation values observed at both the locations were quite similar with a maximum value of about 7%.

Considering the horizontal distance between the sites we should expect a constant phase lag in the wave propagation. Using the wave parameters and the geometry of the two locations we estimated the time lag to be 15 min. We assume that the wave approached Hachioji first and then passed Shigaraki. Any small differences in the phase pattern could be explained under these circumstances. Also one has to consider the horizontal variation in the gravity wave field.

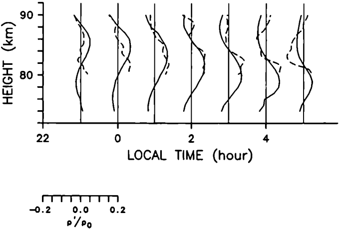

Figure 4.19: Time-height variations of the atmospheric density perturbations obtained from the MU radar and sodium lidar, for December 15-16, 1993. The solid and dashed curves represent the MU radar and lidar observations, respectively [*Namboothiri et al.*, 1994].

The 0500 LT case should be discussed separately, the density perturbations obtained for the lidar measurements near 83 km shows relatively larger (8.8%) perturbations. During morning hours the increase in temperature causes chemical reactions and raises the sodium density. Also the meteoric ablation during dawn will be high and hence results an increase in sodium density.

Another way to check the gravity wave response to the neutral density fluctuations is the variance analysis. Figure 4.20 depicts the time variations of root mean square values of the variance derived for the MU radar and the lidar observations. The density perturbations obtained for the height range 80-90 km were used in this analysis. There is a difference in the number of density values considered for the variance analysis, that is, the sodium lidar which had a height resolution of 100 m and hence a total number of 110 values were considered for the lidar case, while the MU radar had 1 km height resolution and consequently only 11 values were averaged for the radar case. The density variance plotted for the MU radar observations corresponds to the amplitude of the gravity wave induced wind fluctuations. The values of the wave amplitude and the corresponding density variances are also given in the Table 4.2. A remarkable agreement between the two observations is well evident from Figure 4.20. Discarding the 0500 LT case the time variations show identical response for both the observations and it reaffirms that we saw the manifestations of the same gravity waves over Shigaraki and Hachioji.

4.4 Discussion and Conclusions

In this chapter we studied characteristics of gravity waves near the mesopause, taking advantage of the good time-height resolutions of temperature and wind data obtained by meteor echo measurements with the MU radar.

We found that T fluctuations were clearly associated with wave-like structures showing downward phase propagation with periods shorter than the inertial period (21 hour in Shigaraki). We detected an inertial gravity wave with a period of about 12 hr on December 10-11, 1991, which was observed very clearly as to both wind velocity and T'/T_0, and their phase relation was reasonably interpreted assuming the polarization relation predicted by the linear theory of gravity waves.

Kinetic and potential energy densities associated with gravity waves are theoretically expected to be equal when wave period is short enough compared with the inertial period. Observed kinetic and potential energy densities calculated from horizontal wind velocity and temperature fluctuations, respectively, coincided well for periods longer than 2 hr. Both energy density showed considerable variations between the campaigns in period range longer than 12 hr, which might

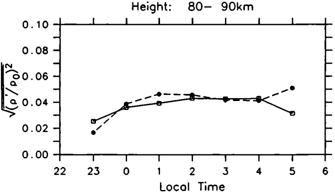

Figure 4.20: Variance of the atmospheric density perturbations calculated for the MU radar (solid line with open squares) and the lidar observations (dashed line with solid circles) [*Namboothiri et al.*, 1994].

be due to large temporal variations of atmospheric tides and inertial gravity waves.

Seasonal variations of horizontal propagation directions of dominant gravity waves were studied using hodographs for 12 observation campaigns from May 1990 to November 1992. Downward phase progression was recognized for most of the waves, indicating the upward energy transportation. Average values of wave periods, vertical and horizontal wavelengths and horizontal phase speeds were 11.3 hr, 13.1 km, 2200 km and 53 m/s, respectively. Note that wave periods and vertical wavelengths seemed to be slightly shifted to shorter values because we selected gravity waves which had clearly shorter periods and wavelengths than diurnal tides to avoid contamination.

Horizontal propagation directions were generally eastward in summer (May-August) and westward in winter (November-December and March). These results showed a good consistency with the results of the turbulence echo observations in the mesosphere with the MU radar by *Nakamura et al.* [1993], suggesting that propagation directions of dominant gravity waves do not significantly change in altitude range from 60 to 95 km. These propagation directions seem to be related to the directional filtering by mean zonal wind below the height region of the present study. Note that propagation directions were not necessarily toward west in winter except for November and December in the mesosphere as reported by *Nakamura et al.*, 1993, implying that the source regions of gravity waves are not uniformly distributed around Shigaraki.

Comparison observations of mesospheric gravity waves were also conducted by means of the MU radar in Shigaraki (34.9°N, 136.1°E) and the sodium lidar in Hachioji (35.6°N, 139.4°E). We used 7 hours of the data collected simultaneously on the night of December 15–16, 1993. The dominant gravity wave and its characteristics were delineated by using a hodograph analysis, which determined that the wave propagated with an average vertical wavelength of 16 km, intrinsic period of 9 hr and horizontal wavelength of 1750 km. We further detected that the gravity wave showed upward energy propagation, and that it propagated from north to south.

The study documented the effective use of gravity wave theory to calculate the wave induced atmospheric density perturbations. The density perturbations showed a maximum of 7% at the radar and the lidar locations. The observed similarities are an indication of the same gravity wave influences at the observational sites. The variance analysis conducted for the density perturbations also showed remarkable agreement in time variations and this is an additional point that support the view that the radar and lidar saw the same gravity wave.

Finally, in this chapter, we showed that short period temperature and wind velocity fluctuations obtained by meteor echo measurements with the MU radar were preferably interpreted by using a linear theory of gravity waves. Then, they were utilized to delineate a seasonal characteristics of dominant gravity waves. Furthermore, a gravity wave with a large horizontal extent was observed through simultaneous observations at two observation sites, then parameters of gravity waves obtained at one observatory were proved to be valid. Through these studies simultaneous observations of temperature and wind velocity fluctuations by meteor echo measurements with the MU radar were shown to be very effective for study of gravity waves.

Chapter 5

Observations of Global Structure of Planetary Waves

Cooperative radar observations revealed characteristics of planetary waves with periods ranging from one day to a few weeks in the upper mesosphere and lower thermosphere [*Salby*, 1980; *Ito et al.*, 1984; *Vincent et al.*, 1984; *Manson et al.*, 1987]. Various observations and theoretical studies pointed out that planetary waves affect mean winds and other waves through nonlinear interactions [e.g., *Plumb at al.*, 1987; *Rüster*, 1994; *Teitelbaum and Vial*, 1991]. In the stratosphere studies using satellite data clarified horizontal and vertical structure of planetary waves and identified various normal mode Rossby waves [e.g., *Hirota and Hirooka*, 1984]. However, global structure of most of long period oscillations near the mesopause was not fully identified yet. In this chapter we study characteristics of long-period wind fluctuations around the mesopause using data obtained at radar stations spaced in latitude and longitude.

5.1 Long-period Waves in Middle Latitudes

Tsuda et al. [1988a] reported long-period oscillations in Shigaraki (35°N, 136°E) using the meteor radar observations conducted from May 1983 to March 1986. They showed oscillations with periods from 1.4 days to 20 days. However, global structure of these waves was not delineated yet except for a wave with a period of about two day (here after referred to as 'two-day wave'). In this section we study global structure of planetary waves by additionally using two data sets from Adelaide MF radar (35°S, 138°E) and Saskatoon MF radar (52°N, 107°W) during May 1983–March 1986. Since there were small number of meteor echoes in evening hours, meteor radar observations were not suitable to delineate continuous time series of wind velocity with a height resolution of 2-4 km. We obtained single bihourly time series by accumulating all the meteor echoes, assuming that wind fields were invariant throughout the observation height range because most of planetary waves are thought to be external modes, and thus have fairly long vertical wavelength.

The center height of meteor echo distribution was around 95 km with a standard deviation of several km [*Yamamoto et al.*, 1986]. For the MF radar observations bihourly time series at five heights, 82, 86, 90, 94 and 98 km, were used.

We calculated mean frequency spectra by Fourier transforming auto correlation functions on the time series from May 1983 to March 1986 with a maximum lag of 30 days, as shown in Figure 5.1 (a), where maximum and minimum wave periods are 60 and 0.8 days, respectively. Conspicuous peak at wave period of 1 day is diurnal tide. For wave periods longer than 1 day, two-day waves showed clear peaks at all the stations, being the largest at Adelaide. Peaks were also seen at periods of 3-5 days and 5–10 days. For longer wave periods spectral density showed fairly monotonous increase with periods, especially in the zonal component.

Furthermore, latitudinal and hemispheric differences are recognized as well. That is, wave activity was the largest in Adelaide and the smallest in Shigaraki in general throughout the frequency range. For wave periods longer than 20 days Saskatoon and Adelaide showed similar spectral densities. Note that a part of small wave energy in Shigaraki might be due to the fact that we accumulated all the data into single time series without considering height variations.

Spectra are plotted in an area preserving form in Figure 5.1 (b). For wave periods longer than 1 day two-day waves made the largest contributions, especially in Adelaide.

Dynamic frequency spectra were calculated by Fourier transforming auto and cross correlation functions on 90 day time series with a maximum lag of 30 days (frequency resolution, 0.0167/day), where the data window of 90 days was stepped forward every 5 days. Five auto spectra of Adelaide and Saskatoon corresponding to the five height layers were averaged to reduce estimation error. Resultant dynamic auto spectra are shown in Figures 5.2 and 5.3 for zonal and meridional wind velocities, respectively. Note that these spectra were smoothed using a spectral window of a raised cosine with a width proportional to frequency. In the figure various oscillations can be seen, among which two-day waves showed remarkable activity, appearing regularly in summer hemisphere at all the observation sites especially in the meridional component. It is noteworthy that in Saskatoon waves with periods longer than 5 days showed clear enhancement in winter months.

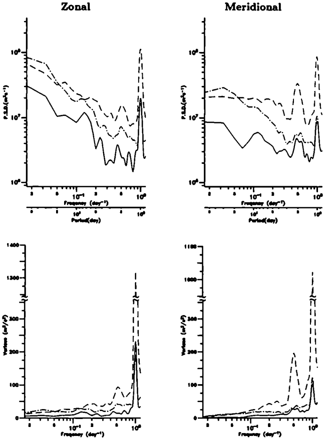

Figure 5.1: Frequency spectra (top) and area preserving spectra (bottom) of zonal wind (left) and meridional wind velocities (right) calculated using data from May 1983 to March 1986. Results for Shigaraki (solid), Adelaide (dashed) and Saskatoon (dot-dashed) are shown.

These may be due to normal mode Rossby waves, which were reported to show large amplitudes in winter months from theoretical and observational studies in the stratosphere [*Salby*, 1981b; *Hirooka and Hirota*, 1985; *Hirooka and Hirota*, 1989]. In the other two stations such features were not as clear as in Saskatoon, possibly due to latitudinal difference.

Cross spectra between Shigaraki and Adelaide/Saskatoon were obtained by averaging five cross spectra between the one layer data in Shigaraki and the five height data in Adelaide/Saskatoon. Further, phase and coherence were calculated from the auto and cross spectra, where estimation error of phase value was about 45°. We considered that planetary waves were simultaneously detected at two radar sites when the following conditions were satisfied.

1. Clear peaks in auto and cross spectra were recognized at the same wave frequency.
2. Fairly invariable phase values were recognized around the corresponding wave frequency.
3. Clear peaks were recognized in coherence at the corresponding wave frequencies.

According to these criteria we extracted 6 waves between Shigaraki and Adelaide, and 14 waves between Shigaraki and Saskatoon. Unfortunately, none of these waves satisfied the criteria for both zonal and meridional components at the same time. Wave periods and observed dates are summarized in Figure 5.4. Obtained wave periods ranged from 1.1 to 10.0 days. Many of these events corresponded to waves found by *Tsuda et al.* [1988a], especially for period ranges longer than 5days and shorter than 2 days. We could not detect waves with periods from 3 to 4 days, although waves in this period range sometimes enhanced independently in Shigaraki [*Tsuda et al.*, 1988a], Adelaide and Saskatoon as seen in Figures 5.2 and 5.3.

It is noteworthy that we detected more cases for the comparison between Shigaraki and Saskatoon than Shigaraki and Adelaide. A number of radar and satellite observations and theoretical studies have indicated that amplitudes of planetary waves show a significant seasonal variation with peaks in winter or summer hemisphere depending on wave modes, thus planetary waves tend to be observed only in single hemisphere [e.g., *Hirota and Hirooka*, 1984; *Hirooka and Hirota*, 1985; *Rodgers and Prata*, 1981; *Salby*, 1981b]. Considering that Shigaraki and Saskatoon are in the northern hemisphere and Adelaide in the southern hemisphere, the difference in detected number of waves seemed to reflect the seasonal dependence of planetary wave activity.

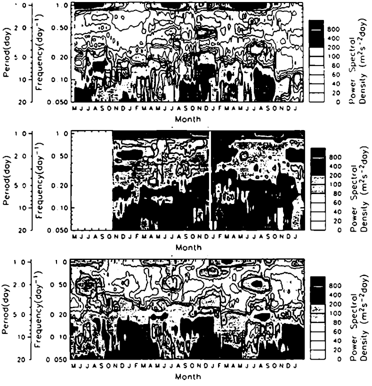

Figure 5.2: Dynamic power spectra of zonal wind velocity in Shigaraki (top), Adelaide (middle) and Saskatoon (bottom) from May 1983 to February 1986. Spectra were analyzed by Fourier transforming an auto-correlation function on a 90 day data series, with a maximum lag of 30 days, where the data window was sled every 5 days.

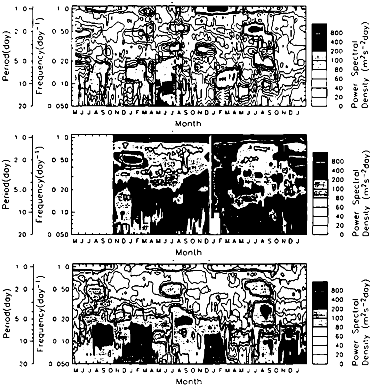

Figure 5.3: Same as Figure 5.2 except for the meridional component.

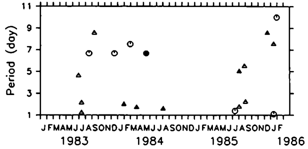

Figure 5.4: Long-period waves observed simultaneously in Shigaraki and Adelaide (closed symbols) and in Shigaraki and Saskatoon (open symbols). Zonal and meridional components are presented with circles and triangles, respectively.

We now attempt to identify global structure of these waves by comparing phases of cross spectra with theoretical prediction. Table 5.1 shows theoretical prediction for phase difference among Shigaraki, Adelaide and Saskatoon for principal normal mode Rossby waves in no background mean wind condition, where 'n' and 'm' indicate zonal wavenumber and meridional index. Waves with odd and even numbers of 'n-m' have symmetric and antisymmetric global structure about the equator, respectively [*Salby*, 1981b]. Since each normal mode Rossby wave is known to appear with a fairly fixed wave period [e.g., ***Hirota and Hirooka***, 1984], we categorized observed waves into 5 groups according to their periods. That is, we selected 1.1-1.4days, 1.6-1.8days, 2.1-2.2days, 4.6-5.5days and 6.7-10days, which correspond to periods range of (1, 0), (2, 0), (3, 0), (1, 1) and (1, 2) (or (2, 2)) mode Rossby waves, respectively.

Figures 5.5 and 5.6 show vector plots of phase values for the first 4 wave periods, where observed phase values are plotted with solid lines, referring to Shigaraki. Clockwise rotation indicates that phase of Adelaide/Saskatoon led Shigaraki. Length of each vector presents wave variances integrated in a frequency band centered at wave period with a half width of 0.0167/day. In the figures theoretical prediction at Adelaide/Saskatoon is also plotted with dashed lines, where length of each vector has no meaning. In Figures 5.5 and 5.6 several waves showed fairly good consistency with the theoretical prediction except for the

Mode	Saskatoon leads Shigaraki (degree)		Adelaide leads Shigaraki (degree)	
(n, n-m) (Period)	E	N	E	N
(1,0) (1.24-1.29d)	117	117	182	2
(1,1) (4.4–5.7d)	117	117	2	182
(1,2) (8.3–10.6d)	117	117	182	2
(1,3) (11.1–20.0d)	117	117	2	182
(2,0) (1.6–1.9d)	243	243	184	4
(2,1) (3.8–4.8d)	243	243	4	184
(2,2) (7.3d)	243	243	184	4
(3,0) (2.1–2.5d)	351	351	186	6

Table 5.1: Theoretical phase relation between 3 observatories for normal mode planetary waves in no background mean wind condition. 'E' and 'N' indicate eastward and northward components, respectively. 'n' and 'm' present zonal wavenumber and meridional index. Theoretically predicted period ranges are taken from *Salby* [1981b].

period range of 1.6–1.8 days. Some discrepancy between observations and theory seems to the effect of background mean wind. That is, theoretical study by *Salby* [1981b] indicated that global structure of a planetary wave is significantly affected by the mean wind. The discrepancy might also be attributed to estimation error caused by fairly small wave variances ranging from 2 to 10 m^2/s^2 as seen in Figures 5.5 and 5.6, that is, from 1 to 3 m/s in terms of wave amplitude, except for two-day wave event in January 1984 when a significant wave variance of 50.8 m^2/s^2 was detected in Adelaide. This two-day wave was found to have antisymmetric structure about the equator, and was interpreted as (3, 0) mode by *Tsuda et al.* [1988a]. The antisymmetric feature was reconfirmed in Figure 5.6 (a).

Figure 5.7 shows results for the period range of 5–10days. Although some cases revealed phase values very similar to the theoretical predictions of (1, 2) and (2, 2) modes, observed phase values were rather random and did not show a clear tendency. Since this period range of 5–10 days is not necessarily dominated by a single wave activity [e.g., *Hirooka and Hirota*, 1985], superposition of waves may be possible. Further, global structure of waves with longer periods are more sensitive to background wind motion due to their smaller horizontal phase speed. Therefore, it is not easy to identify the global structure of planetary waves with fairly long periods.

In this section we studied behavior of planetary waves around the mesopause in middle latitude using data obtained from cooperative radar observations. We detected waves which implied the existence of (1, 0), (2, 0), (3, 0), (1, 1), (1, 2) and (2, 2) normal mode Rossby waves. However, wave amplitudes were not very significant except for two-day waves which appeared with quite a large amplitude in summer hemisphere. We investigate global structure of two-day wave in more detail using simultaneous wind and temperature observations conducted at Shigaraki and Jakarta in Section 5.3.

5.2 Waves in Equatorial Region

The equatorial middle atmosphere is characterized by mean circulation which are not annual in character unlike extratropical latitudes, moreover, it contains unique waves such as equatorial Kelvin waves and Rossby-gravity waves [e.g., *Andrews et al.*, 1987]. In the lower stratosphere below about 35 km the zonal wind velocity is characterized by a quasi-biennial oscillation (QBO). While, in the upper stratosphere and mesosphere a semiannual oscillation (SAO) becomes dominant, which was first discovered by *Reed* [1965] using radiosonde and rocketsonde measurements. *Hirota* [1978] and *Hamilton* [1982] showed that SAO consists of two separate oscillations centered at the stratopause (SSAO) and the

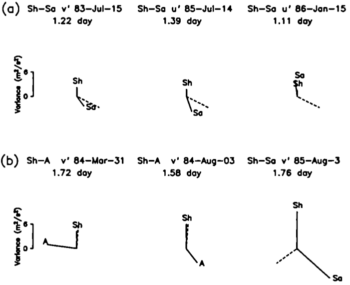

Figure 5.5: Vector plots of phase values of cross spectra between Shigaraki and Adelaide (Sh-A) and Shigaraki and Saskatoon (Sh-Sa), where clockwise rotation indicates leading phase. 'Sh', 'A' and 'Sa' at the tip of each vector stand for Shigaraki, Adelaide and Saskatoon, respectively. Length of each vector presents wave variance integrated in a frequency band centered at wave frequency with a half width of 0.0167/day. Results of period ranges of (a) 1.1-1.4 days and (b) 1.6-1.8 days are shown. Dashed lines indicate theoretical phase values at Adelaide and Saskatoon calculated regarding Shigaraki as a reference, where assumed wave modes were (1, 0) and (2, 0) for (a) and (b), respectively.

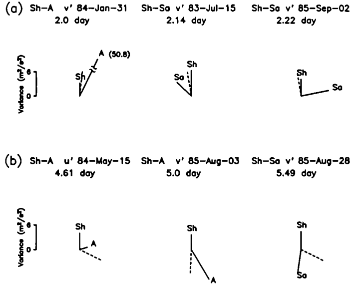

Figure 5.6: Same as Figure 5.5 except for results of period ranges of (a) 2.0–2.2 days and (b) 4.6–5.5 days. Dashed lines indicate theoretical phase values at Adelaide and Saskatoon obtained by assuming (3, 0) and (1, 1) modes for (a) and (b), respectively.

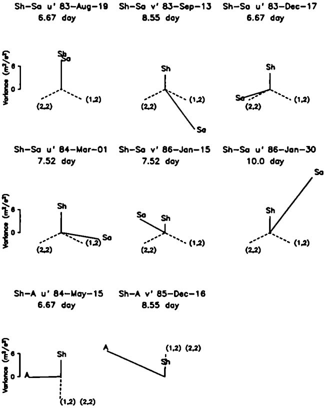

Figure 5.7: Same as Figure 5.5 except for period range of 6.6-10 days. Theoretical phase values are plotted for (1, 2) and (2, 2) modes.

mesopause (MSAO) with an amplitude minimum near 65 km, and an approximate out-of phase relationship between the mesopause and stratosphere maxima. As suggested by the generation of eastward winds at the equator and hence the production of angular momentum per unit mass greater than that of the earth, these oscillation are thought to be driven by the momentum deposition associated with breaking or dissipating Kelvin waves, Rossby-gravity waves, atmospheric tide, and gravity waves [e.g., *Lindzen and Holton*, 1968; *Hirota*, 1978; *Dunkerton*, 1982, *Andrews et al.*, 1987].

However, the study of the equatorial atmosphere mainly relied on balloons and rocket sounding at limited locations with supplement of satellite measurements below 70 km so far, thus the dynamics around the mesopause has not been well understood. Recent MF radar observations in Christmas Island (6°S, 107°W) at 65–100 km revealed MSAO as well as Kelvin-like waves [*Vincent and Lesicar*, 1991; *Vincent*, 1993a; 1993b]. Moreover, we have obtained mesospheric wind fields with meteor radar observations near Jakarta. In this section we investigate mean winds and planetary waves in the equatorial mesosphere using simultaneous observations by Jakarta meteor wind radar and Christmas Island MF radar.

Annual Mean Frequency Spectra in 1993

Figure 5.8 shows frequency spectra of wind velocity at 90 km observed with the meteor radar in Jakarta and the MF radar in Christmas Island in 1993. The range of wave periods is from 6 hr to 60 days, where spectra were calculated by Fourier transforming an auto-correlation function on 365 day time series with a maximum lag of 30 days. Since original frequency spectra had closely spaced data points at higher frequencies, these spectra were smoothed using a spectral window of a raised cosine with a width proportional to frequency.

Figure 5.8 (a) indicates existence of various waves over a wide frequency range. Clear peaks were recognized for tidal components at 24 hr, 12 hr and 8 hr as well. Spectral density of diurnal and semidiurnal tides was larger for meridional component than zonal component by a factor of about 2. Note that there also existed 16 hr oscillation. Spectral density at periods shorter than 1 day, other than the tidal components, decreased with frequency with a logarithmic slope of about −2 for the meridional component, suggesting that these components were due to superposition of gravity waves. While, spectral density for the zonal component revealed a much more gradual decrease with frequency. Note that a noise floor at periods shorter than about 12 hr was recognized for the zonal component. Because the observations was done with antennas steered to north-south direction, meteor arrival directions were concentrated within about 30° from north (or south), resulting in better estimation for the meridional wind velocity than the zonal one.

Remarkable peaks were seen near 2 days in the meridional component and 3–4 days and 6–7 days in the zonal component. The two-day wave seemed to be (3, 0) mode of mixed-Rossby-gravity wave, which was enhanced at low and middle latitude in summer hemisphere [e.g., *Vincent*, 1984, *Tsuda et al.*, 1988a]. At periods longer than 10 days the zonal component had larger energy than the meridional component. *Eckermann and Vincent* [1993] reported similar variations in the zonal component from the MF radar observations in Christmas Island, and interpreted them as an effect of time-varying mean wind rather than long period Kelvin waves.

Frequency spectra in Figure 5.8 at the two locations revealed a similar feature with peaks at tidal components, near two days, 3–4 days and 6–7 days. However, there are some marked differences as well. It is noteworthy that spectral density was generally greater in Jakarta at periods shorter than 4 days for both zonal and meridional components by a factor of 1.5–2.5. Part of this discrepancy may be explained by larger wave energy generated by the active cloud convection over a maritime continent around Indonesia [*Andrews et al.*, 1987]. For tidal components the difference could be due to latitudinal difference of the two stations. For the two-day wave spectral density for the meridional component was almost the same at the two sites, but largely different for the zonal component. Considering that Christmas Island is closer to the equator, this difference might reflect the meridional structure of (3, 0) mode, which is expected to be antisymmetric against the equator [*Salby*, 1981a]. The behavior of this wave is investigated in more detail in the next section.

Spectral peaks at 3–4 days and 6–7 days in the zonal component were clearly seen at both sites. *Vincent and Lesicar* [1991] and *Vincent* [1993a; 1993b] also reported prominent wave activity at 3–10 day wave period from observations in Christmas Island, which appeared only in zonal component with a seasonal variation, showing the strongest activity in January–March and July–September. They interpreted these waves as equatorial Kelvin waves, similar to those identified by *Salby et al.* [1984] in the stratosphere by satellite temperature observations. However, their global structure have not been identified yet because of a lack of observations in equatorial mesopause region. Fortunately we detected conspicuous events of these waves simultaneously in Jakarta and Christmas Island in July–September 1993.

In the followings we first investigate the characteristics of mean winds comparing the results between Jakarta and Christmas Island, then we attempt to identify a global structure of the waves at periods of 3–4 days and 6–7 days.

Mean Winds

Figure 5.9 shows prevailing zonal winds observed in Jakarta and Christmas

(a) Jakarta

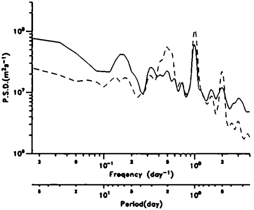

(b) Christmas Island

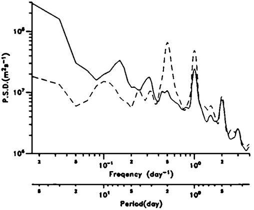

Figure 5.8: Frequency spectra of zonal (solid) and meridional (dashed) wind velocity at 90 km from January 1–December 31, 1993. Results in (a) Jakarta and (b) Christmas Island are shown.

Island from November 1992 to August 1994 after low pass filtering with a cutoff period at 30 days. Since it was sometimes difficult to obtain wind values in the evening due to relatively low meteor echo rate for the meteor observations in Jakarta, simple average of observed winds would yield a significant offset due to tidal component. Therefore, we calculated a mean daily variation of wind velocity by superimposing 10 days of data into local time to get sufficient number of meteor echoes even in the evening hours, then we estimated mean winds by sliding the 10 days window every one day, which was a similar procedure adopted by *Tsuda et al.* [1987].

In Figure 5.9 semi-annual oscillation (SAO) with westward maxima at equinoxes was clearly seen at the both sites throughout the observed height region. In 1993 the westward peak in the vernal equinox (March) was larger, being generally consistent with earlier rocket observations [eg., *Hirota*, 1978]. It is notable that significant year to year variations were also found in Jakarta. That is, wind velocity at the vernal equinox in 1993 showed a peak value of as large as 70 m/s toward west at 80-82 km, while that in 1994 reached only about 20 m/s at 76 km, being smaller than a third of the peak value in 1993. Moreover, wind velocity at the vernal equinox in 1994 was almost 0 m/s or even eastward above 86 km. Considerable year to year variations of MSAO have been reported [*Vincent*, 1993a; 1993b; *Palo and Avery*, 1993], but the difference between 1993 and 1994 was strikingly larger than that reported so far.

We now compare the mean zonal winds between the two radar sites. General features were quite similar, that is, SAO was dominant at the both sites and most of minor westward and eastward perturbations also coincided with each other. Instantaneous peak westward velocities at the vernal equinox were as large as 70 and 80 m/s at 82 km in Jakarta and at 86 km in Christmas Island, respectively, which were observed almost at the same time at the beginning of April 1993. After the maximum westward velocities were recognized, they were followed by a rapid change to eastward wind. This feature was also reported from observations in 1990-1992 in Christmas Island [*Vincent*, 1993a; 1993b]. It is interesting that phase of MSAO often showed downward phase propagation, analogous to the structure of QBO.

There were considerable difference between the two sites, however, especially around the vernal equinox when large westward wind velocity was observed. Figure 5.10 shows 10 day mean height profiles of zonal mean wind velocity centered on April 5, 1993. Above the peak heights westward wind showed rather gradual decrease with height in Christmas Island, maintaining more than 50 m/s even at 98 km. In Jakarta, however, it showed more rapid decrease and reached nearly 0 m/s at 98 km. While below the peak heights, quite a large wind shear, about

Mean Zonal Wind

Jakarta

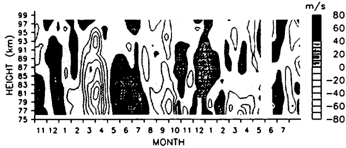

Christmas Island

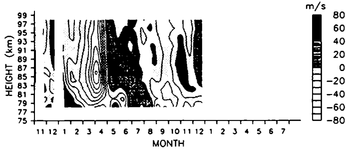

Figure 5.9: Mean zonal winds at Jakarta (top) and Christmas Island (bottom) from November 1992 to August 1993. Periods longer than 30 days have been extracted using a low-pass filter.

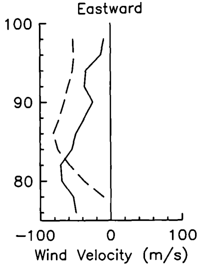

Figure 5.10: Profile of 10 day mean zonal wind velocity centered on April 5, 1993 in Jakarta (solid line) and Christmas Island (dashed line).

8 m/s/km, was observed in Christmas Island and westward velocity was smaller than 10 m/s at 78 km. In Jakarta, however, wind shear was not so large, and westward flow was still about 50 m/s at 76 km.

Earlier observations have pointed out the existence of large longitudinal and latitudinal variations of SAO [*Reddy and Reddi* [1986]]. Asymmetry of SAO about the equator has been also revealed [e.g., *Hirota*, 1980]. Recent satellite (Upper Atmosphere Research Satellite, UARS) observations of the zonal mean zonal wind showed the maximum at 80 km in the vernal equinox of 1993 occured at about 5°S [*Lieberman et al.*, 1993], being qualitatively consistent with the present results.

Next we investigate mean meridional winds in Jakarta and Christmas Island (Figure 5.11). Meridional winds were generally much weaker than the zonal winds, and were characterized by an annual oscillation, flowing from summer to winter hemispheres. We performed a harmonic analysis and found that amplitudes of annual oscillation in 1993 were about 5 m/s at the both stations throughout the observed altitude range. Annual mean northward wind in 1993 were fairly small, ranging -2-0 m/s and 0-3 m/s in Jakarta and Christmas Island, respectively.

However, we found a large difference between the two sites as well. Figure 5.12 presents time series of meridional winds every 2km altitude, where fluctuating components with periods longer than 30 days were extracted. During February-July 1993 meridional wind velocity above 88 km showed oscillating variations which was almost anti-phase between the radar sites. Particularly, during March-April 1993, when a large westward wind velocity was observed, the meridional winds were southward and northward with amplitudes of 10 m/s at Jakarta and Christmas Island, respectively.

Some theoretical and observational works pointed out the latitudinal difference of mean meridional wind near equatorial mesopause. *Miyahara et al.* [1991] showed using numerical model that dissipating diurnal tides and gravity waves could generate cellular structure in the meridional circulation. *Lieberman et al.* [1993] reported using UARS observations that during February-June 1993 at 80 km the flow from summer to winter hemisphere was interrupted at low latitudes by cellular motion in the opposite sense. Further, oscillating feature in Figure 5.12 might be related to long period wave motions.

Kelvin Waves

We now focus on the behavior of waves with periods of 3-4 days and 6-7 days seen in the annual mean frequency spectra for the zonal component shown in Figure 5.8. These waves were often observed in Christmas Island, which are thought to be responsible for eastward acceleration of SAO [*Vincent and Lesicar*, 1991; *Vincent*, 1993a; 1993b], although eastward propagating gravity waves are also required to account for all the eastward acceleration [*R. A. Vincent*, 1994, private communication].

We calculated moving power spectra by Fourier transforming an auto correlation function on a 40 day data series of zonal wind with a maximum lag of 20 days, where the data window was sled forward every 5 days. Frequency resolution is 0.025 /day. We obtained spectra at altitudes from 80 to 98 km every 4 km, then we averaged 5 spectra as in Figure 5.13. In Jakarta conspicuous wave activity was seen during July-September, 1993 at around 0.325/day (3.1 day) and 0.150/day (6.7 day). It is noteworthy that corresponding clear peaks were also observed in Christmas Island, indicating that these waves were of planetary scale. Other peaks were also recognized during January-April, 1993 in Jakarta, and in December 1992 in Christmas Island. However, these waves were

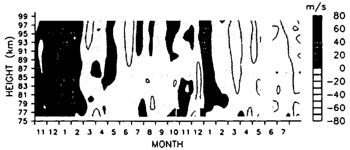

Mean Meridional Wind

Jakarta

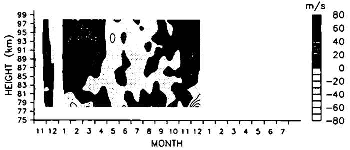

Christmas Island

Figure 5.11: Same as 5.9 except for the meridional component.

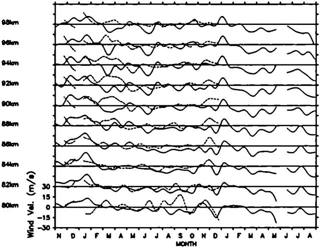

Figure 5.12: Time series of prevailing meridional winds at Jakarta (solid line) and Christmas Island (dashed line) observed in November 1992–August 1994. Periods longer than 30 days have been extracted using a low-pass filter.

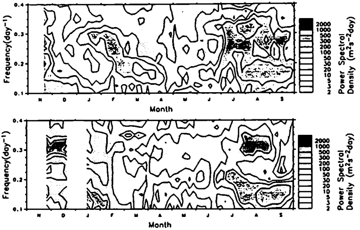

Figure 5.13: Dynamic power spectra for zonal winds at Jakarta (top) and Christmas Island (bottom) from November 1992 to September 1993. Frequency range from 0.1 to 0.4 /day, corresponding period range from 10 to 2.5 day, is plotted.

not simultaneously observed at the two stations. This fact might be qualitatively explained as the effect of zonal mean wind below the observation height. That is, if source region of these waves was limited in a fairly narrow longitudinal area, and horizontal propagation directions of these waves were opposite to prevailing zonal wind, their vertical phase velocities would increase, therefore, these waves could quickly propagate upward and be observed only in fairly limited longitudinal range. For further discussion it is necessary to know their horizontal phase velocities by identifying their zonal wavenumber, their source region and also the mean zonal wind below the present observation height. In the followings we focus on the simultaneously observed waves in Jakarta and Christmas Island during July–September, 1993.

Figure 5.14 shows band-passed time-height section of eastward wind velocity with cutoff periods at 3 and 4 days using data from July 10 to August 18, 1993. Similar downward phase propagation was seen at the both sites with a fairly long vertical wavelength above 85 km altitude. In Christmas Island phase value below 84 km did not show a smooth propagation from the higher altitude unlike in Jakarta, probably due to smaller amplitude in the lower altitudes in Christmas Island. Wave amplitudes were maximized at the end of July 1993 simultaneously at the two stations, reaching a peak value of about 20 m/s. Note that in Jakarta some enhancement was also recognized in meridional component in this period range, although correlation with the zonal component was not very good, suggesting that the enhancement for the meridional component was due to a wave activity different from that seen in the zonal component. While, in Christmas Island no enhancement was observed for the meridional component.

Figure 5.15 shows time-height sections of zonal wind after extracting components of 6–7 day perturbations using data from August 21 to September 30, 1993. Similar wave pattern was seen at the both sites with a peak amplitude of about 15 m/s and a vertical wavelength longer than 60 km. However, at the first stage of this event the wavelength was somewhat longer in Jakarta than Christmas Island as seen in Figure 5.15. During this period no corresponding structure was recognized in the meridional component at the both sites.

We calculated cross spectra by Fourier transforming cross correlation functions obtained using 40 days of wind velocity data centered at July 29, 1993 and September 7, 1993, around which the maximum wave activities were seen for 3–4 and 6–7 day waves, respectively. Dominant wave periods were determined to be 3.1 days (0.325/day) and 6.7 days (0.15/day) from Figure 5.13. The resultant phase values at altitudes from 82 to 98 km are displayed in Figure 5.16 every 4 km, where positive phase value means that Jakarta led Christmas Island.

For the 3-4 day wave the phase was fairly constant, except for 82 km where the wave amplitude was small in Christmas Island as shown in Figure 5.14. Mean phase value from 86 to 98 km was 104°. Since observed wind velocity variations were concentrated to the zonal component at the both stations located near the equator, we can assume only symmetric modes as candidates. Considering the longitudinal difference of 95° between the two sites, possible zonal wavenumber, s, was $1.1 \pm 3.8n$ with n a natural number, where positive value corresponds to eastward phase propagating mode. Assuming that this was an eastward propagating wave, namely, a Kelvin wave, the smallest s is 1 (the exact estimate is 1.1, n=0). Horizontal phase speed of this wave is estimated to be about 150 m/s, which seems to be fast enough to reach the mesopause region not being trapped by mean zonal wind. While, eastward propagating waves with larger s have much smaller horizontal phase speeds of less than 30 m/s. In equatorial stratosphere a Kelvin wave with a period of 3.5–4 days and a zonal wavenumber 1 has been detected in the stratosphere from satellite observations [*Salby et al.*,

Figure 5.14: Band-passed time-height section of eastward wind velocity with cutoff periods at 3 and 4 days on July 10–August 18, 1993. Results in Jakarta (top) and Christmas Island (bottom) are shown.

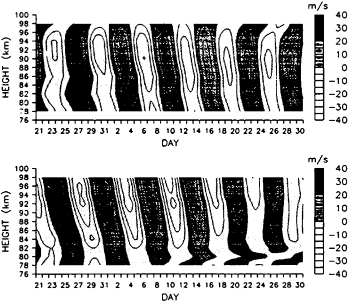

Figure 5.15: Band-passed time-height section of eastward wind velocity with cutoff periods at 6 and 9 days on August 21-September 30, 1993. Results in Jakarta (top) and Christmas Island (bottom) are shown.

1984]. Therefore, provided that our wave was a Kelvin wave, zonal wavenumber 1 is most likely.

On the other hand, assuming that this wave was a westward propagating wave, the smallest $|s|$ is s=-3 (-2.7, n=-1). One of symmetric normal mode Rossby waves with s of -3, i.e., (3, 1) mode, is theoretically expected to have a wave period about 4 days [*Salby*, 1981b]. If wave period of (3, 1) mode becomes 3.1 days, its horizontal phase speed is estimated to be about 50 m/s, which might be enough to reach the mesopause region, although most of the normal mode Rossby waves reported so far had s of 1 or 2 except for (3, 0) mode, which is so called 'two-day wave'.

While, for 6–7 day wave the phase values were quite invariable throughout the observed height range as seen in Figure 5.16, where a mean phase value was 284°, indicating that possible s was 3.0 ± 3.8n. If this wave was a westward propagating wave, value of s should be -1 (0.8, n=-1). However, we can not find a wave with a period around 7 days and s of -1. Although (1, 1) mode, so called 5 day wave, has the nearest period, it was reported to be observed with a period of 5 days in Christmas Island [*Vincent*, 1993b], therefore (1, 1) mode might be discarded for a candidate of the 6–7 day wave. While, assuming that this wave was an eastward propagating wave, a Kelvin wave with a zonal wavenumber 3 (n=0) seems to be most likely. However, its horizontal phase speed was inferred to be only about 20 m/s. Furthermore, observed vertical wavelength was longer than 60 km, being quite longer than a theoretical value which is shorter than 10 km assuming a Kelvin wave to be a two dimensional gravity wave [*Vincent*, 1993b]. At present we can not give relevant explanation to these problems.

Using simultaneous observations at Jakarta and Christmas Island we attempted to identify waves in period range of 3–9 days in the equatorial mesopause region. We found that very clear phase relations existed between the two stations. To fully identify the global structures of these waves at least one more radar station is required. Complementary observations using a satellite like UARS are also desirable.

5.3 Two-day Wave

Two-day wave is one of the the most dominant planetary waves near the mesopause in late summer months [*Vincent*, 1984]. From cooperative radar studies this is thought to be a westward propagating wave with a zonal wavenumber 3 [*Muller and Nelson*, 1978]. Satellite measurements of temperature also showed similar longitudinal structure [*Rodgers and Prata*, 1981], where the amplitude of temperature fluctuation was about 0.5 K near the mesopause in the southern

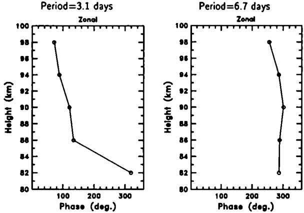

Figure 5.16: Phases of cross spectra between Jakarta and Christmas Island, where Jakarta led Christmas Island by the phase values. Results for 3-4 day wave on July 9-August 17, 1993 (left) and 6-7 day wave on August 18-September 26, 1993 (right) are shown.

hemisphere during January 1976 and 1977.

Although the two-day wave is normally confined to the summer hemisphere, its leakage into the winter hemisphere was sometimes observed [*Craig et al.*, 1983]. *Tsuda et al.* [1988a] further revealed the anti-symmetric structure of the wave from simultaneous observations between Shigaraki (35°N, 136°E) and Adelaide (35°S, 138°E). These observational findings supported the theoretical study by *Salby* [1981a], predicting that the wave is a Rossby-gravity normal mode with a zonal wavenumber of three.

Radar meteor echo observations were recently developed for simultaneous measurements of both wind velocity and temperature fluctuations [*Tsutsumi et al.*, 1994a], which is useful to identify the structure of a two-day wave. In this section we report observations with two radars, i.e., the MU radar at Shigaraki, Japan (35°N, 136°E) and the meteor wind radar, in Jakarta, Indonesia (6°S, 107°E).

Wind velocity and temperature were determined in a time-height bin of 1 hr × 2 km, and 4 hr × 4 km, for the MU radar and Jakarta meteor radar, respectively. However, variations of T'/T_0 for Jakarta meteor radar was delineated only in a single height range centered at 90 km, since the standard deviations of the determinations were rather large at other height ranges due to low meteor echo rates. We first calculated a time mean profile of D_0, which was used to determine D'/D_0 for each meteor echo, then the resultant D'/D_0 was averaged every 4 hours in the height range from 85 to 95 km, and converted to T'/T_0 using Equation 3.8.

In the followings, we describe two events of the two-day wave enhancement in July 1993 and August 1992, where the former is examined by comparing the results between Shigaraki and Jakarta. Seasonal variation of the two-day wave at Jakarta is presented for about one year observations from November 1992 to September 1993.

5.3.1 Coordinate Observations of Two-day Waves

Comparisons between Shigaraki and Jakarta in July 1993

Figure 5.17 shows time series of eastward component u', northward component v' and T'/T_0 at 90 km simultaneously observed in Shigaraki and Jakarta on July 12-19, 1993, where the mean daily variation during this observation period, obtained superimposing raw time series into local time, was removed from each series. A low pass filter with a cutoff period of 8 hr was applied to Figure 5.17 (a) for smoothing.

In Figure 5.17 (a) fairly similar time variations were seen between u', v' and T'/T_0. In wind fields very clear variations with a period of two day were dominantly observed, especially for v' with maxima roughly around 00 LT on odd days. It is notable that two-day variations were also detected in T'/T_0, where shorter periods of variation were also seen, which were thought to be caused by inertial gravity waves. Instantaneous maximum amplitudes of the two-day oscillation were about 40 m/s, 60 m/s and 0.1 for u', v', and T'/T_0, respectively. The amplitude of 0.1 for T'/T_0 corresponded to 18 K provided T_0 was 180 K [CIRA 1986].

In Figure 5.17 (b) two-day variation was clearly observed for v'. It is noteworthy that a remarkable two-day oscillation was also seen for T'/T_0, and showed anti-phase relation with v'. While for u', temporal variations were generally smaller than those of v', and two-day variations were not very clear. Instantaneous maximum amplitudes were about 50 m/s and 0.1 for v' and T'/T_0, respectively.

Similar two-day variations as in Figure 5.17 (a) and (b) were also recognized throughout the height range from 75 to 100 km.

Periodogram Analysis

A periodogram analysis was applied to time series to estimate the dominant wave period, which was determined for both v' and T'/T_0 as 45–47 hrs in Shigaraki and 48–50 hrs in Jakarta, where the wave periods were fairly stable throughout the observed height region. However, the period for u' at Jakarta was not clearly defined, probably due to small amplitude. The slight difference in the periods might be due to Doppler frequency shift caused by different time evolutions of background mean winds in the two sites after the generation of the two-day wave. Some contamination of other periods of waves is also a possible reason for the difference. For comparison of the profiles between Shigaraki and Jakarta, we fixed the wave period to be 48 hrs, and plotted the amplitude and phase profiles in Figure 5.18.

Amplitudes of u' in Shigaraki ranged from 5 to 16 m/s with the maximum value at 86 km. In Jakarta they showed increase with height from 5 to 14 m/s. Amplitudes of v' in Shigaraki were similar to those of u' ranging from 5 to 16 m/s though the peak amplitude was obtained at 90 km, which was higher than that of u' by 4 km. While in Jakarta amplitudes of v' were larger than in Shigaraki throughout the observed altitude range with the maximum value of 22 m/s at 86 km. Note that these amplitudes are smaller than the instantaneous amplitudes seen in Figure 5.17, since we assumed monochromatic sinusoidal variations here.

Amplitude of T'/T_0 in Shigaraki monotonously increased with increasing height ranging from 0.015 to 0.045. In Jakarta amplitude of T'/T_0, determined only at 90 km as mentioned in the previous section, was 0.055, which was about twice larger than in Shigaraki. Corresponding T' was from 2.7 to 8.1 K in Shigaraki and 10.5

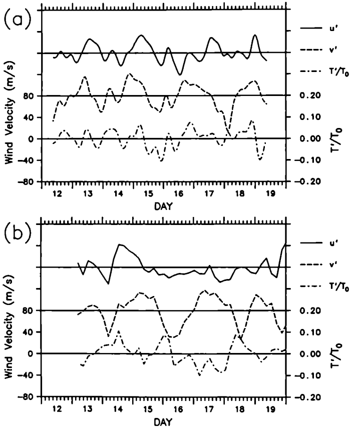

Figure 5.17: Fluctuating components of eastward (solid line) and northward wind velocity (broken line) together with the normalized temperature (chained line) observed on July 12-19, 1993 at 90 km, where mean daily variation during this period was removed from each time series. Results are shown for (a) the MU radar measurements in Shigaraki (35°N, 136°E), and (b) the meteor wind radar in continuous operation near Jakarta, Indonesia (6°S, 107°E).

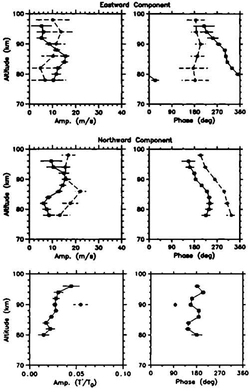

Figure 5.18: Height profiles of amplitudes and phases of u' (top panel), v' (middle panel) and T'/T_0 (bottom panel) of the two-day wave observed on July 12-19, 1993, where phases were defined as the time when fluctuating components had its positive maximum values. The phase value 0 corresponds to 00 UT of even days of July 1993. The wave period was chosen to be 48 hrs. Results at Shigaraki and Jakarta are shown by solid lines with open squares and broken lines with solid circles, respectively. Horizontal bars represent the confidence intervals.

K in Jakarta by assuming T_0 to be 180 K and 190 K [CIRA 1986], respectively. Relative amplitude relation between the observed v' and T'/T_0 showed a fairly reasonable correspondence to that of the numerical study of the two-day wave by *Hagan et al.* [1993] although since global structure of the two-day wave is strongly affected by background wind condition [*Salby*, 1981a; *Rodgers and Prata*, 1981; *Hagan et al.*, 1993] it is not very easy to strictly compare the relative amplitude relation with existing theoretical works.

General structure of the phase profiles for v' was fairly similar between Shigaraki and Jakarta, showing downward phase propagation, that was also recognized for u' except for Jakarta below 86 km, where the corresponding amplitudes were rather small. However, such progression was not clear for T'/T_0.

Here we compare the values of T' of present study with those of satellite study by *Rodgers and Prata* [1981]. The values of T' in the present study showed fairly larger values compared with the satellite observations, where the representative value of T' was about 0.5 K at 85 km in January 1976 and 1977 between 16°S and 32°S. This considerable difference between them might partly due to the difference of the observation time and latitudes. Further, the differences between the observation techniques and analysis methods are also responsible, although they still do not seem to account for all the observed difference. First, the values of T' in the present study were for the conspicuous two-day wave event of only 1 week, and seemed to correspond to the instantaneous peak value, while the satellite study were based on monthly values. Second, the satellite measurements extracted waves assuming both zonal wavenumber and frequency, while the present study does not need to assume wavenumber as a premise, thus, can recognize two-day wave even if longitudinal structure of the wave is not purely sinusoidal but somewhat modified by local background winds. Although some contribution from higher wavenumber modes is possible for the satellite measurements, they are relevant to be excluded because of their very great phase speed [*Rodgers and Prata*, 1981]. Therefore, only pure two-day wave seems to be extracted for the satellite measurements. Third, the height and spatial resolutions of the satellite observations were not as good as the radar observations; for example, the width of the weighting functions at half height was as large as 24 km at the peak height 85 km [*Rodgers and Prata*, 1981]. Since two-day wave generally showed downward phase propagations, an average over such a wide height range will reduce the coherence of received signal, and result in the smaller T'.

One of the major advantages of the present study is that we can observe phase relations between T', u' and v' of waves, which will give us a useful clue to infer the global structure of atmospheric waves. In Shigaraki phase of v' led that of u' by 61° to 158° with the mean value and standard deviation of 89° and 27°, respectively, indicating a clockwise rotation and upward energy transportation in northern hemisphere. On the contrary, the mean phase profiles at Jakarta, averaged over the entire height range, indicated that u' led v' by 82°, with a standard deviation of 48°, being consistent with an anti-clockwise rotation and also the upward energy propagation in southern hemisphere.

The phase of T'/T_0 led that of v' by 94° to -43° in Shigaraki, with the mean value and standard deviation of 31° and 44°, respectively, indicating in-phase relation. On the other hand, the difference in Jakarta was 164° at 90 km, showing anti-phase relation. These phase relations showed consistency with the prediction of the simple theory of Rossby-gravity waves with no background mean wind condition [*Holton*, 1992], although *Salby* [1981a] theoretically predicted that global structure of the two-day wave is significantly modified in the realistic background condition.

We now estimate the zonal structure of the two-day wave from the phase delay between Shigaraki and Jakarta. The phase of v' at Shigaraki preceded Jakarta by the mean value of 80°, with a quite small standard deviation of 9°. While, that for u' was estimated as 98°, with a considerable deviation. Since the difference in longitudes between Shigaraki (136°E) and Jakarta (107°E) is 29°, the phase difference of 80° gives a zonal wavenumber of $2.76 \pm 12.4n$, with n a natural number, where positive value means westward phase propagating mode. Note that we assumed an anti-symmetric mode. Thus, a possible wavenumber seems to be 3, which is quite consistent with the early findings of observational and theoretical studies of the two-day wave.

Observations in August 1992 in Shigaraki

Next we investigate another two-day wave event observed in Shigaraki on August 3–13, 1992, then the meteor radar had not started observations in Jakarta. Figure 5.19 shows height profiles of amplitude and phase for this event, where wave period was determined to be 49 hrs from a periodogram analysis. Amplitudes of v' ranged 16–36 m/s with the maximum at 84 km. The u' amplitudes were generally much smaller than v', showing a slight increase with height from 4 to 10 m/s. While, those for T'/T_0 was 0.02–0.06, showing a similar height variation to that of v'. The corresponding T' was 2.7–8.1 K provided T_0 was 180 K [CIRA 1986].

Phases of u' and v' showed quite clear downward progressions, corresponding to a vertical wavelength of about 80 km. But, they were almost out of phase, although the phase lag is theoretically predicted to be 90° in the northern hemisphere. That is, the phase of v' led that of u' by 160°–204° with the mean and standard deviation of 182° and 13°, respectively.

While phase profile of T'/T_0 showed similar structure to that of v' below

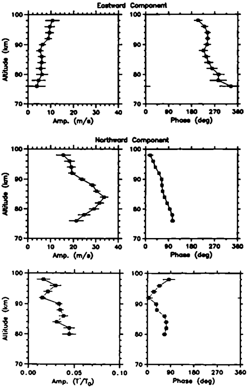

Figure 5.19: Same as Figure 5.18 except for the observations on August 3–13, 1992 with the MU radar at Shigaraki. By using a periodogram, the wave period was best-fitted as 49 hr.

92 km, though the reversed progression with height above that. Phases of v' preceded T'/T_0 by -17° to 46° with the mean and standard deviation of 16° and 18°, respectively, indicating that they were nearly in phase.

Investigating the results in Figures 5.18 and 5.19, the former was fairly consistent with a two-day wave frequently observed with earlier studies. While, it may not be straightforward to understand the case in Figure 5.19 by assuming the manifestation of the same two-day wave. The event in August 1992 was conspicuously observed in the northern hemisphere, and has been studied through global radar network. *Meek et al.* [1994] showed that its horizontal wave number was more likely to be 4 instead of 3. A numerical study also suggested that the period of such a wave with zonal wavenumber 4 can be around two-day in a realistic background condition [private communication, *Hagan*, 1994].

5.3.2 Seasonal Behavior in Equatorial Mesosphere

In this section we investigate the seasonal characteristics of the two-day wave in the equatorial mesopause region using a moving power spectra. Spectra were analyzed by Fourier transforming an auto-correlation function on a 30 day data series of u', v' and also T'/T_0 at 90 km, with a maximum lag of 10 days, where the data window of 30 days was stepped forward every 5 days (Figure 5.20). The mean daily variation was not removed from each time series in the spectral analysis. Resultant frequency resolution is 0.05/day. Note that in Figure 5.20, spectra of $g/N \cdot T'/T_0$, that is, the potential energy, are shown by adopting the values $2\pi/300$ rad s^{-1} and 9.55 m s^{-2} for N and g, respectively.

Diurnal tide was evidently recognized in Figure 5.20 (a) and (b) throughout the year with larger amplitude in v' than u'. Diurnal variations of T'/T_0 were also remarkable as seen in Figure 5.20 (c), which, however, may not be solely interpreted as the effects of propagating tides [e.g., *Tsutsumi et al.*, 1994a].

Here we focus on 2 day oscillation. In Figure 5.20 (a) spectral values for u' were not very significant around 2 day in general. While those of v' in Figure 5.20 (b) exhibited clear enhancement throughout the year. Especially the 2 day oscillation was magnified after solstices, i.e., in January-February 1993 and July-August 1993, coincident with summer months in the southern and northern hemisphere, respectively, where the event was more conspicuous during the former period. Spectral values for T'/T_0 also showed a marked enhancement around 2 day as in Figure 5.20 (c) with a seasonal variation similar to that seen in Figure 5.20 (b). During the end of February to the beginning of March 1993, however, the value of T'/T_0 showed non-monochromatic structure with two peaks near two day, which was not recognized for v'.

In Figure 5.20, periods of two-day wave seem to reveal a remarkable seasonal

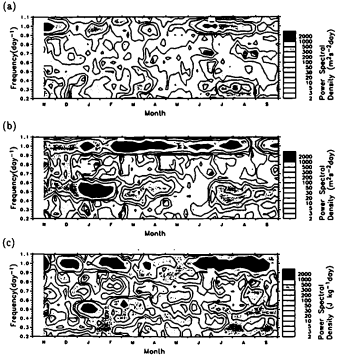

Figure 5.20: Dynamic power spectra of (a) u', (b) v' and (c) $g/N{\cdot}T'/T_0$ observed at 90 km in Jakarta, where the wave frequency ranged 0.2 to 1.1/day, corresponding to wave periods from 5.0 to 0.9 day. Spectra were analyzed by Fourier transforming an auto-correlation function on a 30 day data series, with a maximum lag of 10 days, where the data window was sled every 5 days. Frequency resolution is 0.05/day.

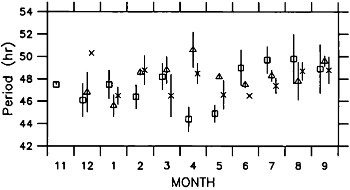

Figure 5.21: Monthly averaged periods of the two-day wave at 90 km in Jakarta from November 1992 to September 1993 calculated using a complex demodulation analysis with the demodulating frequency of 1/48 hr^{-1} and the bandpass filter from 40 to 60 hrs. The periods of eastward component, northward component and temperature fluctuations are shown as squares, triangles and crosses, respectively.

variations. To precisely investigate the seasonal variations of the wave period we employed a complex demodulation technique [*Harris and Vincent*, 1993; *Harris*, 1994]. First, frequency domain bandpass filter with cutoff periods at 40 and 60 hr was applied to the time series, then, the time series were demodulated with a complex sinusoid of the demodulating frequency 1/48 hr^{-1}, and time series of amplitude and phase were obtained. Time differential of the phase corresponds to the frequency difference between the demodulating frequency and the observed wave frequency. Monthly mean wave periods were calculated using data for times when the amplitudes exceeded 10 m/s for u' and v' and 0.01 for T'/T_0 and are shown in Figure 5.21.

During summer months in each hemisphere wave periods were fairly similar among u', v' and T'. During January 1993 to February 1993, i.e., summer months in the southern hemisphere, when the two-day wave was the most active during the observation period, the wave periods were confined around 47 hr, revealing another evidence that the two day oscillations seen in the wind fields and temperature fields were based on the same atmospheric phenomena. While during June

1993 to September 1993, i.e., summer months in the northern hemisphere, wave periods showed larger values centered around 49 hr. The periods of the two-day wave were larger in northern hemisphere summer months, which was consistent with the earlier findings [*Muller and Nelson*, 1978; *Craig and Elford*, 1981; *Tsuda et al.*, 1988a; *Harris and Vincent*, 1993; *Harris*, 1994].

On the other hand, the wave periods during April 1993 exhibited a considerable scatter compared with other months. During this period the dynamic spectra of u' showed an enhancement at periods clearly longer than that of v' as seen in Figure 5.20 (c), implying that the enhancements in u' might be related with different wave activities from v'. Therefore, this non-monochromatic feature seemed to be responsible for the large scatter.

We calculated the variances of the wave energy by integrating the moving power spectra from 0.35–0.65 /day, that is, 69–37 hrs, being wide enough to cover a major part of the two-day wave, and investigated seasonal variations of the two-day wave energy (Figure 5.22 (a)). We also calculated the moving cross spectra between v' and T'/T_0 at 90 km, and plotted the phase values in Figure 5.22 (b) at frequency of 0.45, 0.5 and 0.55 /day, corresponding period of 53.3, 48 and 43.6 hrs, respectively. Note that T'/T_0 led v' in the phase values.

In Figure 5.22 (a) the variance for v' showed enhancement during summer months in each hemisphere, and also a minor event during March and April 1994. The seasonal variations of the variance for potential energy was remarkably similar to that for v' with corresponding clear peaks at January and July–August 1993. The potential energy was comparable to or slightly smaller than the variance of v' by a factor 1/2 to 1. While, variance for u' also showed similar seasonal variations to that of v', where the u' variance was 1/10–1/2 of the u' variance. Note again that the relative amplitudes between u', v' and T'/T_0 are not very easy to compare with theoretical predictions because they are strongly affected by the background conditions.

Another peak in the potential energy existed from the end of February to March 1993, to which no corresponding large peaks were seen for v'. As mentioned earlier not only a single wave seemed to be responsible for the peaks of T'/T_0 during this period. The origin of these peaks can not be identified at present.

In Figure 5.22 (b) the phase values were very stable when large variance was observed in v'. That is, the values were confined around 180° in January, March, April, June, July and September 1993, indicating v' and T'/T_0 were almost always anti-phase. This phase relation was again consistent with the theory of Rossby-gravity waves with no background mean wind condition [*Holton*, 1992]. During February to March 1993 when only T'/T_0 was magnified the phase values were unstable as in Figure 5.22 (b), suggesting again that this event was not

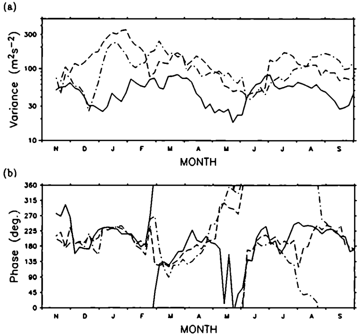

Figure 5.22: (a) Variances of two-day wave component observed in Jakarta at 90 km. Values for u' (solid line), v' (broken line) and $g/N \cdot T'/T_0$ (chained line) were obtained by integrating dynamic auto spectra shown in Figure 5.20 from 0.35 to 0.65 /day, corresponding period of 69-37 hrs. (b) Phase of dynamic cross spectra between v' and $g/N \cdot T'/T_0$ at the frequencies of 0.45 (solid line), 0.50 (broken line) and 0.55 /day (chained line), corresponding periods of 53.3, 48 and 43.6 hrs, respectively, where T'/T_0 led v' by the phase values.

solely associated with the same two-day wave frequently observed in the summer months of the northern and southern hemisphere.

5.4 Discussion and Conclusions

In this chapter we studied global structure of planetary waves by means of cooperative radar observations separated in both latitude and longitude.

In Section 5.1 planetary waves in middle latitudes were studied on the basis of simultaneous observations from May 1983 to March 1986 by the meteor radar in Shigaraki and MF radars in Adelaide (35°S, 138°E) and Saskatoon (52°N, 107°W).

Mean frequency spectra during the observation period showed that two-day waves were the most conspicuous planetary waves in the mesopause region. Using dynamic frequency spectra we picked up planetary scale waves simultaneously observed at the radar sites in period range of 1-10 days. We detected 6 wave events between Shigaraki and Adelaide and 14 between Shigaraki and Saskatoon. This difference may be due to seasonal dependence of planetary wave activity caused by zonal mean winds, as reported for stratospheric planetary waves, because Shigaraki and Saskatoon are located in northern hemisphere, and Adelaide in southern hemisphere.

By comparing observed phase differences between the radar sites with theoretical phase differences assuming motionless atmosphere, we found that several waves could be interpreted as normal mode Rossby waves such as (1, 0), (3, 0), (1, 1), (1, 2) and (2, 2). However, there were also cases that the observed and theoretical phase differences showed considerable discrepancies. A part of these differences seemed to be attributed to modification of global structure of planetary waves due to prevailing zonal winds and latitudinal temperature gradient. Further, fairly small amplitudes of these waves might cause a large estimation error. Superposition of waves also seemed to make it difficult to identify global structure of waves.

In Section 5.2 we analyzed long period wind motions in equatorial mesopause region using meteor radar observations in Jakarta from November 1992 to August 1994 and MF radar in Christmas Island (6°S, 107°W) from November 1992 to December 1993.

Annual mean frequency spectra in 1993 at 90 km revealed the existence of waves with various periods such as tides (24hr, 12hr, 8hr), two-day wave and also zonally concentrated 3-4 day and 6-7 day oscillations at the both sites. Spectral density for period range shorter than 1 day showed a logarithmic slope of about -2, suggesting that these components were due to superposition of gravity waves.

Further, spectral density were generally larger in Jakarta at periods shorter than 4 days by a factor of 1.5-2.5, part of which may be explained by larger wave energy generated by active cloud convection over Indonesia.

Prevailing winds were dominated by semiannual oscillations with westward maxima in equinoxes for zonal component and an annual oscillation flowing from summer to winter hemisphere for meridional component at the both stations. However, significant differences between the stations were also found for both the zonal and meridional components, especially when large westward winds were observed at the vernal equinox of 1993. Large year to year variations were also found. Obtained results showed a reasonable agreement with those of UARS observations.

Waves with periods of 3–4 days and 6–7 days revealed marked enhancements for the zonal components during July–September, 1993 simultaneously at the two stations. They showed quite clear phase differences between the two sites, being fairly constant throughout the observed altitudes, from which the 3–4 day and 6–7 day waves could be interpreted as equatorial Kelvin waves with zonal wavenumbers of 1 and 3, respectively, although there were ambiguities of their zonal wavenumbers because we had data from only two observatories. Observed vertical wavelength of longer than 60 km for the 6-7day wave was largely different from a theoretical value of less than 10 km, to which we can not give an appropriate explanation at present. We will determine global structure of these waves without ambiguities by employing, at least, one more radar observatories. Complementary satellite observations is also needed.

In Section 5.3 we studied the behavior of two-day waves near the mesopause, through the simultaneous wind and temperature observations by taking advantage of radio meteor echo measurement with the MU radar in Shigaraki (35°N, 136°E) and the meteor wind radar in Jakarta (6°S, 107°E).

Simultaneous observations in Shigaraki and Jakarta on July 12–19, 1993 revealed a conspicuous two-day oscillation in both wind and temperature fields, where the values of T'/T_0 were 0.015–0.045 at height range 80–96 km in Shigaraki and 0.055 at 90 km in Jakarta with the corresponding T' of 2.7–8.1 K and 10.5 K, adopting T_0 from CIRA 1986 model atmosphere. These temperature values are considerably larger than the satellite observations of 0.5 K reported by *Rodgers and Prata* [1981]. However, the discrepancy could be caused by the difference in observation techniques and analysis methods between the two techniques. It is notable that the phase of v' and T'/T_0 showed in-phase and anti-phase relations in the northern and southern hemispheres, respectively, which agreed well with the theoretical prediction for Rossby-gravity waves. The phase difference between Shigaraki and Jakarta suggested that the wave propagated westward with a zonal wavenumber of 3 (the exact estimate is 2.76).

For another two-day wave event on August 3-13, 1992 observed in Shigaraki, temperature fluctuations was similar to those in the July 1993 event. Phase relation between v' and T'/T_0 also satisfied the theoretical prediction. However, this event was shown to be associated with a wave with zonal wavenumber 4 instead of 3, which was found through cooperative radar study [*Meek et al.*, 1994].

Seasonal variations of the two-day wave in Jakarta were examined by using data collected from November 1992 to September 1993. Two-day wave exhibited similar enhancement in both wind and temperature fields during summer months of the southern and northern hemispheres with larger values during the former period. Since the two-day wave is known to be enhanced in the summer hemisphere, the enhancement of the latter period on July–August 1993 would be a leakage from the northern hemisphere to the southern hemisphere. Potential energy estimated from T'/T_0 showed somewhat smaller value than kinetic energy for v' by a factor of 1/2 to 1. While kinetic energy for u' was much smaller than for v'.

Wave periods, estimated using a complex demodulation analysis, were fairly stable between u', v' and T'/T_0 when conspicuous wave activity was observed in v'; they were around 47 and 49 hrs during summer months of the southern and northern hemispheres, respectively. When remarkable wave activity was seen in v', phase of T'/T_0 exceeded that of v' by 180–225°, indicating the anti-phase relation.

Other marked enhancements were also seen in T'/T_0 during the end of February to the beginning of March 1993. However, no corresponding enhancements were recognized in v' and they were interpreted to be associated with different wave activities.

These observational results are quite consistent with the early observational and theoretical studies that the two-day wave frequently observed near mesopause is (3, 0) mode of Rossby-gravity wave.

Chapter 6

Summary and Conclusions

This thesis is devoted to the study of atmospheric dynamics near mesopause region by means of newly developed simultaneous wind and temperature observation techniques by utilizing radio scattering from ionized meteor trails.

In Chapter 2 we described development of observation techniques using meteor echoes. Since meteors appear quite randomly and sporadically in a large spatial area, special experimental setup is required for meteor echo observations. First, an antenna with a wide radiation pattern is prefered to survey a large horizontal area. Second, an interferometer in reception is essentially important for accurate determination of meteor echo arrival direction and reflection height. Third, a sophisticated real-time processing software is required to extract only meteor echoes from received signal.

A meteor wind radar was constructed in 1977 in Shigaraki (35°N, 136°E), Japan, equipped with fundamental functions to realize the above stated requirements. The radar was operated until 1986 in Shigaraki. We transported the radar to an observatory (6.4°S, 106.7°E) near Jakarta for observations of equatorial atmosphere after replacing a transmitter, system-installed computer and antennas. Substantial auto-recovery functions were also provided in order to continue unmanned observations for a long period. Observations were continued since November 1992.

We realized a sophisticated meteor observation technique utilizing the versatility of the MU radar. We designed a broad radiation pattern of a transmitting antenna by controlling phases of each antenna, which was proved to be effective to collect larger number of echoes than a pencil-like pattern that is normally used for MST observations. An interferometer with four receiving antennas was composed in the MU radar, whose accuracy was about 0.3–0.6 km in altitude at a zenith angle of 30°, being sufficient enough for studying minute vertical structure of wind fields and diffusion coefficient.

Further, we proposed an improvement for meteor observation technique with the MU radar by equipping external receiving antennas, a meteor detection hardware and a personal computer, which enables us long-period meteor observations in parallel with normal observations of the MU radar.

Distribution of meteor echoes as a function of zenith angle, horizontal distance, height and local time was investigated. Meteor echoes were found to be widely distributed in zenith as large as 70° and 50° for the meteor radar and the MU radar observations, respectively. Most of meteor echoes were detected at 70–110km and 70–105 km with a peak height of 92 km and 88 km for the meteor radar and the MU radar observations. Meteor echo rate showed a very clear diurnal distribution with a peak at 4–5 LT for the meteor radar observations. While, that of the MU radar exhibited a much smoothed daily variations due to an omnidirectional antenna pattern, which reduced a ratio between maximum and minimum number of hourly meteor echoes.

Number of echoes per day for the meteor wind radar in Jakarta ranged from 500 to 1200. While, that of the MU radar observations was as much as 3000–5000. Owing to the fairly high echo acquisition rate we can determine wind velocity and ambipolar diffusion coefficient with a good time-height resolution of about 1 hr×4 km and 1 hr×1 km, for the meteor radar and the MU radar observations, respectively.

In Chapter 3 we studied a theoretical relation between temperature, T, density, ρ, and ambipolar diffusion coefficient, D, inferred from a decay time constant of meteor echo intensity. Employing a theory of ionic diffusion, we obtained a relation, $D \propto T/\rho$. Since T is fairly constant near the mesopause, observed D profile with the MU radar showed an exponential increase with a scale height almost identical to that of atmospheric density. Further, using a Boussinesq approximation, we found a relation between the normalized D and T fluctuations as $T'/T_0 = 1/2D'/D_0$.

Observed T'/T_0 involved fluctuations with various periods, showing coherent structure between different altitudes, among which diurnal variations were investigated in this chapter. In Shigaraki typical amplitude of diurnal variations of T' was about 10 K throughout a year from campaign observations with durations of 2–7 days. In summer phases were fairly constant along height at 04–05LT, which was in contrast to downward phase propagation seen in wind field. The standing phase structure could imply a manifestation of an evanescent diurnal tides or in-situ heating due to solar radiation. On the other hand, in winter months phase of T' often exhibited clear downward phase progression. A typical example showed wavelength of about 25 km in both the wind and temperature fields with phase relations preferably interpreted as a manifestation of $S_{1,1}$ mode diurnal tide. While, in Jakarta monthly mean amplitude of diurnal variations of T' was about 10 K. Phases often showed downward propagations, being interpreted as a manifestation of vertically propagating diurnal tides.

In Chapter 4 characteristics of gravity waves near the mesopause were studied, taking advantage of the good time-height resolutions of temperature and wind observations with the MU radar.

We found that T fluctuations were clearly associated with wave-like structures showing downward phase propagation with periods shorter than the inertial period. Phase relations between observed T'/T_0 and wind velocity fluctuations were consistent with polarization relation predicted by a linear gravity wave theory. Further, we examined amplitude relation between kinetic and potential energy densities calculated from horizontal wind velocity and temperature fluctuations, respectively. The two energy densities coincided well for periods longer than 2 hr, being consistent with the gravity wave theory.

Seasonal variation of horizontal propagation direction of dominant gravity waves was studied from campaign observations in 1990–1992 by means of hodograph analysis. Most of the waves showed downward phase propagations, indicating the upward energy transportation. Mean values of obtained wave periods, vertical and horizontal wavelengths and horizontal phase speed were 11.3 hr, 13.1 km, 2200 km and 52.9 m/s, respectively. Obtained horizontal propagation directions were generally eastward in summer (May–August) and westward in winter (November–December and March), which were fairly consistent with the results of the turbulence echo observations with the MU radar in the mesosphere centered at 70–75 km altitude [*Nakamura et al.*, 1993]. The seasonal variation seems to be related to directional filtering by prevailing zonal winds.

We also conducted comparison observations of mesospheric gravity waves by means of the MU radar in Shigaraki and a sodium lidar in Hachioji (35.6°N, 139.4°E), which are horizontally separated by 310 km. A monochromatic gravity wave was simultaneously observed on the night of December 15-16, 1993. Observed similarities in amplitude and time evolution are an indication of the same gravity wave influences at the observation sites.

In Chapter 5 global structure of planetary waves were investigated by means of cooperative radar observations spaced in latitude and longitude.

Planetary waves in middle latitudes were studied by using meteor radar observations in Shigaraki and MF radar observations in Adelaide (35°S, 138°E) and Saskatoon (52°N, 107°W). Planetary waves were detected in period range of 1–10 days, where several waves could be interpreted as normal mode Rossby waves from their phase differences between the radar sites, although global structure of waves sometimes seemed to be affected by prevailing zonal winds. Further, most of the wave amplitudes were not significant compared with the two-day wave which showed conspicuous activity in summer hemisphere.

Long period waves in equatorial mesopause region were analyzed using meteor radar observations in Jakarta and MF radar in Christmas Island (6°S, 107°W). Prevailing winds were dominated by semiannual oscillations with westward maxima in equinoxes for zonal component and an annual oscillation which flew from summer to winter hemisphere for meridional component at the both stations. Significant differences between the stations were also found for the both components, especially a large westward wind was observed in the first equinox in 1993. Considerable year to year variations of prevailing winds were found in Jakarta as well. Waves with periods of 3–4 days and 6–7 days simultaneously revealed marked enhancements for the zonal components at Jakarta and Christmas Island during July–September 1993. Phase differences observed between the two stations implied that these waves were equatorial Kelvin waves with zonal wavenumbers of one and three, respectively, although there still remain ambiguities. Moreover, observed vertical wavelength of the 6–7 day wave was much longer than the theoretical prediction.

We studied two-day wave using simultaneous wind and T'/T_0 observations in Shigaraki and Jakarta. Observed wind and T'/T_0 exhibited conspicuous two day oscillations, where meridional component and T'/T_0 showed in-phase and antiphase relations in Shigaraki and Jakarta, respectively. Phase difference between the two stations indicated that this wave was a westward propagating wave with a zonal wavenumber of three. Seasonal variations of two-day wave in equatorial mesosphere was also investigated, where both the wind and T'/T_0 showed clear enhancements during summer months in each hemisphere. These results strongly support that the two-day wave near the mesopause can be interpreted as the (3, 0) mode of a Rossby-gravity wave.

In conclusion, we studied atmospheric dynamics near the mesopause in middle and equatorial latitudes by means of radio meteor echo measurements with the meteor radar and the MU radar, together with other radar and lidar observations. We conducted simultaneous observations of wind and temperature fluctuation using meteor echoes, which were proved to be very useful to investigate the behavior of atmospheric waves such as gravity waves, atmospheric tides and planetary waves.

Appendix A

Comparison Experiment between the MU Radar and the Meteor Radar

We present here comparison experiment between meteor measurements with the meteor radar and the MU radar conducted in Shigaraki before the meteor radar was transported to Indonesia.

After the meteor wind radar system was improved for the observations in Indonesia, we started test operation of the radar from April 1992 and collected fairly large amount of data in August 1992 using northward pointing antennas. While, we carried out meteor echo observations with the MU radar on July 31 – August 1, August 3–8 and August 10–13, 1992, which were compared with the simultaneous measurements with the meteor wind radar.

In order to select the identical meteor echoes from the data obtained with the two radars, we picked up 1142 meteor echoes that appeared within 3 seconds of time difference for both radars, and less than 3 km in the ranges during the simultaneous observation periods. Figure A.1 shows the comparison of azimuth angles for the 1142 echoes. Most of the echoes were aligned near the line $y = x$ within the difference of $\pm 10°$. However, some of the echoes showed fairly large discrepancy ranging as much as 100°, which seems to be caused, at least partially, by the ambiguity of the interferometer of the meteor wind radar. Further the contamination of echoes from different meteor trails might also be responsible, because the preferable directions to detect echoes are different between the two radars due to the difference of the transmitting and receiving antenna patterns.

Since we are interested in the accuracy of the angle determination itself, and moreover, the most of the ambiguities can be removed by utilizing other echo characteristics such as decay height, we discarded data which showed more than

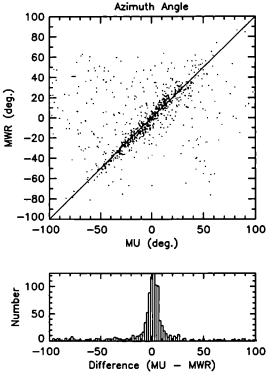

Figure A.1: Top: A scatter diagram of the azimuth angles measured by the MU radar and the meteor radar for simultaneously observed meteor echoes during July, 31 - August 13, 1992. Bottom: Histogram of the azimuth angle differences between the two radar measurements.

20° difference. Then, we considered only the statistical error and found the mean difference and standard deviation of 0.56° and 6.5°, respectively, showing fairly good correlation.

Similar comparison was also done for elevation angle measurement. By selecting echoes within 20° elevation angle difference we obtained the mean difference and the standard deviation of 0.94° and 5.25°, respectively.

As for the radial wind velocity, comparison was conducted for 807 meteor echoes whose azimuth and elevation angle differences were within 20°, as shown in Figure A.2. We conducted a least square fitting to the data and found the best fitted line given by $y = 0.96x - 0.7$ with a correlation coefficient of 0.82 shown as dashed line in Figure A.2. The mean difference and standard deviation were -0.26 m/s and 8.59 m/s, respectively.

Figure A.3 shows comparison of northward wind velocity between the meteor wind radar and the MU radar on August 3-8, 1992 every 2 km altitude with a time resolution of 2 hours, where typical standard deviations were 20 m/s and 15 m/s, respectively. Similar temporal variations were recognized with each other although the wind velocity by the meteor wind radar was difficult to be obtained in the evening hours due to lower echo rate.

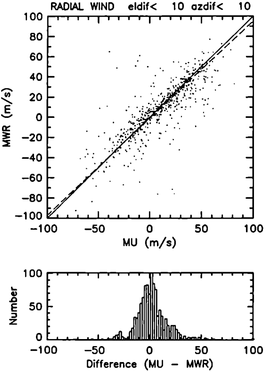

Figure A.2: Same as Figure A.1 except for radial wind velocity measurements. Meteor echoes whose azimuth and zenith angle differences between the MU radar and the meteor radar were less than 20° are plotted.

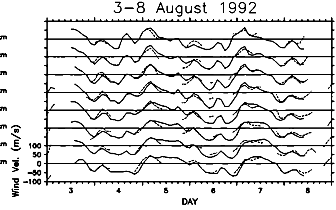

Figure A.3: Time series of northward wind velocity observed on August 3-8, 1992 in Shigaraki. Results for the MU radar and the meteor wind radar are shown by solid and dashed lines, respectively.

Appendix B

Receiving Antenna of the MU/Meteor Monitor

In Section 2.2.3 we briefly described that a dipole antenna is advantageous to the Yagi antenna in the MU radar in receiving a large number of meteor echoes from a wider spatial area. In this appendix we present numerically calculated radiation patterns of receiving antennas and also the results of comparison experiments between the dipole and Yagi antennas.

The three-element crossed Yagi antenna used in the MU radar has the radiation pattern with its maximum gain at $\theta = 0$ as shown Figure B.1. While, the radiation pattern of a dipole antenna significantly varies with the antenna height from the ground, thus we designed a preferable antenna pattern for meteor observations. The antenna directivity of horizontally polarized component is given for horizontally arranged dipole antenna with the height, h, as

$$D(\phi) = \sin(kh\sin(\phi)) \tag{B.1}$$

where k is wave number, and ϕ is zenith angle. The antenna patterns for h of $1/8\lambda$, $1/4\lambda$, $3/8\lambda$ and $1/2\lambda$ are shown in Figure B.2. We employed the dipole antennas at the height of $3/8\lambda$, which has the maximum gain at the zenith angle of around 45°.

We conducted an experiment on December 3-4, 1990 using a crossed dipole antenna at the height of $3/8\lambda$ from the ground for the receiver channel 4, where three out of four receiver channels (channels 1-3) were connected to the internal Yagi antennas of the MU radar, constructing an interferometer. The maximum sample range was set to 183 km. The range distribution of meteor echoes is shown in Figure B.3 for each receiver channel. Distribution for channels 1-3 had a peak around 100 km and rapidly decreased in number with range. The echo

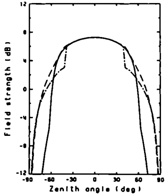

Figure B.1: Computed radiation pattern of the optimized 3-element Yagi's in the infinite array for the case where x-aligned elements are excited. Solid and dashed curves, and chain are for the directions of 0° (x-z plane), 45°, and 90° (x-z plane), respectively [*Sato*, 1981].

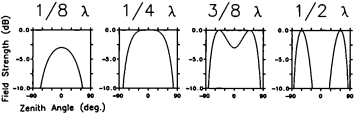

Figure B.2: Computed radiation patterns of x-aligned dipole antennas for the direction of x-z plane. Four figures correspond to the antenna heights of 1/8λ, 1/4λ, 3/8λ and 1/2λ, respectively.

numbers were 4645, 4266 and 4671 for channel 1, 2 and 3, respectively. While, the distribution for channel 4 did not show a clear peak but quite a gradual decrease with range. Total echo number was 4909, which was 1.05–1.15 times larger than those of channels 1–3. In this experiment maximum sample range was restricted to 183 km due to system limit, arising from the size of main memory of the MU radar. However, for the MU/Meteor monitor we can enlarge the sample range without such a limit, indicating that number of echoes will further increase.

The ratio of echo power received with the dipole antenna to the average echo power received with the three Yagi antennas is plotted in Figure B.4 for echoes received with all of the four antennas. Note that the zenith angles were determined with the interferometer using channels 1–3, and were estimated by decay height method for echoes with the range smaller and larger than 127 km, respectively. The ratio clearly increased with zenith angles as seen in Figure B.4. At the zenith angles larger than about 40° the echo power of the crossed dipole antenna became larger than that of the Yagi antenna. These results indicate that the dipole antenna takes an advantage of the Yagi antenna in receiving a large number of echoes for a larger zenith angles.

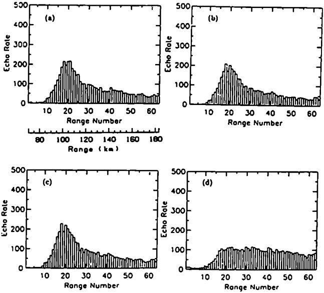

Figure B.3: The range distribution of meteor echoes obtained by the experiment on December 3-4, 1990. (a), (b), (c) and (d) correspond to the receiver channel 1, 2, 3 and 4, respectively. The channels, 1, 2 and 3, were connected to the internal Yagi antennas of the MU radar. The channel 4 was connected to the crossed dipole antenna located at the height of $3/8\lambda$ from the ground level.

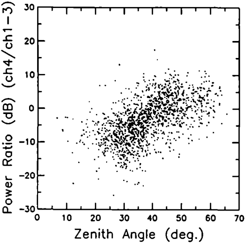

Figure B.4: The ratio of echo power received with the dipole antenna to the average echo power received with the three Yagi antennas. The zenith angles were determined with the interferometer using channels 1–3, and estimated by decay height method for echoes with range shorter and longer than 127 km, respectively.

Appendix C

Effects of Local Topography to Radiation Pattern of the Jakarta Meteor Radar

In this appendix we discuss the irregular zenith angle distributions found for the meteor radar observations in Jakarta [*Fujioka*, 1993].

Figure C.1 presents zenith angle distribution of meteor echoes obtained with the southward antenna beam on December 1-31, 1992, where echoes were widely distributed from 10° to 75°. Note that irregular enhancements were superimposed on the zenith angle distribution, which seems to be caused by a modulation of antenna radiation pattern due to an interference between the direct and reflected radio waves by the local topography. Figure C.2 schematically shows the situation, where λ, θ and h are the wavelength, zenith angle and antenna height from the reflector (ground). When the following relation is satisfied, the direct and reflected radio waves become in phase and antenna gain should increase.

$$2h \sin\theta = (\frac{1}{2} + n)\lambda \tag{C.1}$$

where n is a integer. In the case of $h = 40$ m, which roughly corresponds to the surrounding topography of the site, the solutions for θ are indicated in Figure C.1 by thick vertical lines, which agree quite well the enhancements in the distribution.

These enhancements, however, are not preferable when we investigate true spatial distribution of meteor echoes. Therefore, we have altered the antenna beam direction to northward since June 9, 1993 after conducting experimental operation with the northward antenna beam during March 11-17, 1993.

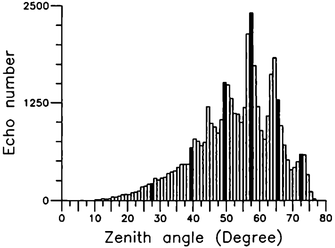

Figure C.1: Zenith angle distribution of meteor echoes observed in Jakarta with the southward antenna beam on December 1-31, 1992.

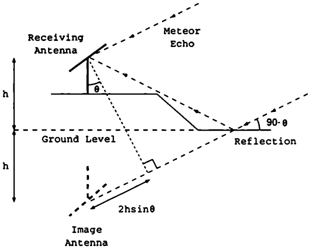

Figure C.2: Schematic figure showing antenna interference, where λ, θ and h are the wavelength, elevation angle and antenna height from the reflector.

References

Aikin, A. C., and R. D. McPeters, Meteoric material and the behavior of upper stratospheric polar ozone, *Geophys. Res. Lett.*, *17*, 1300-1303, 1986.

Andrews, D. G., J. R. Holton, and C. B. Leovy, *Middle Atmosphere Dynamics*, Academic Press, New York, 489pp, 1987.

Aso, T., T. Tsuda, and S. Kato, Meteor radar observations at Kyoto University, *J. Atmos. Terr. Phys.*, *41*, 517-525, 1979.

Aso, T., T. Tsuda, Y. Takashima, R. Ito, and S. Kato, Observations of Lower Ionospheric Wind by the Kyoto Meteor Radar, *J. Geophys. Res.*, *85*, 177-184, 1980.

Aso, T., T. Nonoyama, and S. Kato, Numerical simulation of semidiurnal atmospheric tides, *J. Geophys. Res.*, *86*, 11388-11400, 1981.

Aso, T., S. Ito, and S. Kato, Background wind effect on the diurnal tide in the middle atmosphere, *J. Geomag. Geoelectr.*, *39*, 297-305, 1987.

Avery, S. K., A. C. Riddle, and B. B. Balsley, The Poker Flat, Alaska, MST radar as a meteor radar, *Radio Sci.*, *18*, 1021-1027, 1983.

Baggaley, W. J., Multi frequency studies of radio-meteor train diffusion, *Bull. Astron. Inst. Czechosl.*, *31*, 305-308, 1980.

Baggaley, W. J., Single wavelength measurements of the initial radii of radio meteor ionization columns, *Bull. Astron. Inst. Czechosl.*, *32*, 345, 1981.

Beatty, T. J., C. A. Hostetler, and C. S. Gardner, Lidar observations of gravity waves and their spectra near the mesopause and stratopause at Arecibo, *J. Atmos. Sci.*, *49*, 477-496, 1992.

CIRA 1986, *COSPAR International Reference Atmosphere: 1986*, Part II: Middle Atmosphere Models (D. Ress, J. J. Barnett and K. Labitzke), Pergamon Press, 1990.

Collins, R. L., A. Nomura, and C. S. Gardner, Gravity waves in the upper mesosphere over Antarctica: Lidar observations at the South pole and Syowa, *J.*

Geophys. Res., *99*, 5475-5485, 1994.

Craig, R. L., and W. G. Elford, Observations of the quasi 2-day wave near 90 km altitude at Adelaide (35°S), *J. Atmos. Terr. Phys.*, *43*, 1051-1056, 1981.

Craig, R. L., R. A. Vincent, S. P. Kingsley, and H. G. Muller, Simultaneous observations of the quasi 2-day wave in the northern and southern hemisphere, *J. Atmos. Terr. Phys.*, *45*, 539-541, 1983.

Devara, P. C. S., Mohammed Iqhbal Ahmed, and M. Srirama Rao, Echo duration and diffusion coefficient measurements using meteor wind radar, *Radio Sci.*, *16*, 111-119, 1981.

Dunkerton, T. J., Theory of the mesopause semiannual oscillation, *J. Atmos. Sci.*, *39*, 2681-2690, 1982.

Ebel, A., A. H. Manson, and C. E. Meek, Short period fluctuations of the horizontal wind measured in the upper middle atmosphere and possible relationships to internal gravity waves, *J. Atmos. Terr. Phys.*, *49*, 385-401, 1987.

Eckermann, S. D., and R. A. Vincent, First observations of intraseasonal oscillations in the equatorial mesosphere and lower thermosphere, *J. Geophys. Res.*, submitted, 1993.

Forbes, J. M., Atmospheric tides, 1, Model description and results for the solar diurnal component, *G. Geophys. Res.*, *87*, 5222-5240, 1982.

Forbes, J. M., Middle atmosphere tides, *J. Atmos. Terr. Phys.*, *46*, 1049-1067, 1984.

Forbes, J. M., and M. E. Hagan, Diurnal propagating tide in the presence of mean winds and dissipation: a numerical investigation, *Planet. Space Sci.*, *36*, 579-590, 1988.

Forbes, J. M., and F. Vial, Monthly simulation of the solar semidiurnal tide in the mesosphere and lower thermosphere, *J. Atmos. Terr. Phys.*, *51*, 649-661, 1989.

Franke, S. J., T. Beatty, D. Thorsen, C. H. Liu, C. S. Gardner, F. L. Roesler, and J. Harlander, Simultaneous Na lidar and HF radar observations of vertical velocities in the mesosphere over Urbana, IL, *Geophys. Res. Lett.*, *17*, 69-72, 1990.

Fritts, D. C. and P. K. Rastogi, Convective and dynamical instabilities due to gravity wave motions in the lower and middle atmosphere: Theory and observations, *Radio Sci.*, *20*, 1247-1277, 1985.

Fukao, S., T. Sato, T. Tsuda, S. Kato, K. Wakasugi, and T. Makihira, The MU radar with an active phased array system, 1. Antenna and power amplifiers, *Radio Sci.*, *20*, 1155–1168, 1985a.

Fukao, S., T. Tsuda, T. Sato, S. Kato, K. Wakasugi, and T. Makihira, The MU radar with an active phased array system, 2. In-house equipment, *Radio Sci.*, *20*, 1169–1176, 1985b.

Gage, K. S., and G. D. Nastrom, Theoretical interpretation of atmospheric wavenumber spectra of wind and temperature observed by commercial aircraft during GASP, *J. Atmos. Sci.*, *43*, 729–740, 1986.

Garcia, R. R., and S. Solomon, Numerical model of the zonally averaged dynamical and chemical structure of the middle atmosphere, *J. Geophys. Res.*, *88*, 1379–1400, 1983.

Gardner, C. S., and D. G. Voelz, Lidar studies of the nighttime sodium layer over Urbana, Illinois, 2, Gravity waves, *J. Geophys. Res.*, *92*, 4673-4694, 1987.

Gardner, C. S., D. C. Senft, T. J. Beatty, R. E. Bills, and C. A. Hostetler, Rayleigh and sodium lidar techniques for measuring middle atmosphere density, temperature and wind perturbations and their spectra, in *World Ionosphere/Thermosphere Study Handbook*, vol. 2, edited by C. H. Liu and B. Edwards, pp. 148-187, International Congress of Scientific Unions, Urbana, Ill., 1989.

Gossard, E. E., and W. H. Hooke, *Waves in the Atmosphere*, vol. 2, *Development in Atmospheric Science*, Elsevier Science, New York, 1975.

Greenhow, J. S., and J. E. Hall, Diurnal variations of density and scale height in the upper atmosphere, *J. Atmos. Terr. Phys.*, *18*, 203–214, 1960.

Greenhow, J. S., and J. E. Hall, The height variation of the ambipolar diffusion coefficient for meteor trails, *Planet. Space Sci.*, *5*, 109–114, 1961.

Greenhow, J. S., and E. L. Neufeld, The diffusion of ionized meteor trails in the upper atmosphere, *J. Atmos. Terr. Phys.*, *6*, 133–140, 1955.

Hagan, M. E., J. M. Forbes, and F. Vial, Numerical investigation of the propagation of the quasi-two-day wave into the lower thermosphere, *J. Geophys. Res.*, *98*, 23193–23205, 1993.

Hamilton, K., Rocketsonde observations of the mesospheric semiannual oscillation at Kwajalein, *Atmosphere-Ocean*, *20*, 281-286, 1982.

Harris, T. J., and R. A. Vincent, The quasi-two-day wave observed in the equatorial middle atmosphere, *J. Geophys. Res.*, *98*, 10481–10490, 1993.

Harris, T. J., A long-term study of the quasi-two-day wave in the middle atmosphere, *J. Atmos. Terr. Phys., 56*, 569-579, 1994.

Hauchecorne, A., M. L. Chanin, and R. Wilson, Mesospheric temperature inversion and gravity wave breaking, *Geophys. Res. Lett., 14*, 933-936, 1987.

Hawkins, G. S., Variations in the occurrence rate of meteors, *Astron. J., 61*, 386-391, 1956a.

Hawkins, G. S., A radio survey of sporadic meteor radiants, *Mon. Not. R. astr. Soc., 116*, 92–104, 1956b.

Herlofson, N., The theory of meteor ionization, *Repts. Prog. Phys., 11*, 444–454, 1948.

Hess, G. C., and M. A. Geller, The Urbana Meteor-Radar System: Design, development, and first observations, *Aeron. Rep., 74*, Univ. Illinois, Urbana, Ill., U.S.A., 1976.

Hines, C. O., Diurnal variations in forward-scattered meteor signals, *J. Atmos. Terr. Phys., 9*, 229–232, 1956.

Hines, C. O., Internal atmospheric gravity waves at ionospheric heights, *Can. J. Phys., 38*, 1441-1481, 1960.

Hirooka, T., and I. Hirota, Normal mode Rossby waves observed in the stratosphere. Part II: Second antisymmetric and symmetric modes of zonal wavenumber 1 and 2, *J. Atmos. Sci., 42*, 536–548, 1985.

Hirooka, T., and I. Hirota, Further evidence of normal mode Rossby waves, *PAGEOPH 130*, 277-289, 1989.

Hirota, I., Equatorial waves in the upper stratosphere and mesosphere in relation to the semiannual oscillation of the zonal wind, *J. Atmos. Sci., 35*, 714–722, 1978.

Hirota, I., Observational evidence of the semiannual oscillation in the tropical atmosphere - A review, *PAGEOPH, 118.*, 217–238, 1980.

Hirota, I., and T. Hirooka, Normal mode Rossby waves observed in the upper stratosphere. Part I: First symmetric modes of zonal wavenumber 1 and 2, *J. Atmos. Sci., 41*, 1253–1267, 1984.

Holton, J. R., *An Introduction to Dynamic Meteorology*, Third edition, Academic Press, 1992.

Hostetler, C. A., and C. S. Gardner, Observations of horizontal and vertical wavenumber spectra of gravity wave motions in the stratosphere and mesosphere over the mid-Pacific, *J. Geophys. Res.,*, in press, 1994.

Hughes, D. W., *Cosmic Dust*, edited by J. A. M. McDonnell, Wiley, Chichester, 1978.

Huuskonen, A., T. Nygrén, L. Jalonen, N. Bjørnå, T. L. Hansen, A. Brekke, and T. Turunen, Ion composition of sporadic E layers measured by the EISCAT UHF radar, *J. Geophys. Res.*, 93, 14603–14610, 1988.

Huxley, L. G. H., The persistence of meteor trails, *Aust. J. Sci. Res.*, *5*, 10-16, 1952.

Ito, R., T. Tsuda, T. Aso, and S. Kato, Long period of oscillations in the meteor winds observed over Kyoto during 1978-1983, *J. Geomag. Geoelectr.*, *36*, 173-188, 1984.

Jones, J., On the decay of underdense radio meteor echoes, *Mon. Not. R. astr. Soc.*, *173*, 637-647, 1975.

Jones, W., and J. Jones, Ionic diffusion in meteor trains, *J. Atmos. Terr. Phys.*, *52*, 185-191, 1990.

Kaiser, T. R., Radio echo studies of meteor ionization, *Phil. Mag.*, *2*, 495–495, 1953.

Kato, S., Diurnal atmospheric oscillation, 1. eigenvalues and Hough functions, *J. Geophys. Res.*, *71*, 3201-3209, 1966.

Kato, S., *Dynamics of the upper atmosphere*, 233pp., D. Reidel Publ. Co., Dordrecht, 1980.

Kirkwood, S., and U. von Zahn, On the role of auroral electric fields in the formation of low altitude sporadic-E and sudden sodium layers, *J. Atmos. Terr. Phys.*, *53*, 389–407, 1991.

Kwon, K. H., C. S. Gardner, S. K. Avery, and J. P. Avery, Correlative radar and airborne sodium lidar observations of the vertical and horizontal structure of gravity waves near the mesopause, *J. Geophys. Res.*, *95*, 13,723-13,748, 1990.

Lieberman, R. S., M. D. Burrage, D. A. Gell, P. B. Hays, A. R. Marshall, D. A. Ortland, W. R. Skinner, D. L. Wu, R. A. Vincent, and S. J. Franke, Zonal mean winds in the equatorial mesosphere and lower thermosphere observed by the high resolution Doppler imager, *Geophys. Res. Lett.*, *20*, 2849-2852, 1993.

Lindzen, R. S., Thermally driven diurnal tide in the atmosphere, *Quart. J. Roy. Meteor. Soc.*, *93*, 18-42, 1967.

Lindzen, R. S., and J. R. Holton, A theory of the quasi-biennial oscillation, *J. Atmos. Sci*, *25*, 1095–1107, 1968.

Lindzen, R. S., Turbulence and stress owing to gravity wave and tidal breakdown, *J. Geophys. Res., 86*, 9707-9714, 1981.

Longuet-Higgins, M. S., The eigenfunctions of Laplace's tidal equations over a sphere, *Phil. Trans. Roy. Soc. London, a262*, 511–607, 1968.

Madden, R. A., and Julian, P. R., Further evidence of global-scale 5-day pressure waves, *J. Atmos. Sci., 29*, 1464–1469, 1972.

Madden, R. A., and Julian, P. R., Reply, *J. Atmos. Sci., 30*, 935–940, 1973.

Manning, L. A., O. G. Villard, and A. M. Peterson, Meteoric echo study of upper atmospheric winds, *Proc. IRE, 38*, 877–883, 1950.

Manson, A. H., C. E. Meek, J. L. Fellous, and M. Massebeuf, Winds oscillations (~6h-6days) in the upper middle atmosphere at Monpazier (France, 45°N, 1°E) and Saskatoon (Canada, 52°, 107°W) in 1979–1980, *J. Atmos. Terr. Phys., 49*, 1059–1069, 1987.

Manson, A. H., and C. E. Meek, Gravity wave propagation characteristics (60-120 km) as determined by the Saskatoon MF radar (Gravnet) system: 1983-1985 at 52°N, 107°W, *J. Atmos. Sci., 45*, 932-946, 1988.

Mason, B., *Handbook of Elemental Abundances of Meteorites*, New York: Gorden and Breach, 1971.

Matsuno, T., Quasi-geostrophic motions in the equatorial area, *J. Meteoral. Soc. Japan, 44*, 25–42, 1966.

Matsuno, T., A quasi-one-dimensional model of the middle atmospheric circulation interacting with internal gravity waves, *J. Meteorol. Soc. Japan, 60*, 215-226, 1982.

McDaniel, E. W., and E. A. Mason, *The mobility and diffusion of ions in gases.*, Wiley, 1973.

McKinley, D. W. R., *Meteor Science and Engineering*. McGraw-Hill, New York, 1961.

Meek, C. E., I. M. Reid, and A. H. Manson, Observations of mesospheric wind velocities 1. Gravity wave horizontal scales and phase velocities determined from spaced wind observations, *Radio Sci., 20*, 1363-1382, 1985.

Meek, C. E., A. H. Manson, S. J. Franke, W. Singer, P. Hoffmann, R. R. Clark, T. Tsuda, T. Nakamura, M. Tsutsumi, M. Hagan, D. C. Fritts, J. Isler, and Yu I. Portnyagin, Global study of northern hemisphere quasi-2-day wave events in the summers of 1991 and 1992, Submitted, *J. Atmos. Terr. Phys.*, 1994.

Miyahara, S., Yu. I. Portnyagin, J. M. Forbes, and T. V. Solovjeva, Mean zonal acceleration and heating of the 70- to 100-km region, *J. Geophys. Res.*, *96*, 1225-1238, 1991.

Muller, H. G., and L. Nelson, A traveling quasi 2-day wave in the meteor region, *J. Atmos. Terr. Phys.*, *40*, 761–766, 1978.

Murayama, Y., T. Tsuda, M. Yamamoto, T. Nakamura, T. Sato, S. Kato, and S. Fukao, Dominant vertical scales of gravity waves in the middle atmosphere observaed with the MU radar and rocketsondes, *J. Atmos. Terr. Phys.*, *54*, 339–346, 1992.

Murayama, Y., T. Tsuda, and S. Fukao, Seasonal variation of gravity wave activity in the lower atmosphere observed with the MU radar, *J. Geophys. Res.*, *99*, 23057–23069, 1994.

Murray, E. L., Ambipolar diffusion of a meteor trail and its relation with height, *Planet. Space Sci.*, *1*, 125–129, 1959.

Nagasawa, C., and M. Abo, Lidar observations of a lot of sporadic sodium layers in mid-latitude, Submitted, *Geophys. Res. Lett.*, 1994.

Nakamura, T., T. Tsuda, M. Tsutsumi, K. Kita, T. Uehara, S. Kato, and S. Fukao, Meteor wind observations with the MU radar, *Radio Sci.*, *26*, 857–869, 1991.

Nakamura, T., T. Tsuda, M. Yamamoto, S. Fukao, and S. Kato, Characteristics of gravity waves in the mesosphere observed with the middle and upper atmosphere radar, 1, Momentum flux, *J. Geophys. Res.*, *98*, 8899-8910, 1993.

Nakamura, T., T. Tsuda, and S. Fukao, Mean winds at 60–90 km observed with the MU radar (35°N) *J. Atmos. Terr. Phys.*, in press, 1995.

Namboothiri, S. P., T. Tsuda, M. Tsutsumi, T. Nakamura, C. Nagasawa, and M. Abo, Simultaneous observations of mesospheric gravity waves with the MU radar and the Sodium lidar, *J. Geophys. Res.*, *submitted*, 1994.

Newell, R. E., and Gould-Stewart, S., A stratospheric fountain?, *J. Atmos. Sci.*, *38*, 2789–2796, 1981.

Ogawa, T., A. Nomura, T. Tanaka, and K. Igarashi, Simultaneous measurements of antarctic mesospheric gravity waves by meteor radar and lidar, *J. Geomag. Geoelectr.*, *41*, 835-849, 1989.

Olsson-Steel, D., and W. G. Elford, The height distribution of radio meteors: observations at 2 MHz, *J. Atmos. Terr. Phys.*, *49*, 243–258, 1987.

Palo, S. E., and S. K. Avery, Mean winds and the semiannual oscillation in the mesosphere and lower thermosphere at Christmas Island, *J. Geophys. Res.*, *98*, 20385–20400, 1993.

Plane, J. M. C., The chemistry of meteoric metals in the earth's upper atmosphere, *International reviews in physical chemistry, 10*, 55–106, 1991.

Plumb, R. A., R. A. Vincent, and R. L. Craig, The quasi-two-day wave event of January 1984 and its impact on the mean mesospheric circulation, *J. Atmos. Sci., 44*, 3030–3036, 1987.

Reddy, C. A., and C. R. Reddi, Longitudinal differences and inter-annual variations of zonal wind in the tropical stratosphere and troposphere, *J. Atmos. Terr. Phys., 48*, 1085-1092, 1986.

Reed, R. J., The quasi-biennial oscillation of the atmosphere between 30 and 50 km over Ascension Island, *J. Atmos. Sci., 22*, 331–333, 1965.

Rodgers, C. D., and A. J. Prata, Evidence for a traveling two-day wave in the middle atmosphere, *J. Geophys. Res., 86*, 9661-9664, 1981.

Rodgers, C. D., Coordinated Study of the Behavior of the Middle Atmosphere in Winter (PMP-1), *Handbook for MAP, 12*, 1–59, 1984.

Rüster, R., VHF radar observations of nonlinear interactions in the summer polar mesosphere, *J. Atmos. Terr. Phys., 56*, 1289–1092, 1994.

Salby, M. L., and R. G. Roper, Long-period oscillations in the meteor region, *J. Atmos. Sci., 37*, 237–144, 1980.

Salby, M. L., The 2-day wave in the middle atmosphere: observations and theory, *J. Geophys. Res., 86*, 9654–9660, 1981a.

Salby, M. L., Rossby normal modes in nonuniform background configurations. Part II: Equinox and solstice conditions, *J. Atmos. Sci., 38*, 1827–1840, 1981b.

Salby, M. L., D. L. Hartmann, P. L. Bailey, and J. C. Gille, Evidence for equatorial Kelvin modes in Nimbus-7 LIMS, *J. Atmos. Sci., 41*, 220-235, 1984.

Sato, T., *Coherent radar measurements of the middle atmosphere and design concepts of the MU radar*, Ph.D thesis, Dep. of Electr. Eng., Kyoto Univ., Kyoto, Japan, 1981.

Senft, D. C., and C. S. Gardner, Seasonal variability of gravity wave activity and spectra in the mesopause region at Urbana, *J. Geophys. Res., 96*, 17229-17264, 1991.

She, C. Y., J. R. Yu, J. W. Huang, C. Nagasawa, and C. S. Gardner, Na temperature lidar measurements of gravity wave perturbations of wind, density and temperature in the mesopause region, *Geophys. Res. Lett., 18*, 1329–1331, 1991.

She, C. Y., J. R. Yu, and H. Chen, Observed thermal structure of a midlatitude mesopause, *Geophys. Res. Lett., 20*, 567–570, 1993.

Shibata, T., T. Kukuda, and M. Maeda, Density fluctuations in the middle atmosphere over Fukuoka observed by a XeF Rayleigh lidar, *Geophys. Res. Lett., 13*, 1121-1124, 1986.

Shimazaki, T., *Minor Constituents in the Middle Atmosphere* (Dordrecht: Reidel), 1985.

Stull, Ronald B., An Introduction to Boundary Layer Meteorology. Kluwer Academic Publishers, Dordrecht / Boston /London, 1988.

Sugar, G. R., Radio propagation by reflection by meteor trails, *Proc. IEEE, 52*, 116–136, 1964.

Teitelbaum, H., and F. Vial, On tidal variability induced by nonlinear interaction with planetary waves, *J. Geophys. Res., 96*, 14169–14178, 1991.

Thomas, R. M., P. S. Whitham, and W. G. Elford, Response of high frequency radar to meteor backscatter, *J. Atmos. Terr. Phys., 50*, 703–724, 1988.

Tohmatsu, T., *Compedium of aeronomy*, Terra scientific publishing company, Kluwer academic publishers, 1990

Tsuda, T., *Kyoto meteor radar and its application to observation of atmospheric tides,*, Ph.D thesis, Dep. of Electr. Eng., Kyoto Univ., Kyoto, Japan, 1982.

Tsuda, T., T. Nakamura, and S. Kato, Mean winds observed by the Kyoto meteor radar in 1983-1985, *J. Atmos. Terr. Phys., 49*, 461-466, 1987.

Tsuda, T., S. Kato, and R. A. Vincent, Long period wind oscillations observed by the Kyoto meteor radar and comparison of the quasi-2 day wave with Adelaide HF radar observations, *J. Atmos. Terr. Phys., 50*, 225-230, 1988a.

Tsuda, T., S. Kato, A. H. Manson, and C. E. Meek, Characteristics of semidiurnal tides observed by the Kyoto meteor radar and Saskatoon Medium-Frequency radar, *J. Geophys. Res., 93*, 7027-7036, 1988b.

Tsuda, T., S. Kato, T. Yokoi, T. Inoue, M. Yamamoto, T. E. VanZandt, S. Fukao, and T. Sato, Gravity waves in the mesosphere observed with the middle and upper atmosphere radar, *Radio Sci., 26*, 1005-1018, 1990.

Tsuda, T., Y. Murayama, K.-I. Oyama, H. Kanzawa, T. Nakamura, M. D. Yamanaka, S. Fukao, and S. Kato, Rocketsonde observations of the middle atmosphere dynamics at Uchinoura (31°N, 131°E) during DYANA campaign. Part II: Characteristics of gravity waves, *J. Geomag. Geoelectr., 44*, 1009–1023, 1992.

Tsuda, T., Y. Murayama, H. Wiryosumarto, S. W. B. Harijono, and S. Kato, Radiosonde observations of equatorial atmosphere dynamics over Indonesia 2. Characteristics of gravity waves, *J. Geophys. Res.*, *99*, 10507–10516. 1994.

Tsuda, T., S. Fukao, M. Yamamoto, T. Nakamura, M. D. Yamanaka, T. Adachi, H. Hashiguchi, N. Fujioka, M. Tsutsumi, S. W. B. Harijono, T. Sribimawati, B. P. Sitorus, R. B. Yhya, M. Karmini, F. Renggono, B. L. Parapat, W. Djojonegoro, P. Mardio, N. Adikusumah, H. T. Endi, and H. Wiryosumarto, A preliminary report on observations of equatorial atmosphere dynamics in Indonesia with radars and radiosondes, *J. Meteorol. Soc. Japan, in press,* 1995.

Tsutsumi, M., T. Tsuda, T. Nakamura, and S. Fukao, Temperature fluctuations near the mesopause inferred from meteor observations with the middle and upper atmosphere radar, *Radio Sci.*, *29*, 599–610, 1994a.

Tsutsumi, M., T. Tsuda, T. Nakamura, and S. Fukao, Wind Velocity and Temperature Fluctuations due to a Two-day Wave Observed with Radio Meteor Echoes, *J. Geophys. Res.*, *submitted*, 1994b.

Vial, F., Numerical simulations of atmospheric tides for solstice conditions, *J. Geophys. Res.*, *91*, 8955–8969, 1986.

Vial, F., Tides in the middle atmosphere, *J. Atmos. Terr. Phys.*, *51*, 3–17, 1989.

Vincent, R. A., and I. M. Reid, HF Doppler measurements of mesospheric gravity wave momentum fluxes, *J. Atmos. Sci.*, *40*, 1321–1333, 1983.

Vincent, R. A., MF/HF radar measurements of the dynamics of the mesopause region–A review, *J. Atmos. Terr. Phys.*, *46*, 961–974, 1984.

Vincent, R. A., T. Tsuda, and S. Kato, A comparative Study of Mesospheric Solar Tides Observed at Adelaide and Kyoto, *J. Geophys. Res.*, *93*, 699–708, 1988.

Vincent, R. A., T. Tsuda, and S. Kato, Asymmetries in mesospheric tidal structure, *J. Atmos. Terr. Phys.*, *51*, 609–616, 1989.

Vincent, R. A., Long-period motions in the equatorial mesosphere, *J. atmos. Terr. Phys.*, *55*, 1067–1080, 1993a.

Vincent, R. A., Low frequency dynamics of the equatorial mesosphere, in *Coupling processes in the lower and middle atmospheres*, edited by E. V. Thrane et al., pp. 125–136, Kluwer, Dordrecht, 1993b.

Vincent, R. A., and D. Lesicar, Dynamics of the equatorial mesosphere: First results with a new generation partial reflection radar, *Geophys. Res. Lett.*, *18*, 825–828, 1991.

Wang, S. T., D. Tetenbaum, B. B. Balsley, R. L. Obert, S. K. Avery, and J. P. Avery, A meteor echo detection and collection system for use on VHF radars, *Radio Sci.*, *23*, 46-54, 1988.

Watanabe, J., T. Nakamura, M. Tsutsumi, and T. Tsuda, Radar Observation of Strong Activity of Perseid Meteor Shower in 1991, *Publications of the Astronomical Society of Japan*, *44*, 677-685 1992.

Weiss, A. A., Diffusion coefficient from the rate of decay of meteor trails, *Aust. J. Phys.*, *8*, 279–288, 1955.

Whitehead, J. D., Production and prediction of sporadic E, *Rev. Geophys.*, *8*, 65–144, 1970.

Wilson, R., M. L. Chanin, and A. Hauchecorne, Gravity waves in the middle atmosphere observed by Rayleigh lidar 1. i Case studies, *J. Geophys. Res.*, *96*, 5153-5167, 1991.

Yamamoto, M., T. Tsuda, and S. Kato, Gravity waves observed by the Kyoto meteor radar in 1983–1985, *J. Atmos. Terr. Phys.*, *48*, 597–603, 1986.

Reference is also made to the following unpublished material:

Fujioka, N., Meteor wind radar observations of equatorial atmosphere in Indonesia, Master thesis, Dep. of Electr. Eng., Kyoto Univ., Kyoto, Japan, 1993.

Publication List

1. Nakamura, T., T. Tsuda, M. Tsutsumi, K. Kita, T. Uehara, S. Kato, and S. Fukao, Meteor wind observations with the MU radar, *Radio Sci., 26*, 857–869, 1991.

2. Watanabe, J., T. Nakamura, M. Tsutsumi, and T. Tsuda, Radar Observation of Strong Activity of Perseid Meteor Shower in 1991, *Publications of the Astronomical Society of Japan, 44*, 677-685 1992.

3. Tsutsumi, M., T. Tsuda, T. Nakamura, and S. Fukao, Temperature fluctuations near the mesopause inferred from meteor observations with the middle and upper atmosphere radar, *Radio Sci., 29*, 599–610, 1994.

4. Tsuda, T., S. Fukao, M. Yamamoto, T. Nakamura, M. D. Yamanaka, T. Adachi, H. Hashiguchi, N. Fujioka, M. Tsutsumi, S. W. B. Harijono, T. Sribimawati, B. P. Sitorus, R. B. Yhya, M. Karmini, F. Renggono, B. L. Parapat, W. Djojonegoro, P. Mardio, N. Adikusumah, H. T. Endi, and H. Wiryosumarto, A preliminary report on observations of equatorial atmosphere dynamics in Indonesia with radars and radiosondes, *J. Meteorol. Soc. Japan, submitted*, 1994.

5. Tsutsumi, M., T. Tsuda, T. Nakamura, and S. Fukao, Wind Velocity and Temperature Fluctuations due to a Two-day Wave Observed with Radio Meteor Echoes, *J. Geophys. Res., submitted*, 1994.

6. Namboothiri, S. P., T. Tsuda, M. Tsutsumi, T. Nakamura, C. Nagasawa, and M. Abo, Simultaneous observations of mesospheric gravity waves with the MU radar and the Sodium lidar, *J. Geophys. Res., submitted*, 1994.

7. Meek, C. E., A. H. Manson, S. J. Franke, W. Singer, P. Hoffmann, R. R. Clark, T. Tsuda, T. Nakamura, M. Tsutsumi, M. Hagan, D. C. Fritts, J. Isler, and Yu I. Portnyagin, Global study of northern hemisphere quasi-2-day wave events in the summers of 1991 and 1992, *J. Atmos. Terr. Phys., submitted*, 1994.